

UNDERSTANDING AND MITIGATING DEFECTS IN BARIUM STRONTIUM
TITANATE RUDDLESDEN-POPPER SUPERLATTICES FOR HIGH FREQUENCY
TUNABLE DIELECTRICS

A Dissertation

Presented to the Faculty of the Graduate School

of Cornell University

in Partial Fulfillment of the Requirements for the Degree of

Doctor of Philosophy

by

Natalie Marie Dawley

December 2018

© 2018 Natalie Marie Dawley

UNDERSTANDING AND MITIGATING DEFECTS IN BARIUM STRONTIUM
TITANATE RUDDLESDEN-POPPER SUPERLATTICES FOR HIGH FREQUENCY
TUNABLE DIELECTRICS

Natalie Marie Dawley, Ph. D.

Cornell University 2018

Materials challenges are a substantial obstacle for gigahertz frequency technologies such as high-bandwidth 5G cellphone networks. These challenges are especially prominent in the development of tunable dielectric materials, essential for tunable filters and antennas. Large loss of the electric field arises in the most common tunable dielectrics at high frequencies from entropically-favored point defects and polar inhomogeneities. Strained $(\text{SrTiO}_3)_n\text{SrO}$ Ruddlesden-Popper superlattices are tunable dielectrics with unprecedented low loss up to 120 GHz and the highest reported figure of merit (FOM) of all known tunable dielectrics. This low loss is thought to be due to the defect-mitigating nature of the Ruddlesden-Popper structure.

In this thesis, I improve on previous $(\text{SrTiO}_3)_n\text{SrO}$ tunable dielectrics with the incorporation of BaTiO_3 into the metastable structure, forming $(\text{SrTiO}_3)_{n-1}(\text{BaTiO}_3)_1\text{SrO}$. A single layer of BaTiO_3 in the superlattice provides targeted chemical pressure to polarize the neighboring SrTiO_3 for thicker, more tunable films, giving a record-breaking 200% improvement in the FOM for tunable dielectrics. Preliminary work on higher barium-concentration SrTiO_3 Ruddlesden-Popper superlattices is shown for out-of-plane ferroelectric/tunable devices.

These structures were made using molecular-beam epitaxy and required advancements in the calibration of shutter times to deposit precisely one monolayer. This thesis discusses a refinement of the standard SrTiO₃ calibration by reflection high-energy electron diffraction (RHEED) oscillations, with an emphasis on oscillation curvature and codeposition oscillations.

This thesis also describes efforts to understand the loss mechanisms in these materials by probing the defect-mitigating nature of (SrTiO₃)_nSrO via positron annihilation lifetime spectroscopy (PALS) of a compositional series of $n = 6$ (Sr_{1+ δ} TiO₃)_nSrO films. Throughout this series the dominant positron lifetime shows little variance and is associated with TiO_x vacancies. These TiO_x vacancies are likely charge neutral and may be the (SrO)₂ layers themselves, demonstrating the (SrTiO₃)_nSrO structure's ability to accommodate off-stoichiometry and point defects.

To date, the (SrTiO₃)_{n-m}(BaTiO₃)_mSrO films have only been integrated with non-industry-standard substrates like DyScO₃. I integrated (Ba,Sr)TiO₃ and (BaSrTiO₃)_{n-1}(SrTiO₃)₁SrO materials with silicon in MIM devices, showing the highest reported film quality and lowest current leakage in the literature. One to three layers of (SrO)₂ were inserted into 20 nm thick (Ba,Sr)TiO₃ films and found to further lower current leakage by an order of magnitude, demonstrating the Ruddlesden-Popper's ability to dramatically lower loss.

Finally, in a separate study, (SrTiO₃)_nSrO superlattices were examined for how their atomically precise interfaces suppress thermal transport for applications including thermal barrier coatings and thermoelectrics.

BIOGRAPHICAL SKETCH

Natalie Dawley was born in Virginia, USA to Scott and Julie Dawley and grew up with her siblings Stephen and Helen. Science was an early dinner table discussion as both her parents work as chemists and rocket scientists. In high school Natalie excelled in her classes with a particular focus on French language. She studied as an exchange student in Lorient, France for a semester and in Virginia won first place in a French poetry recitation competition. As a senior she took Physics and found a passion for understanding the world through Math. She graduated with honors in 2011 with a bachelors of science in Physics and a minor in Materials Science and Engineering from the University of Virginia where she met her husband, fellow physicist Ruffin Evans. The summer after her sophomore year she was an REU student at University of Delaware with professor Ismat Shah studying P3HT / TiO₂ spray-on hybrid organic solar cells. The following summer she studied aluminum-induced crystallization of silicon on quartz for silicon wire array solar cells at a summer REU with professor Joan M. Redwing at Penn State University. At UVA her senior thesis was with Electrical Engineering professor Mool C. Gupta on carbon nanotubes as transparent electrodes for solution processable silicon solar cells. She joined the Materials Science and Engineering department at Cornell University in 2011 for her Masters and PhD as a Clare Boothe Luce Fellow with professor Darrell G. Schlom studying the growth of oxide superlattices and their properties by molecular-beam epitaxy. At Cornell she was active in mentoring and supporting women in engineering. Natalie enjoys cooking, hiking, and reading classic literature in her spare time.

To Ruffin and my family - Scott, Julie, Stephen, & Helen

ACKNOWLEDGMENTS

I would like to thank the support and direction of my advisor Darrell Schlom and committee members Lena Kourkoutis and Bruce van Dover. My work could not have been done without the help and enthusiasm of many collaborators especially Gerhard Olsen, Nate Orloff, Eric Marksz, Aaron Hagerstrom, Megan Holtz, Kiyong Lee, and Ella Pek.

I have enjoyed the supportive atmosphere in the Schlom group and wish all the best to my lab mates. For the patience and support of Che-hui Lee, Charles Brooks, and Carolina Adamo teaching me how to grow on the MBE. The generosity of Hanjong Paik and Hari Nair teaching me how to fix the many ways an MBE can break. The friendship over many days and nights in the lab with my fellow group members Alex Melville, Shaobo Zhu, Julia Mundy, Eva Smith, Zhe Wang, Jessica Burton, Rachel Steinhardt, Nate Schreiber, Matthew Barone, and Jake Sun. I would also like to thank the many post-docs who have taken the time to share their knowledge and interest in oxides with me especially Tassilo Heeg, Arsen Soukiassian, Yuefeng Nie, Rainer Held, Phil King, John Heron, Eric Langenberg, Shuolong Yang, Antonio Mei, and Jisung Park.

And finally and most importantly I would like to thank my family for believing in me and supporting me on this journey. Thank you Ruffin for being there to support and make me smile every day. To my parents and siblings, Scott, Julie, Helen, and Stephen for your love and encouragement. To my family and friends for making the distance from New York to Virginia seem not so far: Ted, Suzanne, Dean, Wanda,

Kristina, Lauren, Melissa, and the Jones, Croto, Evans, and Adamson families. I would also like to dedicate this work in part to my grandfathers, Jay P. Dawley and John L. Sherwin, who passed away during my graduate work, who shared a love of science, engineering, and discovery.

I have been honored to be funded by the Clare Boothe Luce Fellowship, DOW Chemical Company Foundation Fellowship, and Kionix Fellowship. My research is supported by the U.S. Department of Energy, Office of Basic Sciences, Division of Materials Sciences and Engineering, under Award No. DE-SC0002334 and the Army Research Office under grant GFEB001020505000001. Sample preparation was in part facilitated by the Cornell NanoScale Science & Technology Facility (CNF), a member of the National Nanotechnology Coordinated Infrastructure (NNCI), which is supported by the National Science Foundation (Grant NNCI-1542081). Ferroelectric and dielectric measurements with temperature were conducted at the Center for Nanophase Materials Sciences, which is a DOE Office of Science User Facility. This work made use of Cornell Center for Materials Research Shared Facilities, which are supported through the NSF MRSEC program (DMR-1719875). This work was supported in part by ASCENT, one of six centers in JUMP, a Semiconductor Research Corporation (SRC) program sponsored by DARPA.

TABLE OF CONTENTS

BIOGRAPHICAL SKETCH	v
ACKNOWLEDGMENTS	vii
Chapter 1 Introduction to Molecular-Beam Epitaxy	1
Reflection High-Energy Electron Spectroscopy (RHEED)	2
Origin of RHEED Diffraction Pattern	3
Surface Effects on the RHEED Pattern	6
Kikuchi Lines	6
RHEED Oscillations	7
SrTiO ₃ RHEED Oscillations for Monolayer Precise Superlattice Growth	8
Chapter 2 Applying Chemistry to Improve Today's Best Tunable Dielectric: The Inequivalence of Local and Global Strain	18
Growth and Structural Characterization	25
Ferroelectric Measurements	27
First-principles calculations - the Strain Effect of Barium	29
Millimeter-Wave Devices	30
Methods	34
Supplementary Information	42
Chapter 3 Off-stoichiometric defect accommodation in (SrTiO ₃) _n SrO Ruddlesden- Popper superlattices studied by positron annihilation	56
Experiment	59

Discussion	62
Supplementary Information	65
Chapter 4 Dependence of Dielectric Constant and Leakage on Sample Quality in (Ba,Sr)TiO ₃ Silicon MIM Devices	71
Film growth and structural characterization	73
Dependence of dielectric constant and leakage on sample quality	75
Supplementary Information	80
Chapter 5 Thermal conductivity of the $n = 1 - 5$ and 10 members of the (SrTiO ₃) _n SrO Ruddlesden-Popper superlattices	83
Experiment	87
TDTR Results	91
Chapter 6 Outlook and Conclusion	98
Out-of-plane ferroelectric barium-containing (SrTiO ₃) _n SrO Ruddlesden-Popper superlattices	98
Conclusion	104
Appendix A: Photolithography	107

LIST OF FIGURES

Figure 1.1 Image of the MBE chamber	2
Figure 1.2 Schematic of the setup of the RHEED system and electron path.	3
Figure 1.3 A slice of a 3D Ewald sphere.	4
Figure 1.4 The production of a RHEED pattern from the Ewald sphere intersecting the reciprocal lattice rods.	5
Figure 1.5 The RHEED diffraction pattern along the [110] azimuth of (110) DyScO ₃	7
Figure 1.6 Left, RHEED diffraction pattern of a SrTiO ₃ surface along the [110] azimuth. Top right, the resulting oscillation pattern.....	10
Figure 1.7 SrTiO ₃ oscillations monitoring diffraction spots as in Figure 1.6. The ending curvatures of both components are shown right,	12
Figure 1.8 Left, a schematic of the Sr ₂ TiO ₄ unit cell. Right, x-ray diffraction patterns from three 30 nm thick Sr ₂ TiO ₄ films grown on (100) LSAT.....	13
Figure 1.9 X-ray diffraction from a 300 nm thick $n = 10$ (SrTiO ₃) _n SrO superlattice grown on (100) SrTiO ₃	14
Figure 1.10 Top, a RHEED image during the growth of a 300 nm thick $n = 2$ (SrTiO ₃) _n SrO film on (001) SrTiO ₃ along the [110] azimuth.....	16
Figure 2.1 The inequivalence of local chemical and global epitaxial strain in (SrTiO ₃) _{n-1} (BaTiO ₃) ₁ SrO phases.	22
Figure 2.2 Structural characterization of ~50 nm thick epitaxial (SrTiO ₃) _{n-1} (BaTiO ₃) ₁ SrO films with $n = 2-6$ grown on (110) DyScO ₃ substrates.	26
Figure 2.3 Emergence of ferroelectricity in (SrTiO ₃) _{n-1} (BaTiO ₃) ₁ SrO films grown on (110) DyScO ₃	28
Figure 2.4 In-plane dielectric constant (K_{11}) of 100 nm $n = 6$ (SrTiO ₃) _{n-1} (BaTiO ₃) ₁ SrO film on (110) DyScO ₃ , and its tunability at room temperature and high frequency.	31
Figure 2.5 Schematic of the crystal structure of (SrTiO ₃) _{n-1} (BaTiO ₃) ₁ SrO phases for n	

= 2-6.....	42
Figure 2.6 ω rocking curves of 50 nm thick $(\text{SrTiO}_3)_{n-1}(\text{BaTiO}_3)_1\text{SrO}$ thin films grown on (110) DyScO_3	43
Figure 2.7 STEM-EELS measurements of the $n = 6$ $(\text{SrTiO}_3)_{n-1}(\text{BaTiO}_3)_1\text{SrO}$ thin films.	44
Figure 2.8 Overview HAADF-STEM images of the 50 nm thick $n = 2-6$ $(\text{SrTiO}_3)_{n-1}(\text{BaTiO}_3)_1\text{SrO}$ films.	45
Figure 2.9 High magnification HAADF-STEM images of the $n = 3-6$ $(\text{SrTiO}_3)_{n-1}(\text{BaTiO}_3)_1\text{SrO}$ thin films.	46
Figure 2.10 Annular dark field and annular bright field images of the 50 nm $n = 6$ $(\text{SrTiO}_3)_{n-1}(\text{BaTiO}_3)_1\text{SrO}$ compound.	47
Figure 2.11 Polarization versus applied electric field hysteresis loops of 50 nm $n = 2-6$ $(\text{SrTiO}_3)_{n-1}(\text{BaTiO}_3)_1\text{SrO}$ films grown on (110) DyScO_3	48
Figure 2.12 Phonon frequencies and energy gains for the ferroelectric instabilities as a function of the perovskite layer thickness, n	49
Figure 2.13 Broadband DC to Millimeter-wave dielectric permittivity characterization devices.	50
Figure 2.14 Broadband complex permittivity of the $n = 6$ $(\text{SrTiO}_3)_{n-1}(\text{BaTiO}_3)_1\text{SrO}$ thin film.	51
Figure 2.15 Tuning of the real part of the complex permittivity of the $n = 6$ $(\text{SrTiO}_3)_{n-1}(\text{BaTiO}_3)_1\text{SrO}$ thin film under an applied bias electric field.	51
Figure 3.1 X-ray diffraction of $\delta \pm 5\%$ of 300 nm thick $n = 6$ $(\text{Sr}_{1+\delta}\text{TiO}_3)_n\text{SrO}$ films grown on (001) SrTiO_3	60
Figure 3.2 The c -axis of $n = 6$ $(\text{Sr}_{1+\delta}\text{TiO}_3)_n\text{SrO}$ films shown in Figure 3.1 calculated by Nelson-Riley analysis.	61
Figure 3.3 The dominant positron lifetime from a free fit of the PALS spectra of the $n = 6$ $(\text{Sr}_{1+\delta}\text{TiO}_3)_n\text{SrO}$ films.	62
Figure 4.1 X-ray diffraction, 2θ , of a series of $x = 0.3$ $\text{Ba}_x\text{Sr}_{1-x}\text{TiO}_3$ films in blue and $x = 0.3$ $(\text{Ba}_x\text{Sr}_{1-x}\text{TiO}_3)_{n-1}(\text{SrTiO}_3)\text{SrO}$ films in red, grown on 50 nm SrRuO_3 / 20 nm SrTiO_3 / (001) Si	74
Figure 4.2 Annular dark field STEM (a-d, g, and h) of $x = 0.3$ $\text{Ba}_x\text{Sr}_{1-x}\text{TiO}_3$ samples shown in Figure 4.1.	75

Figure 4.3 a, The out-of-plane dielectric constant K_{33} is seen to increase with lower sample quality (higher FWHM).....	77
Figure 4.4 Current leakage in MIM devices for two different electric fields.....	78
Figure 4.5 ω rocking curves of the 002 silicon and 002 film peak for: a – c films of 20 nm $x = 0.3 \text{ Ba}_x\text{Sr}_{1-x}\text{TiO}_3$ / 50 nm SrRuO_3 / 15 nm SrTiO_3 / (001) Si.....	80
Figure 4.6 Current Leakage in MIM devices with applied voltage.....	80
Figure 5.1 θ - 2θ x-ray diffraction scans of the epitaxial 300 nm thick $\text{Sr}_{n+1}\text{Ti}_n\text{O}_{3n+1}$ ($n=1-5, 10$) films grown on (001) SrTiO_3 (001) LSAT.	89
Figure 5.2 Annular-dark-field STEM images of the epitaxial Ruddlesden-Popper	90
Figure 5.3 Summary of experimental and simulated cross-plane thermal conductivities of the Ruddlesden-Popper $(\text{SrTiO}_3)_n\text{SrO}$ phases as a function of interface density.....	92
Figure 6.1 a, Schematic of the $(\text{BaTiO}_3)_{n-3}(\text{SrTiO}_3)_3\text{SrO}$ unit cell. b, First-principles calculation of the phonon component associated with in-plane polarization for $(\text{BaTiO}_3)_{n-3}(\text{SrTiO}_3)_3\text{SrO}$	99
Figure 6.2 a, A schematic of the $(\text{BaTiO}_3)_5(\text{SrTiO}_3)_1\text{SrO}$ unit cell with barium atoms shown in pink and strontium atoms in green.	100
Figure 6.3 a, X-ray Diffraction of 150 nm thick $(\text{Ba}_{60}\text{Sr}_{40}\text{TiO}_3)_{n-1}(\text{SrTiO}_3)_1\text{SrO}$ films grown on 15 nm thick SrRuO_3 bottom electrodes on (110) DyScO_3	102
Figure 6.4 The out-of-plane dielectric temperature, K_{33} , with temperature of the $n = 20, 15,$ and $10 (\text{Ba}_{60}\text{Sr}_{40}\text{TiO}_3)_{n-1}(\text{SrTiO}_3)_1\text{SrO}$ films.	103

Chapter 1

Introduction to Molecular-Beam Epitaxy

Molecular-beam epitaxy (MBE) is a thin film growth technique requiring a high vacuum chamber with heated elemental sources evaporating and condensing onto a heated substrate. This substrate acts as an atomic template for the growing crystal. In this chapter I will discuss the set-up of the chamber, oxide growth mechanisms, and reflection high-energy electron diffraction.

In the family of thin film deposition techniques under vacuum, like pulsed laser deposition (PLD), sputtering, and thermal evaporation, molecular-beam epitaxy (MBE) provides the highest control of monolayer species for epitaxial single crystal thin film growth. Developed in the 1960's at Bell Labs¹, MBE was created for the epitaxial growth and doping of the GaAs system. Sources of pure elements or compounds held in crucibles are thermally evaporated, forming 'molecular beams' to react at the surface of a heated single crystal. Gases can also be introduced as molecular beams, like oxygen or nitrogen. Usually these gases are 'cracked' or put under a high electric field to dissociate the molecules to make a more reactive source. In Figure 1.1 a picture and diagram is shown of the MBE setup used in this thesis. Here, the chamber is equipped with reflection high-energy electron diffraction (RHEED), which gives *in situ* information of the crystal surface during growth. MBE can also be combined with other techniques like electron-beam deposition or sputtering, useful for elements that have high melting points or are reactive with common crucible materials.

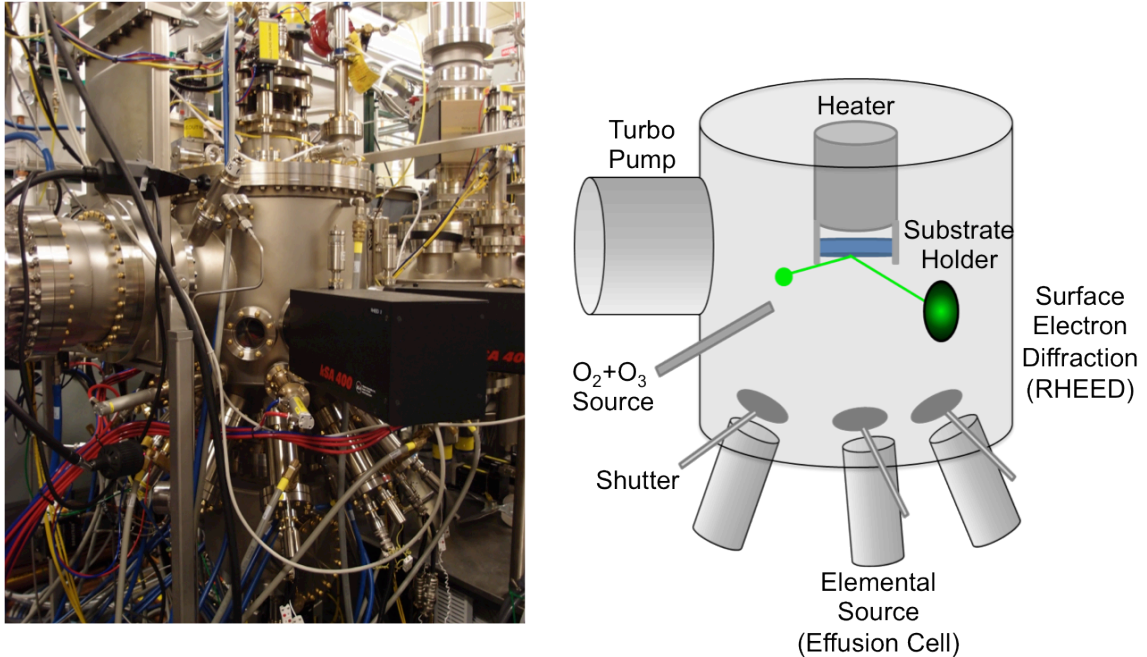


Figure 1.1 Image of the MBE chamber with effusion-cell elemental sources shown surrounding the bottom of the chamber, a RHEED screen and camera can be seen in the black boxes, and a turbo pump and cryo pump are attached to the chamber

Reflection High-Energy Electron Spectroscopy (RHEED)

RHEED provides access to *in situ* information on the structural changes of atomic surfaces during growth. Electrons are excellent probe particles due to their large scattering cross-section, the compact size of the equipment needed, and their subangstrom wavelengths: an electron with the energy of 10 keV has a wavelength of 0.12 Å. At a grazing angle to the surface, the electron beam can be maximally elastically diffracted from the surface atomic lattice without much noise from inelastic scattering. RHEED was first performed by Nishikawa and Kikuchi in 1928².

The RHEED setup is shown below in Figure 1.2. The electron gun attached to the chamber produces electrons via thermionic emission from a heated tungsten hairpin filament. Those electrons are further collimated and focused with electrostatic

and magnetic optics. After diffracting from the surface at $< 10^\circ$ angle, the diffracted electron beam hits and excites a phosphor screen. The diffracted pattern on the phosphor screen is recorded with a CCD camera, which communicates with a lab computer for further analysis of the spatial orientation and intensity of the diffraction pattern.

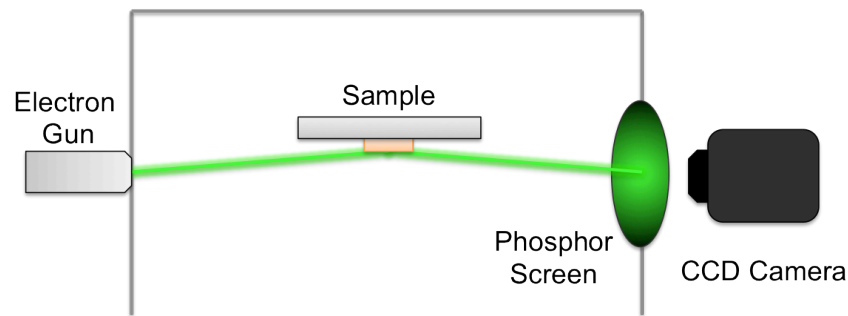


Figure 1.2 Schematic of the RHEED system and electron path.

Origin of RHEED Diffraction Pattern

Diffraction is the process of constructive and destructive interference of waves (electron, photons, *etc.*) from a periodic arrangement of some obstacle. Here we are diffracting electron particle/waves from an atomic lattice.

We can think of diffraction in the physical sense of waves diffracting off of atomic planes, or we can calculate it more efficiently in momentum k space where each crystal plane represents a reciprocal lattice point. The diffracted pattern we observe reflects the surface reciprocal lattice with the addition of surface topography artifacts. Each hkl point in the reciprocal lattice represents a crystallographic plane

with (hkl) Miller indices. Distances between the real space and reciprocal lattice planes are inverses of each other.

With the reciprocal lattice we can construct the Ewald Sphere, which is a useful tool to identify the atom planes where the constructive interference of diffraction occurs. The probing electron beam vector has a k magnitude of $1 / \lambda \text{ \AA}^{-1}$ (λ is the wavelength of the incoming electron beam) and the same direction as the real space electron beam relative to the crystal. For momentum conservation, assuming elastic scattering, the diffracted outgoing electron wave must have the same magnitude in momentum as the incoming wave. Diffraction will then occur at any point within a $1 / \lambda \text{ \AA}^{-1}$ radius of the incoming electrons where this 'Ewald sphere' meets with a reciprocal lattice point. Thus, the vector between the two, called \vec{G} (not shown), is a valid reciprocal space lattice vector. Figure 1.3 displays a representation of the Ewald sphere in reciprocal space.

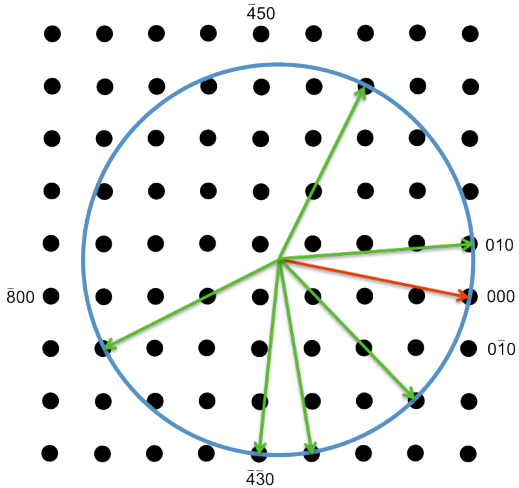


Figure 1.3 A slice of a 3D Ewald sphere. The red arrow represents the incoming electron beam and the green waves are possible diffraction vectors.

In this case we are working with surfaces and not a 3D crystal lattice. RHEED only probes the first few atomic layers of the sample. Thus, we lack periodicity in the out-of-plane direction. Since we lose this axis, in reciprocal space the points along the out-of-plane direction become infinitely extending rods. In Figure 1.3, instead of additional layers of reciprocal lattice points in the out-of-plane direction, the points become rods. At the intersection of the rod and the Ewald sphere diffraction occurs. Seen below in Figure 1.4, the phosphor screen only catches part of the pattern produced by diffraction. The reciprocal rods increase in width with the disorder of a step and terrace structure on the surface, changing the diffraction pattern observed from points to streaks with their size being inversely proportional to the average terrace width.

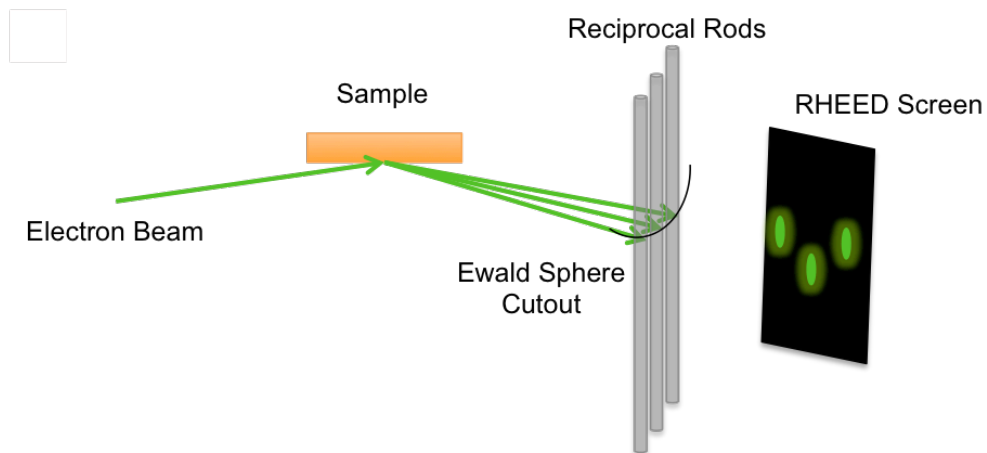


Figure 1.4 The production of a RHEED pattern from the Ewald sphere intersecting the reciprocal lattice rods.

Surface Effects on the RHEED Pattern

During growth our film surfaces are not always as atomically flat as we would like them to be. When the diffusion length of an atom impinging on a surface is smaller than the distance to the nearest terrace, islands begin to form, creating surface roughness. If the islands are mostly flat, as in Stranski-Krastanov growth, then the electron beam will be a mix of diffraction from the flat surface and diffraction through the islands. When the beam travels through the islands an additional pattern of spots is observed, similar to the diffraction patterns seen in transmission electron microscopes (TEM)³. Our 2D Ewald sphere case becomes 3D again.

Another surface effect that can be observed by RHEED is faceting. If the growth surface is a high surface-energy plane, the growing film can facet into lower energy planes. This faceting can cause the electron beam to be reflected at a different angle, causing a splitting of the diffraction spots into chevrons or separate spots. See reference [4] for examples and explanation.

Kikuchi Lines

Kikuchi lines are broad streaks of intensity observed in the RHEED pattern from inelastic/incoherent scattering. Figure 1.5 shows an example of Kikuchi lines on a (110) DyScO₃ substrate along the [110] azimuth. When electrons undergo inelastic/diffuse scattering in the crystal they lose energy and are scattered in all directions. This wide beam of electrons in k space can then undergo diffraction from atomic planes, forming Kossel cones, which appear as Kikuchi lines. We only observe a slice of the cone as the Kikuchi line. Kikuchi lines are very sensitive to surface

smoothness and thus are most often seen from bare substrates and then decay in intensity with film deposition⁵.

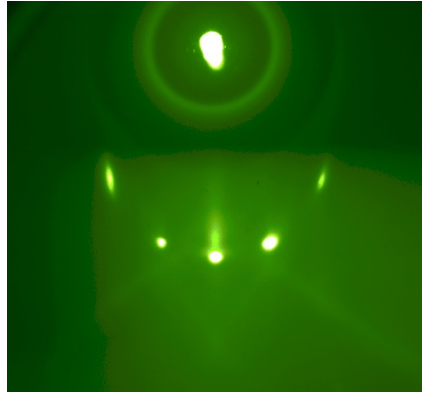


Figure 1.5 The RHEED diffraction pattern along the [110] azimuth of (110) DyScO₃. The diffuse Kikuchi lines can be clearly seen about the specular diffraction spot with the direct spot seen on top.

RHEED Oscillations

The growth mechanism of the film will affect the intensity of electrons hitting the phosphor screen that form the RHEED pattern. RHEED intensity oscillations, measured by monitoring the intensity of a specific diffraction spot over time, are key to obtaining the time for a complete monolayer formation, with accuracies of up to ~ 1%.

An oscillation in intensity of the RHEED diffraction pattern is seen during codeposition from layer-by-layer growth. During codeposition, as the layer begins to form, the RHEED beam interacts with an atomically rough surface, is scattered more, and diffraction intensity goes down. As the layer begins to complete one monolayer and becomes smoother, intensity increases until a full monolayer is reached and the beam can be minimally scattered.

The origin of typical RHEED oscillations used in shutter growth calibration is still not well understood, but is affected by electron phase and the scattering factor of the element being deposited⁶. For SrTiO₃, when the strontium shutter is opened the intensity of the diffraction spots increases and when titanium is deposited, the intensity decreases. The reverse can also occur, especially when starting on a new substrate with mixed termination or at specific angles of the electron beam impinging on the surface.

In step-flow growth, as with vicinal substrates, no oscillations are observed as monolayers do not grow consecutively, but grow concurrently in moving the surface step edges forward. Thus, the coverage of the new layer remains constant during growth and the RHEED intensity does not change. It is possible to have a mixed growth mechanism of nucleation of terraces and step flow growth that can also lead to a constant RHEED intensity with deposition time⁷.

In island or mixed growth, oscillations can still be seen from layer-by-layer growth on the island surfaces, but the overall amplitude is weaker due to decreased flat surfaces to diffract from, and the overall intensity may vary as the surface becomes more or less rough. The RHEED diffraction pattern is lower in intensity as some of the beam is diverted by traveling through the islands, creating a 'spotty' 3D crystal transmission pattern. See reference [8] for further information.

SrTiO₃ RHEED Oscillations for Monolayer Precise Superlattice Growth

The calibration of strontium and titanium sources for precise superlattice

growth is a time-consuming challenge involving 6+ hours of RHEED oscillation observation to detect and correct for small changes in the drift of elemental deposition rates. Layers of SrO and TiO₂ are deposited sequentially and the resulting intensity modulation in the RHEED diffraction spots are observed, with strontium increasing the diffraction intensity and titanium decreasing it (this is likely due to the higher scattering factor of strontium versus titanium). Ideally this creates a perfectly sinusoidal pattern when plotted over time with diffraction spot intensity on the y -axis and time on the x -axis. Several papers have addressed this calibration method^{6,9,10} in a helpful but incomplete manner. Through years of practice I have found additional key properties of these oscillations to reliably achieve atomically precise superlattices.

To calibrate SrTiO₃ and BaTiO₃ for superlattice growths, I match the deposition rate of the strontium and titanium sources so the time to deposit one monolayer of each source is identical; this allows me to both shutter and codeposit the elemental sources. The shuttered RHEED oscillations allow for identification and correction of the stoichiometry, and the codeposition oscillations of the true deposition time for one monolayer. To calibrate SrTiO₃ and find the ideal source temperature and shutter times, I first observe shuttered RHEED oscillations with the shutter times for SrO and TiO₂ set to be equal. I look for excess on the A or B -site and adjust to achieve a 1:1 stoichiometry (described in the paragraph below). I monitor the diffraction from the [110] azimuth of the cubic substrate surface as strontium excess can be readily observed as half-order spots in the diffraction pattern and be adjusted for. These spots appear much more readily than in the [100] azimuth where half-order spots associated with titanium excess are observed. Once titanium excess is observed it can be difficult

to return to a smooth surface and well ordered oscillations.

The shuttered calibration is deemed to be complete and accurate when stable RHEED oscillations are achieved for >15 min with no observable change in shape over time and ideally in overall intensity. Small drift in overall intensity is tolerable if it is associated with the inevitable slow surface roughening at sub-optimal growth temperatures, usually greater than $\sim 850\text{ }^{\circ}\text{C}$ or less than $650\text{ }^{\circ}\text{C}$. Once the shuttered portion of the calibration is complete I then codeposit ~ 6 unit cells of SrTiO_3 . The period of these codeposited oscillations give the true monolayer deposition time for both sources that can then be used as the new shutter time in the shuttered superlattice growth (Figure 1.6).

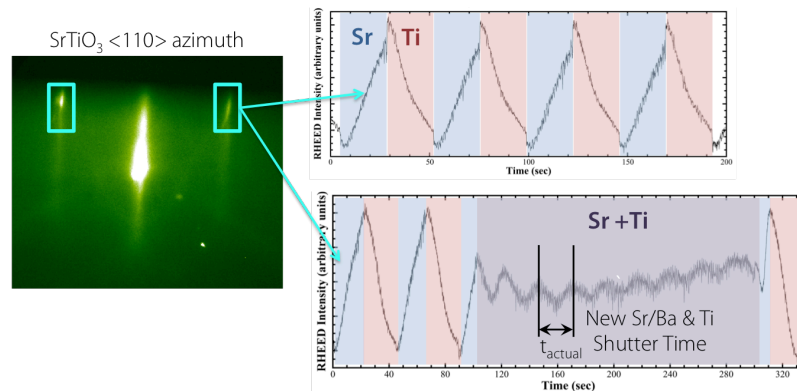


Figure 1.6 Left, RHEED diffraction pattern of a SrTiO_3 surface along the $[110]$ azimuth. Top right, the resulting oscillation pattern from the intensity modulation of the diffraction spots shown in the left figure from shuttering individual monolayers of SrO and TiO_2 . Bottom right, oscillations observed from codeposition of SrO and TiO_2 with a first layer of $\frac{1}{2}$ SrO , eight unit cells of SrTiO_3 deposited, and then another $\frac{1}{2}$ layer of SrO , followed by a final layer of TiO_2 . The accurate shutter time for one layer of SrO and TiO_2 is the period of the codeposition oscillations.

What I realized was key for shuttered RHEED oscillation calibrations was that

the comparison of the ending curvature of each elemental portion of the oscillation was a sensitive indicator of off-stoichiometry. If left uncorrected these indicators will develop into clear *A* or *B*-site excess with the additional peaks/troughs and diffraction half-order RHEED streaks associated with *A* or *B*-site excess⁹. By recognizing these subtle signs a more accurate calibration can be achieved with finer resolution.

Seen below in Figure 1.7 are two calibrations with excess SrO, top, or TiO₂, bottom where the excess element is identified as the oscillation portion that has greater curvature than the other. The temperature of the strontium source is then lowered or raised to account for the excess, with the titanium source and shutter times remaining unchanged. For my work a Ti-ballTM was used as the titanium source¹¹, which has a slow stabilization time after the flux is changed and thus was not adjusted during growth. This is done in steps of 0.1 °C of the strontium source until a perfect condition can be identified. The calibration is deemed stoichiometric when shuttered components consistently end with the same curvature in the RHEED oscillations. They may be more or less curved depending on the growth and electron beam conditions.

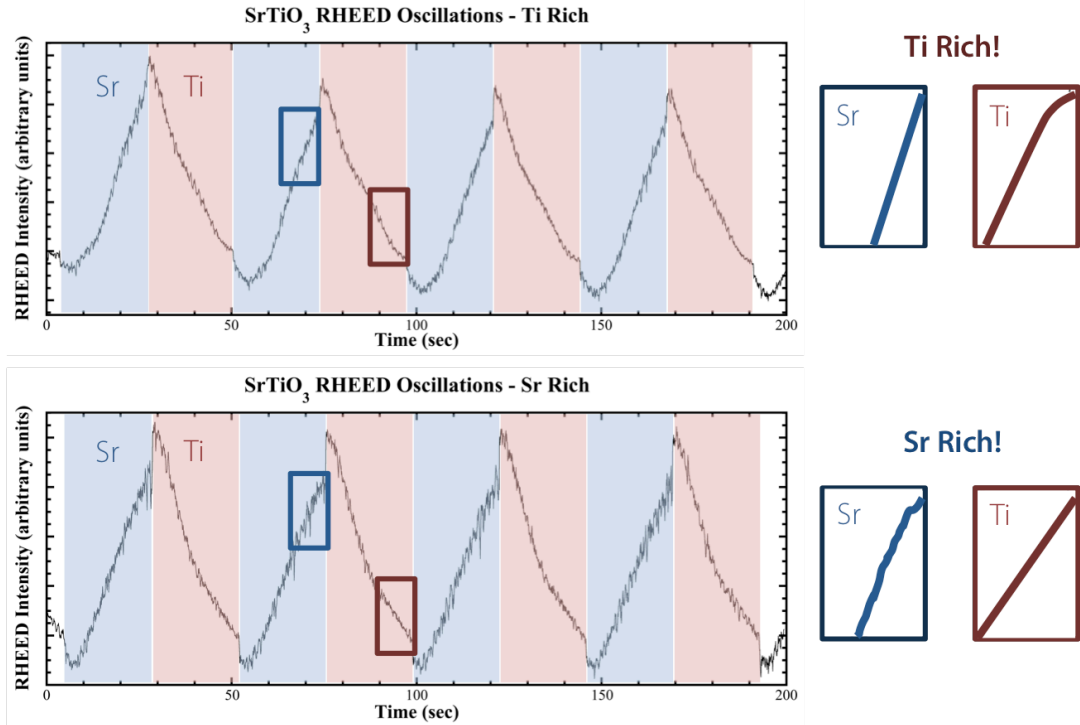


Figure 1.7 SrTiO₃ shuttered oscillations from monitoring diffraction spots as in **Figure 1.6**. The ending curvatures of both components are shown right, with that of TiO₂ inverted for easy comparison. Top, in these oscillations there is excess TiO₂ in the SrTiO₃ as the TiO₂ ending curvature is greater. Bottom, SrO-rich SrTiO₃ oscillations where the SrO ending curvature has slightly higher curvature.

After stable oscillations are reached and codeposition is achieved to determine an accurate shutter time for each component, a shuttered growth of 30 nm thick Sr₂TiO₄ film is made by shuttered growth (usually on a well lattice matched substrate like (001) LSAT, (001) SrTiO₃, or (110) NdGaO₃) to confirm an accurate calibration. Sr₂TiO₄, being the $n = 1$ of the Ruddlesden-Popper series, is extremely sensitive to off-stoichiometry. The 002 and 004 peaks in the resulting x-ray diffraction spectra shown in Figure 1.8, predictably shift with monolayer coverage. If more than one monolayer is deposited the superlattice 002 and 004 peaks shift outward, and if less than one monolayer then the peaks shift inward as compared to a perfect crystal. It is

thought this shift in the x-ray diffraction peaks is the manifestation of a beating in the superlattice structure periodicity when the monolayers are $> |1|$. Further work is being done to explain this effect. Empirically it was found that the shutter time for the SrO and TiO₂ layers can be corrected for atomically precise superlattices using the equation shown in Figure 1.8.

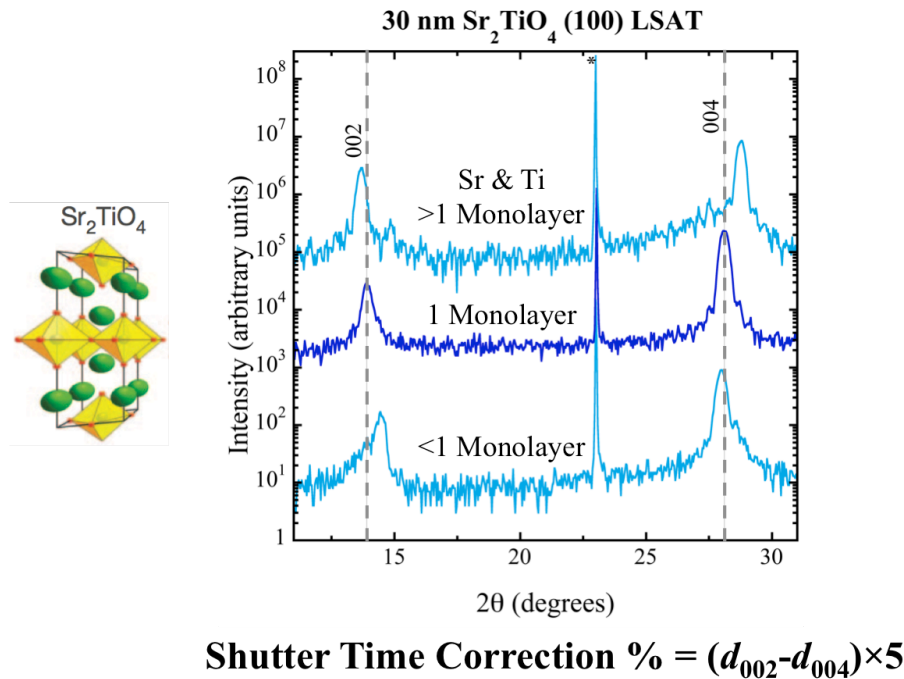


Figure 1.8 Left, a schematic of the Sr₂TiO₄ unit cell. Right, 2θ x-ray diffraction patterns from three 30 nm thick Sr₂TiO₄ films grown on (100) LSAT with varying amounts of monolayer coverage from incomplete to excess. The shutter time is then corrected from an empirical equation displayed at the bottom.

After RHEED oscillation calibration and a test Sr₂TiO₄ sample is grown, precise (SrTiO₃)_nSrO superlattices can be shutter grown as seen in the 300 nm thick $n = 10$ sample in Figure 1.9. Further RHEED calibration can be done using the same method to grow superlattices of multiple components, such as

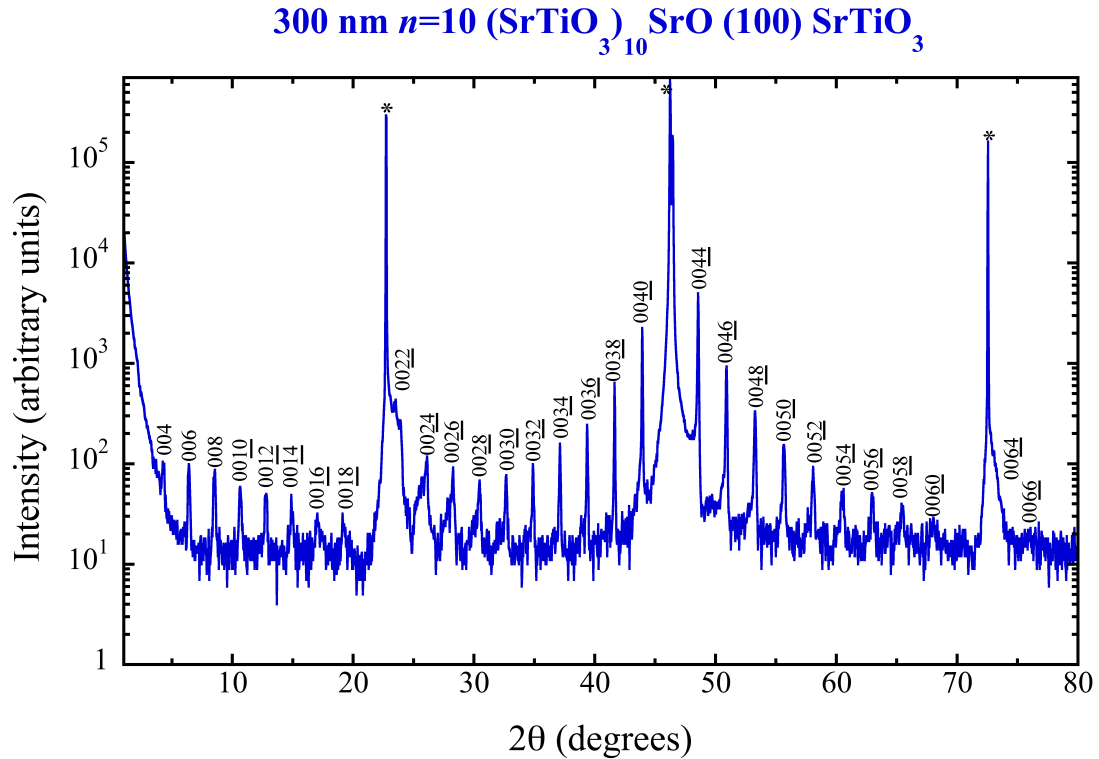
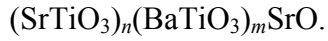
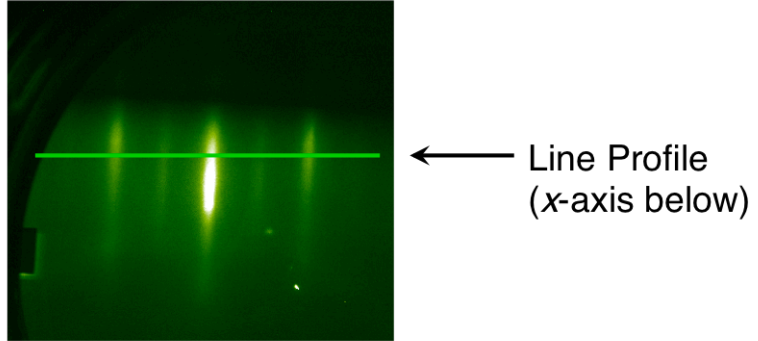


Figure 1.9 X-ray diffraction from a 300 nm thick $n = 10$ $(\text{SrTiO}_3)_n\text{SrO}$ superlattice grown on (100) SrTiO_3 . For this 10+ hour growth the intensity of the half-order RHEED streaks associated with SrO excess, which naturally occur in this structure, were monitored over time as compared to the main diffraction spots to insure they remained relatively stable in the ratio of their intensities overtime. Most often the temperature of the strontium was needed to increase every 2-4 hours.

Due to the controlled slow growth rate of oxide MBE, thicker films take hours to grow, putting the structure quality at risk due to the drift in the source evaporation rates. The 300 nm thick film shown in Figure 1.9 took ~10.5 hrs to grow at a deposition rate of ~25 sec per monolayer. To adjust for drift in the evaporation rate of the sources during growth, I monitored the half-order RHEED streaks along a line profile of the [110] azimuth (Figure 1.10). Strontium titanate Ruddlesden-Popper structures naturally have *A*-site excess from a floating layer of SrO during growth^{12,13}. This excess manifests as a half-order streak in the RHEED pattern along the [110] azimuth from the reconstruction of excess strontium on the surface. During long growths I compare the intensity of the half-order to the main diffraction streaks every 2-3 hours. I then increase (lower) the strontium source temperature by 0.1 °C if the half-order intensity was reduced (increased) relative to the main diffraction streaks, indicating source drift. This ensured stoichiometric growth over long time frames.



After 15 min of Growth

Halfway Through Deposition
- Decrease Sr

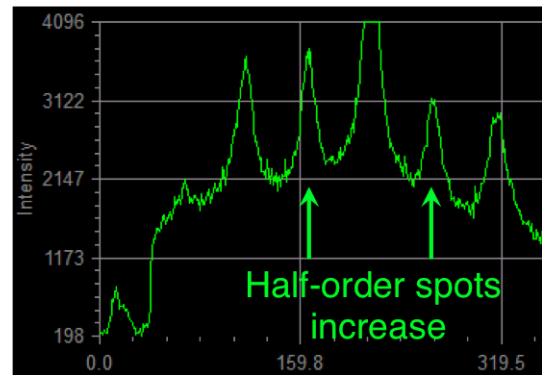


Figure 1.10 Top, a RHEED image along the $[110]$ azimuth during the growth of a 300 nm thick $n = 2$ $(\text{SrTiO}_3)_n\text{SrO}$ film on (001) SrTiO_3 . Bottom, plots of the diffraction intensity along the line shown in the top figure. Bottom left shows the line profile after 15 min of film growth to be used as the base measure for comparison. Bottom right, the line profile halfway through film growth where the half-order spots associated with strontium are seen to increase compared to bottom left. To adjust for this increase, the strontium source temperature was then reduced.

References

1. Cho, A. & Arthur, J. Molecular beam epitaxy. *Prog. Solid State Ch.* **10**, 157–191 (1975).
2. Nishikawa, S. & Kikuchi, S. The diffraction of cathode rays by calcite. *Proc. Imp. Acad.* **4**, 475–477 (1928).
3. Mahan, J. E., Le Thanh, V., Chevrier, J., Berbezier, I., Derrien, J., & Long, R. G. Surface electron-diffraction patterns of β -FeSi₂ films epitaxially grown on silicon. *J. Appl. Phys.* **74**, 1747–1761 (1993).
4. Sanduijav, B., Matei, D., & Springholz, G. *In situ* control of Si/Ge growth on stripe-patterned substrates using reflection high-energy electron diffraction and scanning tunneling microscopy. *Nanoscale Res. Lett.* **5**, 1935–1941 (2010).
5. Ichimiya, A. & Cohen, P. I. *Reflection High Energy Electron Diffraction*. Cambridge University Press, (2004).
6. Sun, H. Y. *et al.* Chemically specific termination control of oxide interfaces via layer-by-layer mean inner potential engineering. *Nat. Comm.* **9**, 2965 (2018).
7. Eason, R. *Pulsed Laser Deposition of Thin Films: Applications-Led Growth of Functional Materials*. John Wiley and Sons, (2007).
8. Li, J. *et al.* Growth and in situ high-pressure reflection high energy electron diffraction monitoring of oxide thin films. *Sci. China Phys. Mech.* **56**, 2312–2326 (2013).
9. Haeni, J. H., Theis, C. D. & Schlom, D. G. RHEED Intensity Oscillations for the Stoichiometric Growth of SrTiO₃ Thin Films by Reactive Molecular Beam Epitaxy. *J. Electroceramics* **4**, 385–391 (2000).
10. Haislmaier, R.C, Stone, G., Alem, N., & Engel-Herbert, R. Creating Ruddlesden-Popper phases by hybrid molecular beam epitaxy. *Appl. Phys. Lett.* **109**, 043102 (2016).
11. Theis, C. D. & Schlom, D. G. Cheap and stable titanium source for use in oxide molecular beam epitaxy systems. *J. Vac. Sci. Technol. A* **14**, 2677 (1996).
12. Lee J. H. *et al.* Dynamic Layer Rearrangement During Growth of Layered Oxide Films by Molecular Beam Epitaxy. *Nat. Mater.* **13**, 879-883 (2014).
13. Nie, Y. F. *et al.* Atomically precise interfaces from non-stoichiometric deposition. *Nat. Comm.* **5**, 4530 (2014).

Chapter 2

Applying Chemistry to Improve Today's Best Tunable Dielectric: The Inequivalence of Local and Global Strain

Natalie M. Dawley^{1*}, Eric J. Marks^{2,3*}, Aaron M. Hagerstrom³, Gerhard H. Olsen⁴, Megan E. Holtz^{1,4}, Jingshu Zhang¹, Christian J. Long³, James C. Booth³, Craig J. Fennie⁴, David A. Muller⁴, Nathan D. Orloff³ & Darrell G. Schlom^{1,5}

1. Department of Materials Science and Engineering, Cornell University, Ithaca, New York 14853, USA

2. Department of Materials Science and Engineering, University of Maryland, College Park, Maryland 20742, USA

3. National Institute of Standards and Technology, Boulder, Colorado 80305, USA

4. School of Applied and Engineering Physics, Cornell University, Ithaca, New York 14853, USA

5. Kavli Institute at Cornell for Nanoscale Science, Ithaca, New York 14853, USA

Correspondence and requests for materials should be addressed to D.G.S. (email: schlom@cornell.edu)

* These authors contributed equally to this work.

Abstract

Tunable dielectrics are key constituents for emerging high-frequency devices in telecommunications—including tunable filters, phase shifters, and baluns—and for miniaturizing frequency-agile microwave and millimeter-wave components. Today's tunable dielectrics with the highest figure of merit (FOM) at room temperature and millimeter-wave frequencies are strained films of $(\text{SrTiO}_3)_6\text{SrO}$. The low loss at frequencies up to 125 GHz comes from the defect mitigating nature of the $(\text{SrTiO}_3)_n\text{SrO}$ Ruddlesden-Popper structure; the tunability arises from a ferroelectric instability induced by epitaxial strain. Unfortunately, the necessity for epitaxial strain limits the film thickness to around 50 nm, which results in insufficient total device tuning for practical application. Here we employ a chemical alternative to provide local strain to induce a ferroelectric instability—the introduction of barium into this Ruddlesden-Popper titanate. No natural barium-containing Ruddlesden-Popper titanates are known, but this atomically engineered superlattice material can be made thicker and we demonstrate a 200% improvement in the FOM of this new $(\text{SrTiO}_3)_{n-m}(\text{BaTiO}_3)_m\text{SrO}$ tunable dielectric.

Epitaxial strain can unlock new and enhanced properties in oxide materials such as inducing ferroelectricity^{1,2}, stabilization of metastable phases^{3,4}, multiferroicity^{5,6}, and can alter the band structure of oxides to enhance electrical transport⁷, magnetic⁸, or superconducting properties^{9,10}. Unfortunately, films with enhanced properties that rely on epitaxial strain are limited in thickness. Above some critical thickness at which material relaxation occurs, dislocations form and the emergent properties induced by the epitaxial strain are degraded or disappear entirely. Another method to impose local strain is through chemical pressure. For example, bonds can be lengthened by the partial substitution of larger isovalent ions in an ionic material, as occurs when barium replaces a portion of the strontium in SrTiO₃ to form (Ba,Sr)TiO₃. Such chemical pressure can often circumvent film thickness limits because it does not involve global strain. Here we use both epitaxial strain and targeted chemical pressure to achieve thicker films while maintaining the desirable properties previously achieved by epitaxial strain. We apply this approach to an electric-field tunable dielectric where, with film thicknesses in the tens of nanometers and no confining electrodes, most of the electric field in the device structure samples the passive substrate and not the active material.

In this Communication we surpass the performance of the record breaking tunable dielectric material (SrTiO₃)_nSrO¹¹ by introducing targeted chemical pressure through the replacement of strontium with barium in a single layer of the crystal structure, forming (SrTiO₃)_{n-1}(BaTiO₃)₁SrO phases (Figure 2.1a). To guide our efforts, the effect of epitaxial strain and chemical pressure on the ferroelectric polarization was investigated using first principles calculations (see Methods section)

as a proxy for room temperature electric-field tunability. The contribution of each atomic layer to the ferroelectric polarization was calculated at 0 K for a range of strain and barium concentrations in the $n = 6$ compounds (Figure 2.1b-d) found to have optimal periodicity from our previous work¹¹. For structures of pure $(\text{SrTiO}_3)_n\text{SrO}$, epitaxial strain is needed to induce ferroelectricity and thus tunability, limiting film thickness. Thicker films are a sure route to enhanced device performance, as thickness can be used to boost the active material to passive substrate ratio sampled by propagating signals.

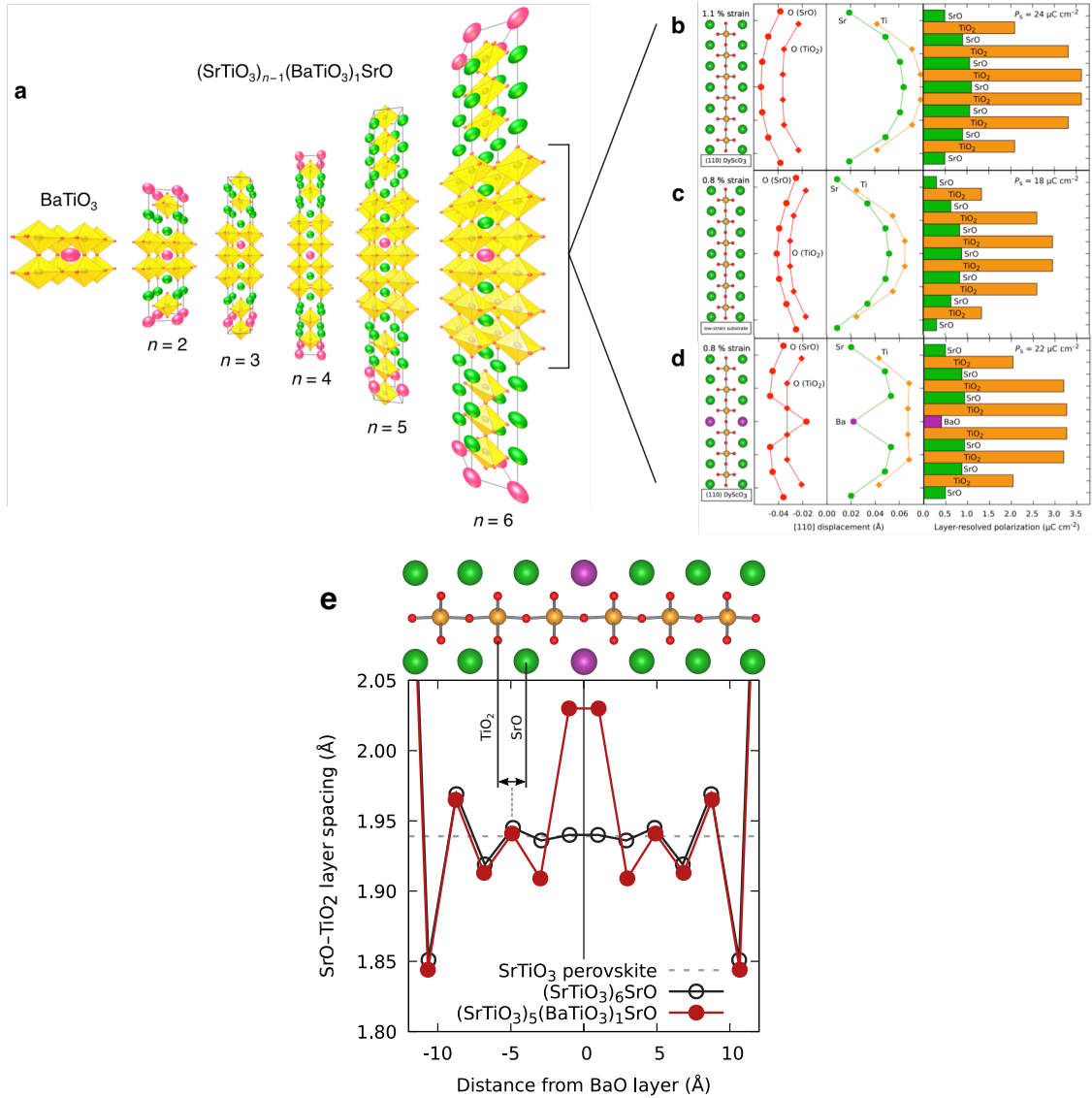


Figure 2.1 The inequivalence of local chemical and global epitaxial strain in $(\text{SrTiO}_3)_{n-1}(\text{BaTiO}_3)_1\text{SrO}$ phases. **a** Schematic of BaTiO_3 and the $(\text{SrTiO}_3)_{n-1}(\text{BaTiO}_3)_1\text{SrO}$ phases for $n = 2-6$ crystal structures. Strontium atoms are shown in green, barium in pink and the unit cells are outlined. **b-d** The effect of epitaxial strain and the addition of the larger barium atom from first-principles calculations on local ferroelectric polarization in the $n = 6$ $(\text{SrTiO}_3)_{n-1}(\text{BaTiO}_3)_1\text{SrO}$ perovskite block of the Ruddlesden-Popper superlattice. Contribution to ferroelectric polarization throughout the (b) $n = 6$ $(\text{SrTiO}_3)_6\text{SrO}$ unit cell epitaxially strained to (110) DyScO₃, (c) $n = 6$ $(\text{SrTiO}_3)_6\text{SrO}$ unit cell epitaxially strained to an intermediate epitaxial strain of 0.8%, d, an $n = 6$ $(\text{SrTiO}_3)_{n-1}(\text{BaTiO}_3)_1\text{SrO}$ unit cell epitaxially strained to (110) DyScO₃. Although c and d have the same epitaxial strain the addition of the local strain from a single larger barium atom further increases the total ferroelectric polarization. **e**, The distortion of the atoms along the c -axis from the addition of a single BaO layer (purple).

Compared to the record breaking $n = 6$ $(\text{SrTiO}_3)_n\text{SrO}$ grown in 1.1% tensile strain on (110)-oriented DyScO_3 , our first-principles calculations suggest that simply lowering the strain to 0.8 % leads to a 25 % reduction of the spontaneous polarization (Figure 2.1b and c), demonstrating the drawback of relying on epitaxial strain in devices requiring thicker films. However, if the same state of 0.8 % tensile strain is reached by substituting a single layer of barium into the superlattice (Figure 2.1d), the polarization is reduced by only 8 %. As seen in Figure 2.1d, the barium layer itself does not enhance polarization, but instead strains the neighboring TiO_2 and SrO layers, in turn leading to a net higher polarization. As shown in Figure 2.1e, the strain imposed by the BaO layer is confined to a few nearest-neighbor layers, demonstrating the importance of atomic layering achievable by correct calibration and MBE. The role played by barium here is distinct from previous reports of $(\text{BaTiO}_3)_m(\text{SrTiO}_3)_n$ superlattices where the polarization is in the out-of-plane direction and arises from the compressively strained BaTiO_3 polarizing neighboring SrTiO_3 layers¹²⁻¹⁴. In strained $(\text{SrTiO}_3)_n\text{SrO}$ and $(\text{SrTiO}_3)_{n-1}(\text{BaTiO}_3)_1\text{SrO}$ under tensile strain, the polarization lies in the plane of the film and decreases near the $(\text{SrO})_2$ boundary where the perovskite unit cell shifts by $\frac{1}{2}a[110]$ breaking the ferroelectric Ti-O chain¹⁵. In addition to enhancing the polarization, confining the barium to a single layer far from the $(\text{SrO})_2$ shear planes is advantageous to minimize the likelihood of forming secondary phases. $\text{Ba}_{n+1}\text{Ti}_n\text{O}_{3+1}$ is metastable in the Ruddlesden-Popper structure, with the non-perovskite barium orthotitanate (Ba_2TiO_4) being the lowest energy phase;¹⁶⁻²⁰ indeed no barium-containing Ruddlesden-Popper titanates are known to form in bulk and the

$(\text{SrTiO}_3)_{n-1}(\text{BaTiO}_3)_1\text{SrO}$ phases that we have targeted lie in a two-phase region of the BaO-SrO-TiO₂ pseudoternary phase diagram²¹. Nevertheless, as we show below, these artificial phases can be engineered using oxide molecular-beam epitaxy (MBE).

BaTiO₃ and SrTiO₃ have long been studied for tunable dielectric properties in the form of $(\text{Ba,Sr})\text{TiO}_3$ ²². The tunability in $(\text{Ba,Sr})\text{TiO}_3$, strained $(\text{SrTiO}_3)_n\text{SrO}$, and our new compound $(\text{SrTiO}_3)_{n-1}(\text{BaTiO}_3)_1\text{SrO}$ arises from the dipole created from the titanium – oxygen bonds in the ferroelectric materials' paraelectric state, which can be reversibly altered through an applied electric field, changing the permittivity. The highest tunability is found when the titanium – oxygen interatomic potential well is widest, occurring just above the ferroelectric Curie temperature, T_C ²². $(\text{Ba,Sr})\text{TiO}_3$ has proven exceptionally useful for tunable dielectrics and microwave devices²³ due to its ease of fabrication and ability to manipulate T_C , through the Ba:Sr ratio, spanning 403 K for BaTiO₃²⁴ to 0 K for SrTiO₃. Unfortunately $(\text{Ba,Sr})\text{TiO}_3$ has high dielectric losses ($\tan\delta > 0.02$) above 10 GHz due to charged point defects^{22,25}, making millimeter-wave applications energy inefficient and impracticable. Recently we showed that inserting additional SrO layers into strained SrTiO₃, forming $(\text{SrTiO}_3)_n\text{SrO}$ Ruddlesden-Popper superlattices²⁶⁻²⁸, led to defect mitigation and low loss²⁹⁻³², precipitating the highest recorded figure of merit for all known tunable dielectrics¹¹. Although this built an understanding of how to control losses in ferroelectrics, we could only grow films 50 nm thick before film relaxation began to occur and the electrical properties degraded. Expanding what was achieved by strain engineering beyond the limits of pure epitaxial strain would facilitate the synthesis of these high-performing tunable dielectrics on common commercial substrates and allow films to be grown to an

arbitrary thickness to optimize tunability. These outcomes are essential for the real implementation of tunable dielectric materials in millimeter wave electronics.

Growth and Structural Characterization

To compare to our previous $(\text{SrTiO}_3)_n\text{SrO}$ work¹¹, $n = 2-6$ $(\text{SrTiO}_3)_{n-1}(\text{BaTiO}_3)_1\text{SrO}$ films of the same thickness, 50 nm, and on the same substrate, (110) DyScO_3 ($a_p \approx 3.949 \text{ \AA}$)³³, were grown via MBE, as well as a 100 nm thick $n = 6$ $(\text{SrTiO}_3)_{n-1}(\text{BaTiO}_3)_1\text{SrO}$ film. The structural quality of the films is important to obtain the lowest loss devices and was examined using four-circle x-ray diffraction (XRD) (Figure 2.2a). The films show clear periodicity with expected out-of-plane lattice constants in θ - 2θ scans, implying that the films are single phase. Rocking curves in ω were measured (Supplementary Figure 2.6) and the films were found to have full-width at half-maximum (FWHM) values comparable to that of the underlying substrate, verifying the structural perfection and commensurate epitaxial growth.

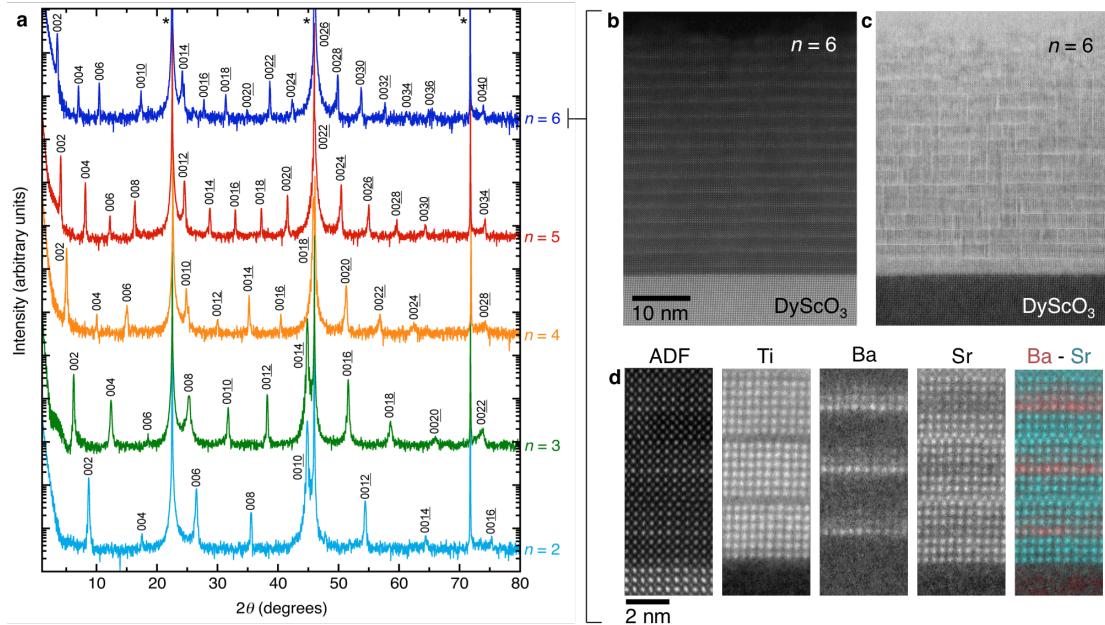


Figure 2.2 Structural characterization of ~ 50 nm thick epitaxial $(\text{SrTiO}_3)_{n-1}(\text{BaTiO}_3)_1\text{SrO}$ films with $n = 2-6$ grown on (110) DyScO_3 substrates. **a** θ - 2θ scans of the 50 nm thick $n = 2-6$ $(\text{SrTiO}_3)_{n-1}(\text{BaTiO}_3)_1\text{SrO}$ films grown on (110) DyScO_3 . Substrate peaks are labeled with an asterisk (*), **b** High-angle annular dark-field STEM image of the 50 nm thick $n = 6$ sample whose XRD is shown in dark blue in **a**, **c** Bright-field STEM image of the same $n = 6$ film, **d** ADF and STEM electron energy-loss spectroscopy (STEM-EELS) images of the same $n = 6$ region showing the elemental distributions from the Ti- $L_{2,3}$ edge, the Ba- $M_{4,5}$ edge and the Sr- $L_{2,3}$ edge, with a colour overlay of the barium signal in red and the strontium in teal. The barium shows 1-2 unit cells of interdiffusion to higher layers in the crystal structure, i.e., in the direction of growth.

To investigate the placement of the metastable BaO layer into the $(\text{SrTiO}_3)_{n-1}(\text{BaTiO}_3)_1\text{SrO}$ phases we used scanning transmission electron microscopy (STEM) on a cross-sectional specimen projecting through a $\{100\}$ plane. The brighter, periodic barium layers could be seen in the high-angle annular dark-field (STEM-HAADF) image (Figure 2.2b) and we observed the brick and mortar structure of the Ruddlesden-Popper superlattice in the bright field STEM image (Figure 2.2c) indicating the presence of $(\text{SrO})_2$ layers accommodating local non-stoichiometry. To

map the elemental distributions we used electron energy-loss spectroscopy (EELS) (Figure 2.2c). The result shows some barium diffusion along the direction of growth (the up direction in Figure 2.2b-d) due to barium overabundance or interdiffusion between strontium and barium layers at the high deposition temperature. The $(\text{SrO})_2$ layers were found to not accommodate any barium except at corners where two perpendicular $(\text{SrO})_2$ layers meet (Supplementary Figure 2.7). We did not observe any secondary phases, indicating that higher barium concentrations are likely possible in this artificial material, i.e., $(\text{SrTiO}_3)_{n-1}(\text{BaTiO}_3)_m\text{SrO}$ phases with $m > 1$.

Results

Ferroelectric Measurements

For electric-field tunable dielectrics, the highest tunability is found near the ferroelectric transition temperature, T_C , in the paraelectric phase of the material. To identify T_C of these new phases, the in-plane permittivity of the films was measured as a function of temperature and frequency (Figure 2.3a) on a cryogenic probe station using gold interdigitated electrodes with a chromium adhesion layer patterned directly on the film surface^{34,35}. $(\text{SrTiO}_3)_{n-1}(\text{BaTiO}_3)_1\text{SrO}$ phases with $n = 2-3$ show little ferroelectric behavior while $(\text{SrTiO}_3)_{n-1}(\text{BaTiO}_3)_1\text{SrO}$ phases $n = 4-6$ show relaxor-like ferroelectric behavior due to the separation of the ferroelectric perovskite blocks by $(\text{SrO})_2$ layers, preventing the propagation of the Ti-O ferroelectric chain through the film and isolating the perovskite blocks to an environment similar to ultra-thin films¹⁵. The peak in the in-plane dielectric constant curve with temperature, T_C , indicates the onset of ferroelectricity. By increasing n , the thickness of the perovskite layer, the polar mode emerges and strengthens¹⁵, increasing T_C (see ferroelectric

hysteresis loops in Supplementary Figure 2.11). Compared to the pure $(\text{SrTiO}_3)_n\text{SrO}$ phase in Figure 2.3b, the T_C of the $(\text{SrTiO}_3)_{n-1}(\text{BaTiO}_3)_1\text{SrO}$ phases are lower as explained by the first-principles calculations below.

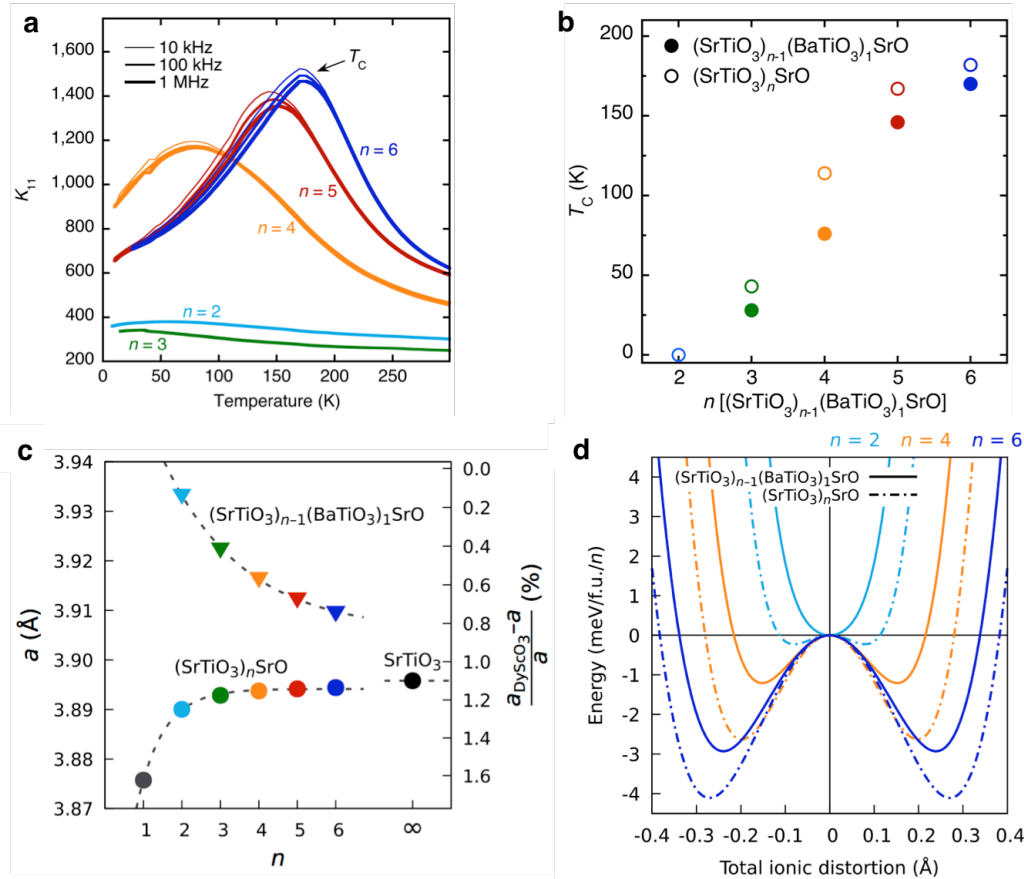


Figure 2.3 Emergence of ferroelectricity in $(\text{SrTiO}_3)_{n-1}(\text{BaTiO}_3)_1\text{SrO}$ films grown on (110) DyScO_3 . **a** In-plane dielectric constant (K_{11}) measurement as a function of temperature of the $n = 2-6$ $(\text{SrTiO}_3)_{n-1}(\text{BaTiO}_3)_1\text{SrO}$ films that are about 50 nm film thick and are grown on (110) DyScO_3 substrates. **b** A comparison in the T_C of $(\text{SrTiO}_3)_{n-1}(\text{BaTiO}_3)_1\text{SrO}$ films taken from the peak in (a) at 10 kHz (closed circles) to $(\text{SrTiO}_3)_n\text{SrO}$ (open circles). **c,d** First-principles calculations showing how the index n can be used to control the local ferroelectric instability of $(\text{SrTiO}_3)_{n-1}(\text{BaTiO}_3)_1\text{SrO}$ and $(\text{SrTiO}_3)_n\text{SrO}$ phases strained commensurately to (110) DyScO_3 substrates. **c** Equilibrium lattice parameter for the Ruddlesden-Popper compounds in the parent space group $I4/mmm$ (left axis), and the tensile strain imposed when they are grown on (110) DyScO_3 (right axis). **d** Potential energy surfaces for the in-plane polar distortion (space group $F2mm$) for the $n = 2, 4, 6$ compounds with and without barium.

First-principles calculations - the Strain Effect of Barium

Our experimental observations are consistent with density functional theory (DFT) calculations of the ferroelectric energy landscape (Methods), which show that the double-well potentials that mediate ferroelectricity are shallower for the Ba-containing $(\text{SrTiO}_3)_{n-1}(\text{BaTiO}_3)_1\text{SrO}$ compounds than for the pure $(\text{SrTiO}_3)_n\text{SrO}$ materials with the same n (Figure 2.3d). This is consistent with a reduction of the tensile strain from $\sim 1.1\%$ to $0.1\text{--}0.8\%$ when the former materials are grown on (110) DyScO_3 (Figure 2.3c). A spontaneous in-plane polarization emerges for $n \geq 4$ in the Ba-containing compounds, and for $n \geq 3$ in the pure SrTiO_3 -based Ruddlesden-Poppers as previously reported^{11,15}. Our calculations suggest that this is not solely an effect of epitaxial strain, since the pure SrTiO_3 -based compounds subject to the same epitaxial strains as the Ba-containing analogs ($0.1\text{--}0.8\%$ tensile) are found to have a smaller polarization. Figure 1 demonstrates this for the $n = 6$ case, where at first a reduction in strain from 1.1% (Figure 2.1b) to 0.8% (Figure 2.1c) for the pure SrTiO_3 compound leads to a decrease in polarization from 24 to $18 \mu\text{C cm}^{-2}$. If the strain lowering is instead done by substituting barium for strontium, a higher value of $22 \mu\text{C cm}^{-2}$ is predicted for the $n = 6$ compound on (110) DyScO_3 (Figure 2.1d). The layer-resolved polarization and in-plane atomic displacements show that this happens through a redistribution of the polar displacements, where the polarization is reduced in the BaO layer are restricted compared to the pure SrTiO_3 case at the same strain, but enhanced in all other layers. In Figure 2.1e we also track the *out-of-plane* displacements of each SrO and TiO_2 layer as a function of the distance from the BaO layer in the middle of the perovskite block, comparing the Ba-containing compound to

the pure SrTiO₃-based superlattice. The atomic displacements have both a "global" contribution from the expanded out-of-plane lattice parameter, and a "local" contribution from the strain field around the BaO layer. Figure 2.1e shows that the local part falls off rapidly away from the BaO layer, essentially reaching zero at the (SrO)₂ shear plane. This local strain field arises because Ba is confined to an atomically thin layer, thereby creating a targeted chemical pressure. In support of this, we performed calculations where the virtual crystal approximation (VCA) was used to simulate the effect of Ba being randomly distributed within the perovskite block (supplementary information). This systematically lead to lower calculated polarizations, highlighting that precise layering of BaO is the optimal strategy for realising low-loss tunable dielectric films with moderate epitaxial strains.

Millimeter-Wave Devices

Controlling dielectric losses and subsequent overall energy efficiency is crucial for high-frequency radio device implementation. As an example, if a device with a 1 GHz operating frequency provides 60 minutes of transmission time for a given battery life, then a device with the same efficiency (Joules/bit) and battery life operating at 60 GHz will only transmit for one minute. For many millimeter-wave applications—multiple input multiple output, beam-forming, full duplex, frequency agility—better materials are requisite for the development of usable, efficient components.

To test the applicability of these materials to millimeter-wave devices, we examined a 100 nm thick $n = 6$ (SrTiO₃)_{*n*-1}(BaTiO₃)₁SrO sample at 300 K, measuring the real and imaginary parts of the in-plane permittivity (Methods) from 600 Hz to 110 GHz (Figure 2.4a, Supplementary Figure 2.14). The minimal observed dispersion

throughout the measured frequency range mirrors the performance of the previously reported $(\text{SrTiO}_3)_n\text{SrO}$ films, and indicates that any major relaxation phenomena likely occur at frequencies above 110 GHz. The inset in Figure 2.4a shows a steady increase in the loss tangent in the millimeter-wave regime up to 0.06 at 110 GHz. We primarily attributed similar loss behavior in the $(\text{SrTiO}_3)_n\text{SrO}$ materials to the presence of polar nanoregions with a finite distribution of sizes¹¹. These films are not observed to be affected by the large relaxations in the gigahertz regime that appear in $(\text{Ba,Sr})\text{TiO}_3$ due to charged point defects, supporting the idea that the defect mitigating nature of the $(\text{SrTiO}_3)_n\text{SrO}$ Ruddlesden-Popper system is remains intact in the $(\text{SrTiO}_3)_{n-1}(\text{BaTiO}_3)_1\text{SrO}$ phases.

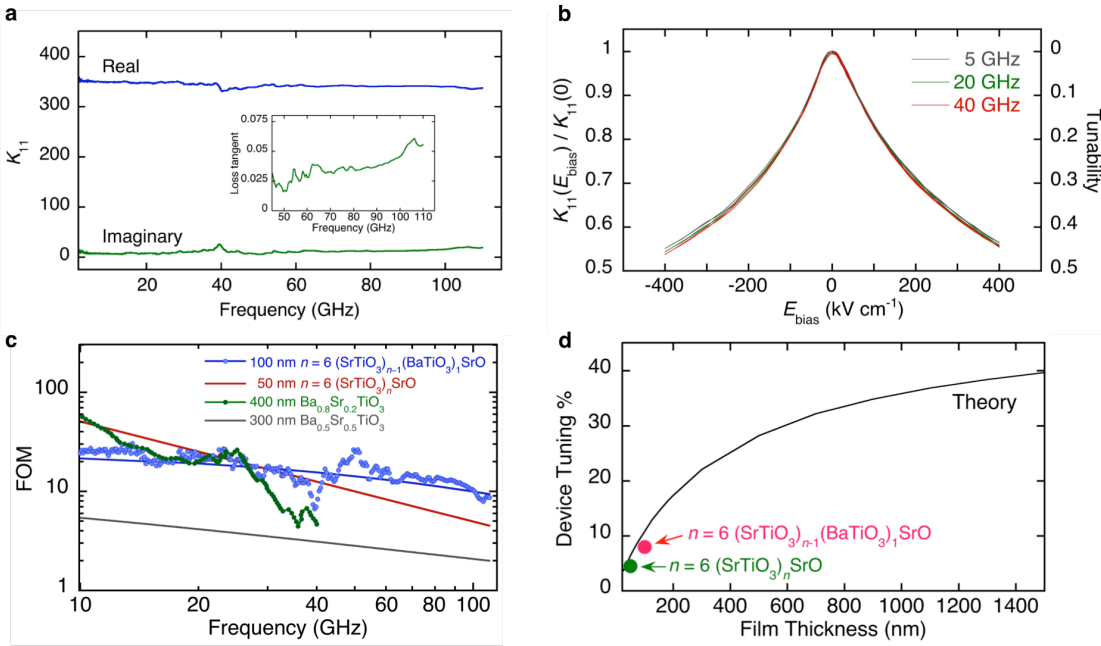


Figure 2.4 In-plane dielectric constant (K_{11}) of 100 nm $n = 6$ $(\text{SrTiO}_3)_{n-1}(\text{BaTiO}_3)_1\text{SrO}$ film on (110) DyScO_3 , and its tunability at room temperature and high frequency. a Real and imaginary parts of K_{11} as a function of frequency for the 100 nm thick $n = 6$ film. The inset shows the film loss tangent on a

linear frequency scale in the microwave frequency regime. **b** The ratio of K_{11} under an applied bias field (E_{bias}) to zero bias field (left-hand axis) and tunability (right-hand axis) of the $n = 6$ sample at several different frequencies in the microwave range. The inset shows the broadband dielectric constant as a function of frequency for several values of applied E_{bias} . **c** Room-temperature FOM (blue) of the same 100 nm thick $n = 6$ sample at a bias field of 400 kV cm^{-1} , (red) of the 50 nm thick $n = 6$ $(\text{SrTiO}_3)_n\text{SrO}$ on (110) DyScO_3 sample at 50 kV cm^{-1} from ref. 11, (green) a $x = 0.8$ $\text{Ba}_x\text{Sr}_{1-x}\text{TiO}_3$ film at 500 kV cm^{-1} from ref. 38, and (gray) a $x = 0.5$ $\text{Ba}_x\text{Sr}_{1-x}\text{TiO}_3$ film at 300 kV cm^{-1} from ref. 37. The FOM of the $n = 6$ sample uses the measured loss tangent, but assumes the tunability is independent of frequency and is 46% at a bias of 400 kV cm^{-1} . **d** Device tuning as a function of film thickness for the $n = 6$ film. The solid points indicate the device tuning for the device geometries used in this measurement of the 50 nm thick $n = 6$ $(\text{SrTiO}_3)_n\text{SrO}$ film grown on (110) DyScO_3 and the 100 nm thick $n = 6$ $(\text{SrTiO}_3)_{n-1}(\text{BaTiO}_3)_1\text{SrO}$ grown on (110) DyScO_3 substrates.

To study tunability, we applied a DC bias to our measurement devices at room temperature to induce reversible changes in the permittivity of a 100 nm thick $(\text{SrTiO}_3)_{n-1}(\text{BaTiO}_3)_1\text{SrO}$ $n = 6$ film. A maximum applied bias of 400 kV cm^{-1} reduced the dielectric constant of the film by more than 46% (Figure 2.4b). The tuning curve was not fully saturated, and no breakdown events were observed in the devices, indicating that tuning could be further increased with a large applied bias electric field. The resistance to breakdown observed in these thicker films is valuable for both achieving high tunability, as well as miniaturization: the material can withstand the increasing concentration of fields as the in-plane dimensions are reduced. The applied bias electric field was not found to alter the frequency dependence of the in the measured range from 100 MHz to 40 GHz (Supplementary Figure 2.15).

Tunable dielectrics are typically compared through a figure of merit (Figure 2.4c), which combines two salient features of these materials: the percent tuning and the quality factor³⁶. This FOM multiplies the material quality factor, $Q = 1/\tan \delta$, by

the relative tuning $(K_{11}(E_0) - K_{11}(E_{\max}))/K_{11}(E_0)$, which is 46% for the $n = 6$ film (Methods). E_0 represents no applied field, and E_{\max} represents the maximum applied bias electric field. Also shown in Figure 2.4c are the room temperature FOMs for the previously reported 50 nm $n = 6$ $(\text{SrTiO}_3)_n\text{SrO}$ superlattice grown on (110) DyScO_3 ($E_{\max} = 50 \text{ kV cm}^{-1}$), and for thin films of the widely-used $\text{Ba}_x\text{Sr}_{1-x}\text{TiO}_3$ – in the paraelectric state with $x = 0.5$ and 300 nm thickness grown on (0001) sapphire, ($E_{\max} = 300 \text{ kV cm}^{-1}$)³⁷, and in the ferroelectric manifold-domain-wall-variant state with $x = 0.8$ grown on (110) SmScO_3 ($E_{\max} = 500 \text{ kV cm}^{-1}$)³⁸. The exceptional room-temperature performance of the $n = 6$ $(\text{SrTiO}_3)_{n-1}(\text{BaTiO}_3)_1\text{SrO}$ material at 5G-relevant frequencies ($> 10 \text{ GHz}$) is apparent, with a FOM of 25 at 10 GHz, and an impressive FOM of approximately 9 at 110 GHz, a 200% improvement compared to our previous record-breaking work¹¹.

Implementation of low-loss, highly tunable films in millimeter-wave devices does not depend on the amount of tuning achieved in the thin film itself, but rather depends on the total tuning of the device, of which the film is only a minute portion. For planar device geometries, the low volume of thin films results in most of the electric field being concentrated in the inactive substrate. Thicker films boost the contribution of the film to the total distributed capacitance of the device, and therefore increase the total device tuning. Simulations of a range of film thicknesses were generated to illustrate how the total device tuning increases with film thickness for a constant film tunability (Figure 2.4d), in this case the tunability achieved in the $n = 6$ $(\text{SrTiO}_3)_{n-1}(\text{BaTiO}_3)_1\text{SrO}$ film. The definition of device tuning is geometry specific, and for the planar capacitor devices used here it is defined as

$(C_{\text{total}}(E_0) - C_{\text{total}}(E_{\text{max}}))/C_{\text{total}}(E_0)$, where C_{total} is the total distributed capacitance of the waveguide. Our previous $(\text{SrTiO}_3)_n\text{SrO}$ 50 nm planar devices produce a device tuning of less than 5%. In this case, the 100 nm thick $n = 6$ $(\text{SrTiO}_3)_{n-1}(\text{BaTiO}_3)_1\text{SrO}$ film doubled the device tuning to approximately 8% (Figure 2.4d). Film thickness becomes an additional parameter that can be optimized for device tunability.

Discussion

In conclusion, single layers of BaTiO_3 were incorporated into $(\text{SrTiO}_3)_n\text{SrO}$ Ruddlesden-Popper superlattices to impose targeted chemical pressure, which provides a technique to surpass the conventional limitations imposed on strain-engineered films by the introduction of defects beyond a critical thickness. The resulting tunable millimeter-wave dielectric was observed to have record-setting performance with a 200% improvement in FOM at 110 GHz compared to the prior best material ($(\text{SrTiO}_3)_n\text{SrO}$ with $n = 6$ commensurately strained to (110) DyScO_3). Future work will examine film integration on a wider variety of substrates. The $(\text{SrTiO}_3)_{n-1}(\text{BaTiO}_3)_1\text{SrO}$ Ruddlesden-Popper series of phases provides a pathway for future optimization of artificial complex materials and for advanced growth methods to achieve the application of viable millimeter-wave active tunable dielectrics in tunable electronics.

Methods

Oxide Molecular-Beam Epitaxy Growth. The $n = 2-6$ $(\text{SrTiO}_3)_{n-1}(\text{BaTiO}_3)_1\text{SrO}$ phases were grown using a Veeco GEN10³⁹ oxide molecular-beam epitaxy system at

875 °C in 1×10^{-6} Torr (1.3×10^{-4} Pa) $O_2 + \sim 10\%$ O_3 oxidant background pressure. The films were grown ~ 50 nm thick on (110) $DyScO_3$ substrates ($a_p \approx 3.949$ Å)³³. Atomic layering was achieved by elemental source shuttering and careful calibration of individual SrO, TiO₂, and BaO monolayer shutter times using reflection high-energy electron diffraction (RHEED) intensity oscillations^{40,41}.

Dielectric Measurements with Temperature. Interdigitated capacitors (IDCs) were photolithographically patterned on the 50 nm $n = 2-6$ $(SrTiO_3)_{n-1}(BaTiO_3)_1SrO$ thin films grown on (110) $DyScO_3$ using thermally evaporated electrodes, 100 nm gold on a 10 nm chromium adhesion layer. The IDC array contained electrodes with finger lengths of 500 μm, finger widths of 5 μm, with finger gaps 6, 10, or 15 μm, and the number of fingers 34, 24, or 20 respectively. An LCR meter coupled with a cryogenic station cooled with liquid helium was used to measure capacitance and resistance of the IDC. The capacitance and resistance was converted to the dielectric constant and loss using the techniques described in references [34] and [35]. Ferroelectric measurements seen in Supplementary Figure 2.11 were measured using the same cryogenic station and IDCs using a commercial ferroelectric tester.

Summary of First-Principles Calculations. All calculations were performed with the Vienna Ab-initio Software Package (VASP)^{42,43}, which implements the projector-augmented wave (PAW) formalism of density functional theory (DFT). We used PAW potentials with the valence electron configurations Sr ($4s^2 4p^6 5s^2$), Ba ($5s^2 5p^6 6s^2$), Ti ($3p^6 4s^2 3d^4$) and O ($2s^2 2p^4$), and expanded the wave functions in-plane waves

up to an energy cutoff of 550 eV. The Brillouin zone was sampled on a Monkhorst-Pack grid⁴⁴ of $8 \times 8 \times N_z$ k -points, where N_z , the number of k -points along z , ranged from 4 for the $n = 1$ Ruddlesden-Popper; $N_z = 2$ for $n = 2$ and 3, and $N_z = 1$ for $n \geq 4$. We relaxed the structures under conditions of fixed biaxial strain, until the Hellmann-Feynman forces on all atoms were below 0.1 meV/Å. All forces were calculated using an energy convergence of 10^{-8} eV. Following earlier theoretical work on SrTiO₃-based Ruddlesden-Poppers^{15,11}, we simulated epitaxial growth on (110) DyScO₃ by fixing the in-plane lattice parameter of the Ruddlesden-Popper structures to 3.9386 Å, 1.1% larger than the theoretical (PBEsol) lattice parameter for SrTiO₃ (3.8958 Å). The structures were relaxed keeping the lattice parameters fixed in the ab -plane, while the c lattice parameter and all internal coordinates were allowed to relax. Phonon calculations were done with Phonopy⁴⁵, which implements the finite displacement method to calculate the force constant matrix, using forces calculated with VASP. We used displacements of ± 0.01 Å, and symmetrization of the force constant matrices. Only phonons at the Brillouin zone center (Γ) were considered. We are in this case concerned with the doubly degenerate in-plane polar phonons that transform like the two-dimensional irreducible representation (irrep) Γ_5^- of the parent space group $I4/mmm$ (irrep E_u in point group notation). Polar ground states were obtained by freezing in the phonon eigenvectors corresponding to unstable modes⁴⁶, and relaxing the structures under the same fixed biaxial strain conditions as before. There are three symmetry-inequivalent order parameter directions (OPDs) for the Γ_5^- irrep, corresponding to the isotropy subgroups $F2mm$, $I2mm$ and Cm ⁴⁷, where we only considered $F2mm$ further as we found it to have the lowest energy. This OPD

corresponds in real space to polar displacements in the [110] direction referred to the parent space group.

mmWave Device Fabrication and Measurement. The broadband dielectric properties of the $n = 6$ thin film sample were determined over a frequency range from 500 Hz to 110 GHz, through complex Scattering (S -) parameter measurements of various planar microelectronic circuit devices patterned directly on the surface of the thin-film sample chip. The circuit devices were patterned via mask-less UV photolithography followed by electron-beam evaporation of a 10 nm titanium adhesion layer and a 500 nm gold electrode layer. The individual devices were completed with a lift-off step, to remove the excess metal and remaining photoresist, followed by a gentle cleaning in standard solvents and a light oxygen plasma. Below 100 MHz, the S -parameters of a series of four interdigitated capacitors (IDCs) with active lengths ranging from 0.210 mm to 2.910 mm were measured and used to determine the admittance per unit length of the IDC structures. IDC cross-sections were comprised of three 20 μm -wide fingers, separated by 5 μm -wide gaps, as well as 200 μm -wide ground planes, spaced 20 μm away from the outer fingers of the IDCs (Supplementary Figure 2.13a). The IDC measurements were performed using two different instruments: an LCR meter (500 Hz to 1 MHz) and a radiofrequency vector network analyzer (RF VNA, 500 kHz to 200 MHz). The LCR meter was calibrated using a built-in two-standard Open-Short calibration, while the RF VNA was calibrated using on-wafer Open-Short-Load-Thru (OSLT) standards. From 100 MHz to 110 GHz, the complex S -parameters of co-planar waveguide (CPW) devices were

measured with a high-frequency vector network analyzer (HF VNA). The CPW cross-section consisted of a 20 μm -wide center conductor, a 5 μm -wide gap, and a 200 μm -wide ground plane (Supplementary Figure 2.13b). The thin-film chip contained seven lines with active lengths ranging from 0.420 mm to 7.500 mm. Line lengths were optimized to reduce uncertainty when applying the multiline-TRL (thru-reflect-line) calibration⁴⁸. A total of three chips are needed to complete a full measurement: a custom reference calibration chip with consistent behavior, a companion (110) DyScO₃ substrate (Supplementary Figure 2.13c), and the thin-film chip with the film deposited on (110) DyScO₃. Measurements were conducted on a temperature-controlled stage, and devices were contacted by ground-signal-ground microwave probes mounted on micro-positioners. In this case, the reference chip contained similar CPW and IDC devices patterned on a (001) LaAlO₃ substrate. An additional 12 nm PdAu layer was deposited on the reference chip to produce resistor standards. Series resistor standards were used alongside a series capacitor, symmetric reflect, and all CPW lines to perform the full calibration procedure which defines the reference impedance over a broad frequency range. The calibration is comprised of two tiers. In the first tier, a multiline-TRL calibration was performed using the NIST StatistiCal software package, which also uses a least-squares optimization routine to produce an estimate for γ_0 , the propagation constant of the lines on the reference chip⁴⁹. The propagation constant is defined as $\gamma_0 = \sqrt{R + i\omega L} \sqrt{G + i\omega C}$, where R is the distributed resistance per unit length, L is the distributed inductance per unit length, G is the distributed conductance per unit length, C is the distributed capacitance per unit length, and ω is the angular frequency. A lossless reference calibration substrate was

chosen with a constant C and negligible G in the measured range. The multiline-TRL calibration was compared with a subsequent series-resistor calibration which also provides an estimate for C , which is required to extract R and L , which describe the behavior of the Au conductors^{50,51}. The first-tier calibration produced error boxes that account for signal attenuation and phase shift in the network analyzers and cables, and other systematic effects like reflection at connector interfaces. In the second tier, all lines and a reflect standard were measured on the companion DyScO₃ chip and the thin-film chip, and multiline TRL was again used to refine the calibration with second-tier error boxes and perform de-embedding which shifts the reference planes to the probe tips. The resulting propagation constants for the companion substrate chip and the thin-film chip were further analyzed with the aid of finite element modeling to determine the dielectric properties. Device dimensions measured via optical microscopy and surface profilometry were used to generate 2D simulations of the relevant structures in ANSYS Maxwell 2D Extractor. First, the R and L terms were modeled, and the model was validated by comparing to an R and L determined via an impedance extraction approach. The simulated R and L were then used to extract the C and G from the measured propagation constant. The previously validated simulation was again used to develop a mapping function that relates the measured frequency dependent capacitance and conductance to the real (ϵ') and imaginary (ϵ'') parts of the in-plane complex permittivity, respectively. External bias tees were used to apply a DC bias voltage to the CPW structures up to 200 V, over the frequency range from 100 MHz to 40 GHz, corresponding to a maximum applied field of $E_{\max} = 400 \text{ kV cm}^{-1}$. Complex S -parameters were measured using a high-frequency VNA at applied

bias electric field points stepped in 5 kV cm^{-1} increments. The software used to implement the multiline-TRL calibration also provided estimates of the error (95% confidence intervals) in the propagation constant, γ , at each frequency point, and the series resistor calibration produced uncertainty estimates in the capacitance per unit length for the reference calibration chip. These uncertainties were propagated through the analysis to determine the corresponding relative uncertainty in the measurements of the dielectric permittivity (Supplementary Figure 2.14).

Acknowledgements

The work at Cornell was supported by the U.S. Department of Energy, Office of Basic Sciences, Division of Materials Sciences and Engineering, under Award No. DE-SC0002334. Sample preparation was in part facilitated by the Cornell NanoScale Facility, a member of the National Nanotechnology Coordinated Infrastructure (NNCI), which is supported by the National Science Foundation (Grant ECCS-1542081). Ferroelectric and dielectric measurements with temperature were conducted at the Center for Nanophase Materials Sciences, which is a DOE Office of Science User Facility. This work made use of Cornell Center for Materials Research Shared Facilities, which are supported through the NSF MRSEC program (DMR-1719875).

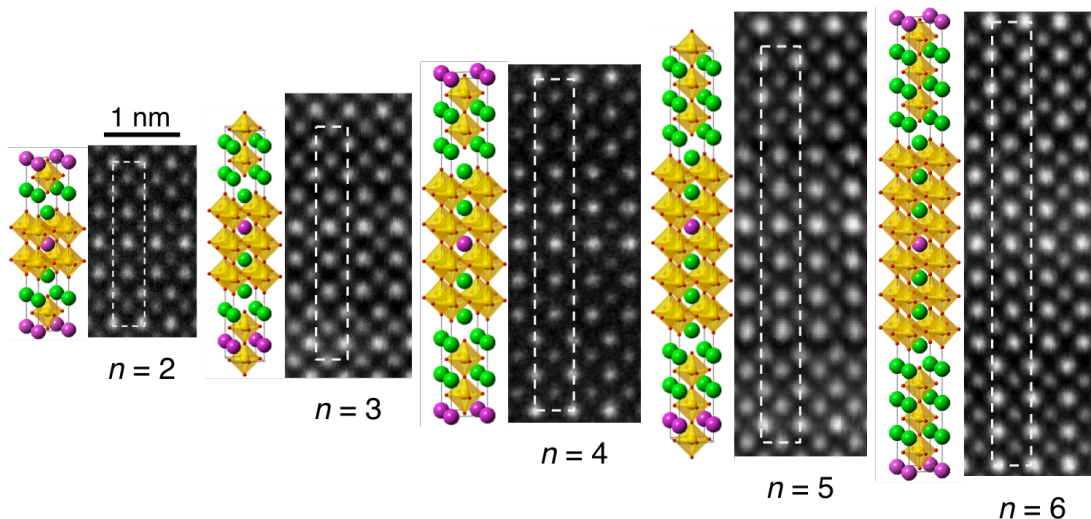
Contributions

N.M.D. and J.Z. synthesized the samples under the supervision of D.G.S. N.M.D. performed the ferroelectric and low frequency dielectric measurements with temperature. G.H.O. and C.J.F. performed the DFT calculations. M.E.H. performed STEM measurements under the supervision of D.A.M. mm-Wave devices were

fabricated and measured by E.J.M. and A.M.H. under the supervision of C.J.L., J.C.B. and N.D.O. N.M.D, D.G.S, E.J.M., A.M.H., N.D.O., G.H.O and M.E.H. wrote the manuscript. All authors discussed results and commented on the manuscript. The study was conceived and guided by D.G.S.

Supplementary Information

Applying Chemistry to Improve Today's Best Tunable Dielectric: The Inequivalence of Local and Global Strain

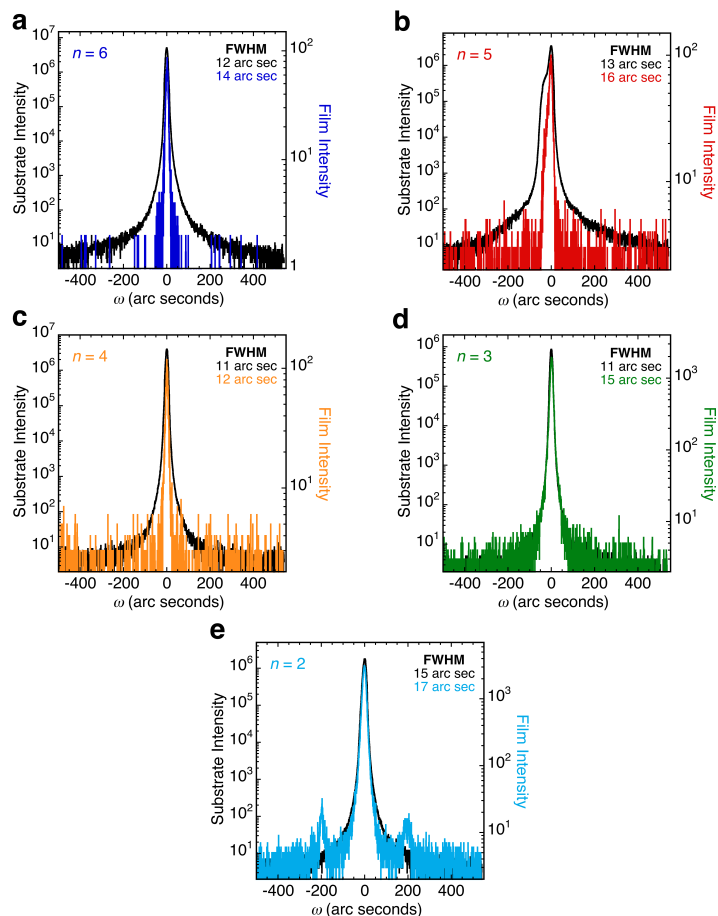


Supplementary Figure 2.5 Schematic of the crystal structure of $(\text{SrTiO}_3)_{n-1}(\text{BaTiO}_3)_1\text{SrO}$ phases for $n = 2-6$. Strontium atoms are shown in green, barium in pink, and the unit cells are outlined. To the right of each schematic is a STEM high-angle annular dark-field (HAADF) image of the corresponding 50 nm thick film grown on (110) DyScO₃ substrates.

X-Ray Diffraction Structural Characterization

From the four-circle x-ray diffraction θ - 2θ plots shown in the main article, Figure 2.2a, Nelson-Riley analysis⁵² was done to give c -axis lengths of 20.18 ± 0.02 Å, 28.25 ± 0.05 Å, 35.72 ± 0.05 Å, 45.02 ± 0.44 Å, and 51.38 ± 0.10 Å for $n = 2-6$ respectively. To confirm the high quality and epitaxy of the 50 nm thick $n = 2-6$ $(\text{SrTiO}_3)_{n-1}(\text{BaTiO}_3)_1\text{SrO}$ films grown on (110) DyScO₃, rocking curves in ω were measured shown in Supplementary Figure 2.6. All films were found to have full width at half maximums (FWHM) similar to the underlying substrate indicating high quality

and epitaxy.

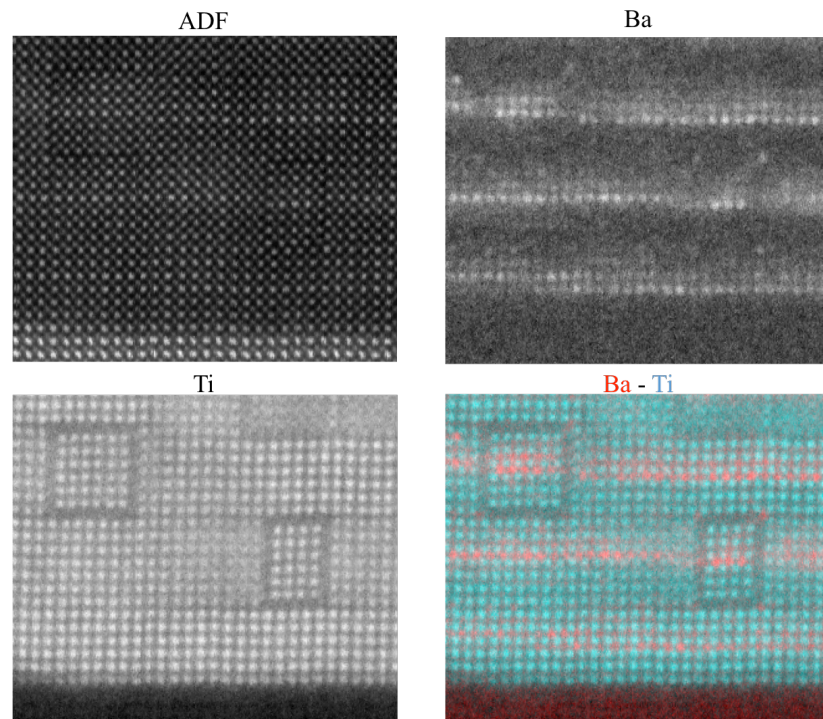


Supplementary Figure 2.6 ω rocking curves of 50 nm thick $(\text{SrTiO}_3)_{n-1}(\text{BaTiO}_3)_1\text{SrO}$ thin films grown on (110) DyScO_3 . Superimposed XRD rocking curves of the 220 peaks of the DyScO_3 substrate (shown in black) and selected film peaks of the $(\text{SrTiO}_3)_{n-1}(\text{BaTiO}_3)_1\text{SrO}$ $n = 2-6$ films: (a) $n = 6$ ($00\bar{2}8$ peak, blue). (b) $n = 5$ ($00\bar{2}4$ peak, red). (c) $n = 4$ ($00\bar{2}0$ peak, orange). (d) $n = 3$ ($00\bar{1}4$ peak, green). (e) $n = 2$ ($00\bar{1}0$ peak, light blue). The full width at half maximum (FWHM) is given as a measure of crystalline quality for the substrate and film peaks.

Transmission Electron Microscopy – Additional Data

Atomic-resolution scanning transmission electron microscopy, electron energy-loss spectroscopy (STEM-EELS) was performed to determine barium and strontium cation occupancy along the [001] growth direction of the 50 nm thick $n = 6$

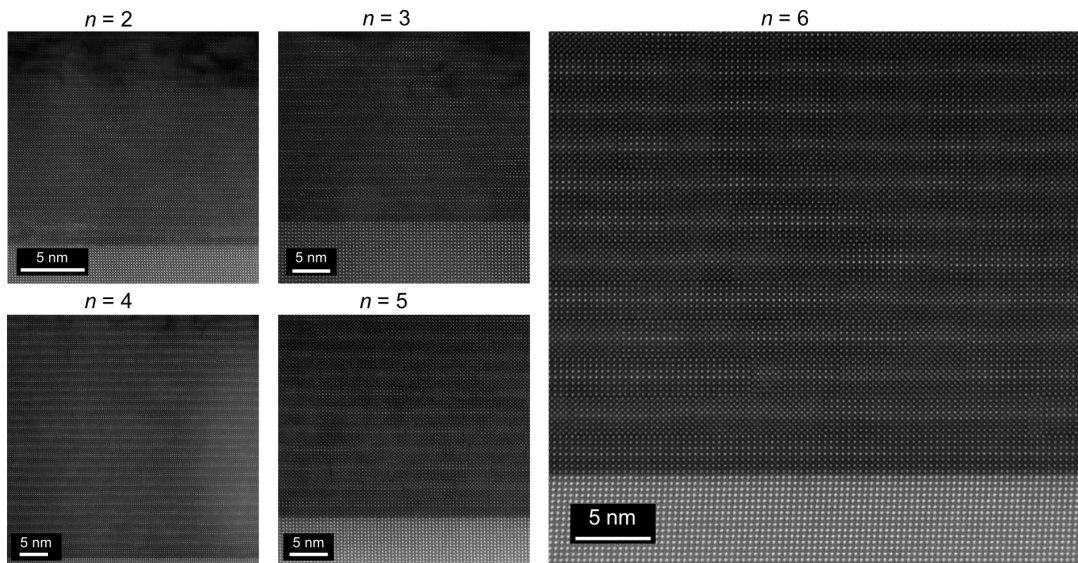
sample. High-angle annular dark-field (HAADF) STEM images and EELS spectroscopic images were recorded from cross-sectional TEM specimens using a 100 keV NION UltraSTEM⁵³, with a 30 mrad aperture and 100-200 pA of beam current. Spectroscopic images of barium (Ba- $M_{4,5}$), strontium (Sr- $L_{2,3}$), and titanium (Ti- $L_{2,3}$), were collected simultaneously using a Gatan⁵³ Dual EELS spectrometer with a dispersion of 0.25 eV/pixel. We find that the barium signal has diffused into the strontium sites 1-2 monolayers above the nominal barium layer. Additionally, we find that barium does not incorporate into the rock-salt SrO layers, except at a 90° bend in the rock stalk interface, where barium incorporates at the outermost of the corner (Supplementary Figure 2.7).



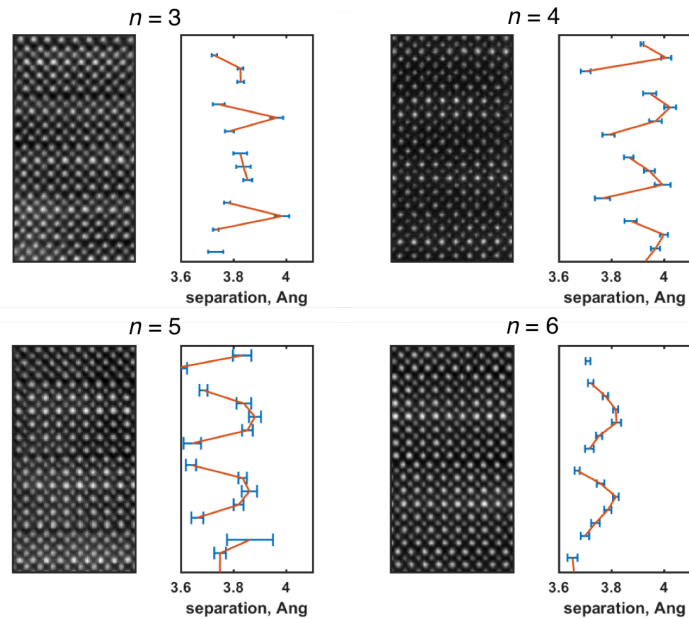
Supplementary Figure 2.7 STEM-EELS measurements of the $n = 6$ $(\text{SrTiO}_3)_{n-1}(\text{BaTiO}_3)_1\text{SrO}$ thin films. The simultaneously-acquired ADF, the barium signal, titanium signal, and a color overlay of the barium in red and the titanium in teal are shown. We see interdiffusion of the barium onto the strontium sites in the 1-2 unit

cells above the nominal barium layer, with no barium present in the rock-salt SrO layers except at 90° turns.

HAADF-STEM images were acquired in the 100 keV NION UltraSTEM⁵³ or the 300 keV Thermo Fisher Titan⁵³ for the $n = 2, 3, 4, 5$ and 6 samples (overview images in Supplementary Figure 2.8). By fitting the locations of the A -site positions, we can find the atomic unit cell spacing in the growth direction. As expected, we find that the addition of barium expands the lattice locally, as shown in Supplementary Figure 2.9.

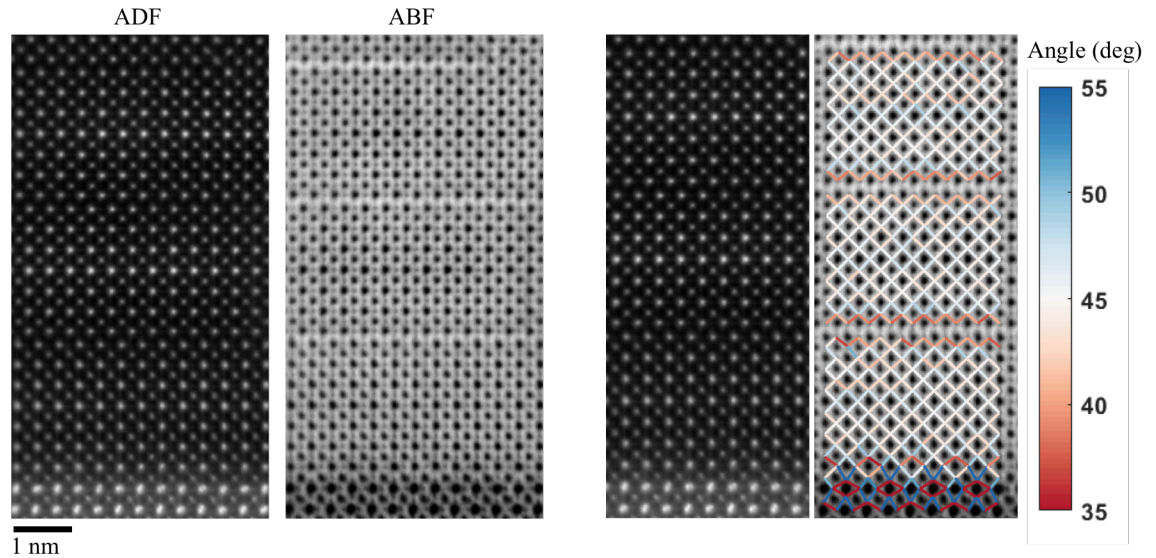


Supplementary Figure 2.8 Overview HAADF-STEM images of the 50 nm thick $n = 2-6$ $(\text{SrTiO}_3)_{n-1}(\text{BaTiO}_3)_1\text{SrO}$ films. All films show similar, uniform crystal structure (with some ion milling damage on the surface of the $n = 2$ and 3 samples).



Supplementary Figure 2.9 High magnification HAADF-STEM images of the $n = 3-6$ $(\text{SrTiO}_3)_{n-1}(\text{BaTiO}_3)_1\text{SrO}$ thin films. The c -axis spacing measured for the row is plotted on the right of the images, with the standard error of the measured values from each atomic column plotted as error bars. In the middle of the perovskite layer, where the barium is present, a larger lattice constant is observed.

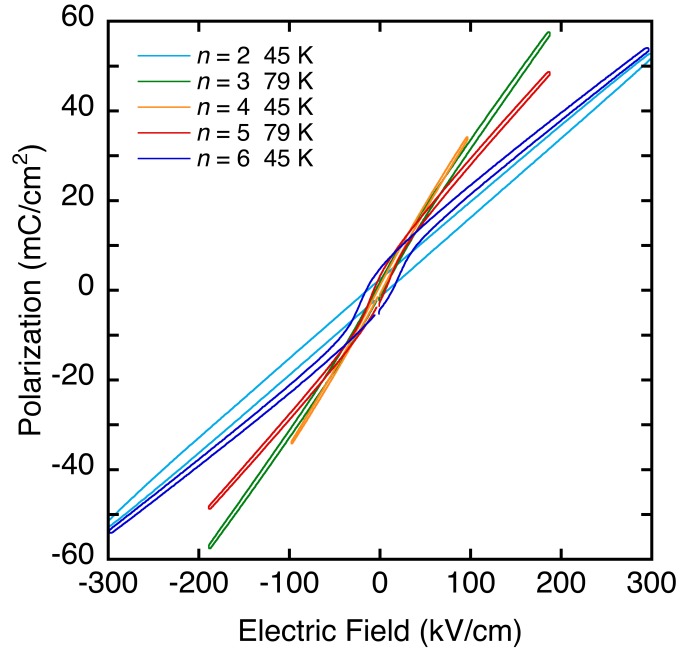
Annular bright field (ABF) images were acquired in the Titan⁵³ with a 30 mrad convergence angle and a 15-45 mrad collection angle for the $n = 6$ sample, shown in Supplementary Figure 2.10. As expected for room temperature measurements, no octahedral distortions are present in the perovskite layers, with a slight compression of the oxygen angle bonds at the rock salt layers. The octahedral rotations in the substrate (DyScO_3) propagate ~ 1 unit cell into the film.



Supplementary Figure 2.10 Annular dark field and annular bright field images of the 50 nm $n = 6$ $(\text{SrTiO}_3)_{n-1}(\text{BaTiO}_3)_1\text{SrO}$ compound. On the right-most panel, the oxygen-to-oxygen lines are drawn with the color corresponding to the angle of the bond – with white being 45 degrees. The octahedral tilts present in the DyScO_3 fall away within the first unit cell of SrTiO_3 in the film.

Ferroelectric Hysteresis Loops

To confirm the ferroelectric character of the 50 nm thick $n = 2-6$ $(\text{SrTiO}_3)_{n-1}(\text{BaTiO}_3)_1\text{SrO}$ films grown on (110) DyScO_3 , in-plane polarization hysteresis loops were measured at cryogenic temperatures shown in Supplementary Figure 2.11 (see methods). Clear hysteresis is seen only in samples $n = 4-6$. For sample $n = 2$, which shows an in-plane dielectric constant peak with temperature at around 50 K, at 45 K the sample does not show ferroelectric behavior, indicating a possible structural transition at this temperature.

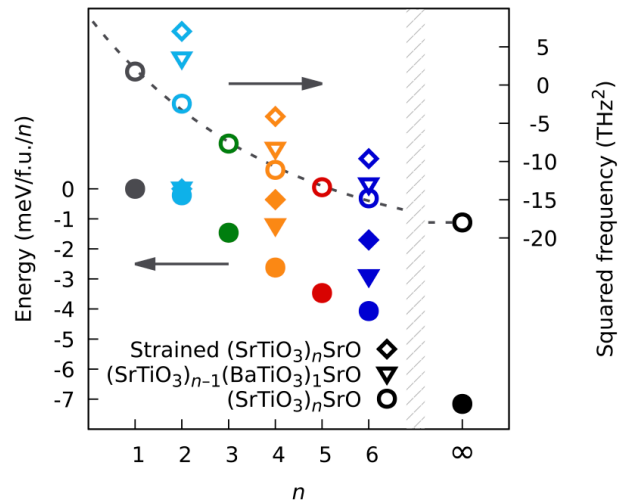


Supplementary Figure 2.11 Polarization versus applied electric field hysteresis loops of 50 nm $n = 2-6$ $(\text{SrTiO}_3)_{n-1}(\text{BaTiO}_3)_1\text{SrO}$ films grown on (110) DyScO_3 . The temperature at which the ferroelectric loop was measured is noted for each sample in the legend.

Density Functional Theory - Phonon frequencies and energy gains

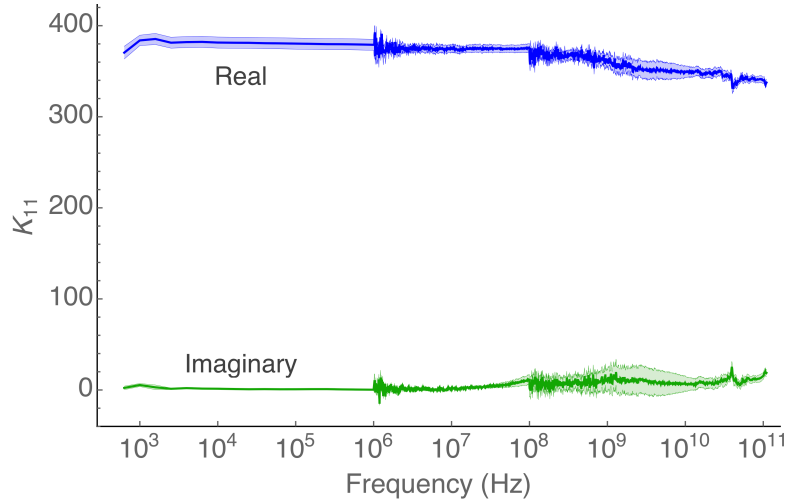
In Supplementary Figure 2.12 we show calculated phonon frequencies for all the $(\text{SrTiO}_3)_n\text{SrO}$ and $(\text{SrTiO}_3)_{n-1}(\text{BaTiO}_3)_1\text{SrO}$ compounds described in the manuscript, along with the energy difference between the $I4/mmm$ and $F2mm$ structures. Essentially this is a different perspective on the data in Figure 2.3d in the main text: The phonon frequencies are proportional to the curvature of the potential energy surfaces at their extrema, while the energy gains are the potential well depths (zero for the dynamically stable structures). In Supplementary Figure 2.12 we also give phonon frequencies and energy gains for $(\text{SrTiO}_3)_n\text{SrO}$ with $n = 1, 3,$ and 5 ; these were left out from Figure 2.3d in the interest of readability. In addition we have included data points for $(\text{SrTiO}_3)_n\text{SrO}$ strained to the same values as the Ba-containing

compounds (strain values given in Figure 2.3c in the main text). This demonstrates in a clear way how the attractive properties of the Ba-containing compounds result from a combination of strain engineering and chemistry: The $(\text{SrTiO}_3)_{n-1}(\text{BaTiO}_3)_1\text{SrO}$ films can be grown thicker than $(\text{SrTiO}_3)_n\text{SrO}$ due to being in a state of lower strain when grown on the DyScO_3 substrate; however, they also have stronger ferroelectric instabilities than the $(\text{SrTiO}_3)_n\text{SrO}$ films would have if they were tuned to the same lower strains by suitable substrates.

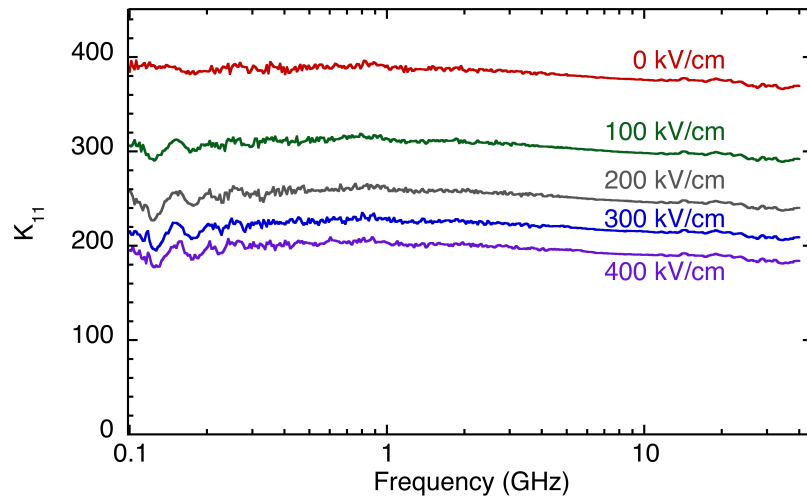


Supplementary Figure 2.12 Phonon frequencies and energy gains for the ferroelectric instabilities as a function of the perovskite layer thickness, n .

Phonon frequencies are shown in open symbols with corresponding values on the right axis and the ferroelectric instabilities are represented by filled symbols with values read from the left axis. Circles and triangles have the same meaning as in the main text **Figure 2.3**, and represent films grown on (110) DyScO_3 . Diamond symbols represent $(\text{SrTiO}_3)_n\text{SrO}$ films in strain states identical to those of the corresponding $(\text{SrTiO}_3)_{n-1}(\text{BaTiO}_3)_1\text{SrO}$ films grown on DyScO_3 as in **Figure 2.1c**.



Supplementary Figure 2.14 Broadband complex permittivity of the $n = 6$ $(\text{SrTiO}_3)_{n-1}(\text{BaTiO}_3)_1\text{SrO}$ thin film. The real part of K_{11} , the complex permittivity, of the $n = 6$ $(\text{SrTiO}_3)_{n-1}(\text{BaTiO}_3)_1\text{SrO}$ thin film is shown in blue, and the imaginary part which corresponds to the dielectric losses in the material is shown in green. This plot is an extension to lower frequency of **Figure 2.4a** in the main text, which highlighted the frequencies relevant for millimeter-wave electronic devices. The shaded regions around the curves correspond to the expanded 95% CI values.



Supplementary Figure 2.15 Tuning of the real part of the complex permittivity of the $n = 6$ $(\text{SrTiO}_3)_{n-1}(\text{BaTiO}_3)_1\text{SrO}$ thin film under an applied bias electric field. The real part of K_{11} is shown from 100 MHz to 40 GHz, with labels that correspond to the electric field applied across the CPW devices during the measurement.

References

1. Haeni, J. H. *et al.* Room-temperature ferroelectricity in strained SrTiO₃. *Nature* **430**, 758-761 (2004).
2. Haislmaier, R. C. *et al.* Unleashing Strain Induced Ferroelectricity in Complex Oxide Thin Films via Precise Stoichiometry Control. *Adv. Funct. Mater.* **26**, 7271–7279 (2016).
3. Béa, H. *et al.* Evidence for room-temperature multiferroicity in a compound with a giant axial ratio. *Phys. Rev. Lett.* **102**, 217603 (2009).
4. Yang, J. C. *et al.* Orthorhombic BiFeO₃. *Phys. Rev. Lett.* **109**, 247606 (2012).
5. Fennie, C. J. & Rabe K. M. Magnetic and electric phase control in epitaxial EuTiO₃ from first principles. *Phys. Rev. Lett.* **97**, 267602 (2006).
6. Lee, J. H. *et al.* A strong ferroelectric ferromagnet created by means of spin. *Nature* **466**, 954–958 (2011).
7. Jalan, B., Allen, S. J., Beltz, G. E., Moetakef, P. & Stemmer, S. Enhancing the electron mobility of SrTiO₃ with strain. *Appl. Phys. Lett.* **98**, 132102 (2011).
8. Marshall, P. B., Ahadi, K., Kim, H. & Stemmer, S. Electron nematic fluid in a strained Sr₃Ru₂O₇ film. *Phys. Rev. B* **97**, 155160 (2018).
9. Burganov, B. *et al.* Strain Control of Fermiology and Many-Body Interactions in Two-Dimensional Ruthenates. *Phys. Rev. Lett.* **116**, 197003 (2016).
10. Hsu, Y.-T. *et al.* Manipulating superconductivity in ruthenates through Fermi surface engineering. *Phys. Rev. B* **94**, 045118 (2016).
11. Lee, C.-H., *et al.* Exploiting dimensionality and defect mitigation to create tunable microwave dielectrics. *Nature* **502**, 532–536 (2013).
12. Neaton, J. B. & Rabe, K. M. Theory of polarization enhancement in epitaxial BaTiO₃/SrTiO₃ superlattices. *Appl. Phys. Lett.* **82**, 1586–1588 (2003).
13. Johnston, K., Huang, X., Neaton, J. B. & Rabe, K. M. First-principles study of symmetry lowering and polarization in BaTiO₃/SrTiO₃ superlattices with in-plane expansion. *Phys. Rev. B* **71**, 100103 (2005).
14. Tenne, D. A. *et al.* Probing Nanoscale Ferroelectricity by Ultraviolet Raman Spectroscopy. *Science* **313**, 1614–1616 (2006).

15. Birol, T., Benedek, N. A. & Fennie, C. J. Interface Control of Emergent Ferroic Order in Ruddlesden-Popper $\text{Sr}_{n+1}\text{Ti}_n\text{O}_{3n+1}$. *Phys. Rev. Lett.* **107**, 257602 (2011).
16. Bland, J. A. The crystal structure of barium orthotitanate, Ba_2TiO_4 . *Acta Crystallogr.* **14**, 875–881 (1961).
17. Suzuki, T., Nishi, Y. & Fujimoto, M. Ruddlesden–Popper Planar Faults and Nanotwins in Heteroepitaxial Nonstoichiometric Barium Titanate Thin Films. *J. Am. Ceram. Soc.* **83**, 3185–3195 (2000).
18. Fujimoto, M. & Suzuki, T. High-Resolution Transmission Electron Microscopy and Computer Simulation of Defect Structures in Electronic Perovskite Ceramics. *J. Ceram. Soc. Jpn.* **109**, 722–732 (2001).
19. Lee, S., Randall, C. A. & Liu, Z.-K. Modified Phase Diagram for the Barium Oxide–Titanium Dioxide System for the Ferroelectric Barium Titanate. *J. Am. Ceram. Soc.* **90**, 2589–2594 (2007).
20. Twigg, M. E., Alldredge, L. M. B., Chang, A., Podpirka, A., Kirchoefer, S. W., & Pond, J. M. Structure and composition of $\text{Ba}_{0.5}\text{Sr}_{0.5}\text{TiO}_3$ films deposited on (001) MgO substrates and the influence of sputtering pressure. *Thin Solid Films* **548**, 178–185 (2013).
21. Kwestroo, W. & Paping, H. A. M. The systems BaO–SrO– TiO_2 , BaO–CaO– TiO_2 , and SrO–CaO– TiO_2 . *J. Am. Ceram. Soc.* **42**, 292–299 (1959).
22. Tagantsev, A. K., Sherman, V. O., Astafiev, K. F., Venkatesh, J. & Setter, N. Ferroelectric Materials for Microwave Tunable Applications. *J. Electroceramics* **11**, 5–66 (2003).
23. Bao, P., Jackson, T. J., Wang, X. & Lancaster, M. J. Barium strontium titanate thin film varactors for room-temperature microwave device applications. *J. Phys. Appl. Phys.* **41**, 063001 (2008).
24. *Landolt-Börnstein: Numerical Data and Functional Relationships in Science and Technology*. 16a, (Springer, 1981).
25. Elissalde, C. & Ravez, J. Ferroelectric ceramics: defects and dielectric relaxations. *J. Mater. Chem.* **11**, 1957–1967 (2001).
26. Balz, D. & Plieth, K. Die Struktur des Kaliumnickelfluorids, K_2NiF_4 . *Z. Für Elektrochem. Berichte Bunsenges. Für Phys. Chem.* **59**, 545–551 (1955).
27. Ruddlesden, S. N. & Popper, P. New compounds of the K_2NiF_4 type. *Acta Crystallogr.* **10**, 538–539 (1957).

28. Ruddlesden, S. N. & Popper, P. The compound $\text{Sr}_3\text{Ti}_2\text{O}_7$ and its structure. *Acta Crystallogr.* **11**, 54–55 (1958).
29. Tilley, R. J. D. Correlation between dielectric constant and defect structure of non-stoichiometric solids. *Nature* **269**, 229–231 (1977).
30. Tilley, R. J. D. An electron microscope study of perovskite-related oxides in the Sr-Ti-O system. *J. Solid State Chem.* **21**, 293–301 (1977).
31. Cockroft, N. J., Lee, S. H. & Wright, J. C. Site-selective spectroscopy of defect chemistry in SrTiO_3 , Sr_2TiO_4 , and $\text{Sr}_3\text{Ti}_2\text{O}_7$. *Phys. Rev. B* **44**, 4117–4126 (1991).
32. Knott, L. J., Cockroft, N. J. & Wright, J. C. Site-selective spectroscopy of erbium-doped SrTiO_3 , Sr_2TiO_4 , and $\text{Sr}_3\text{Ti}_2\text{O}_7$. *Phys. Rev. B* **51**, 5649–5658 (1995).
33. Veličkov, B., Kahlenberg, V., Bertram, R. & Bernhagen, M. Crystal chemistry of GdScO_3 , DyScO_3 , SmScO_3 and NdScO_3 . *Z. Für Krist.* **222**, 466–473 (2009).
34. Gevorgian, S. S., Martinsson, T., Linner, P. L. J. & Kollberg, E. L. CAD models for multilayered substrate interdigital capacitors. *IEEE Trans. Microw. Theory Tech.* **44**, 896–904 (1996).
35. Kidner, N. J., Homrighaus, Z. J., Mason, T. O. & Garboczi, E. J. Modeling interdigital electrode structures for the dielectric characterization of electroceramic thin films. *Thin Solid Films* **496**, 539–545 (2006).
36. Xi, X. X. *et al.* Oxide thin films for tunable microwave devices. *J. Electroceram.* **4**, 393–405 (2000).
37. Houzet, G., Burgnies, L., Velu, G., Carru, J.-C. & Lippens, D. Dispersion and loss of ferroelectric $\text{Ba}_{0.5}\text{Sr}_{0.5}\text{TiO}_3$ thin films up to 110 GHz. *Appl. Phys. Lett.* **93**, 053507 (2008).
38. Gu, Z. *et al.* Resonant domain-wall-enhanced tunable microwave ferroelectrics. *Nature* **560**, 622–627 (2018).
39. Certain commercial equipment, instruments, or materials are identified in this paper to foster understanding. Such identification does not imply recommendation or endorsement by the National Institute of Standards and Technology, nor does it imply that the materials or equipment identified are necessarily the best available for the purpose.
40. Haeni, J. H., Theis, C. D. & Schlom, D. G. RHEED Intensity Oscillations for the Stoichiometric Growth of SrTiO_3 Thin Films by Reactive Molecular Beam Epitaxy. *J. Electroceramics* **4**, 385–391 (2000).

41. Haislmaier, R.C, Stone, G., Alem, N., & Engel-Herbert, R. Creating Ruddlesden-Popper phases by hybrid molecular beam epitaxy. *Appl. Phys. Lett.* **109**, 043102 (2016).
42. Kresse, G. & Furthmüller, J. Efficient iterative schemes for ab initio total-energy calculations using a plane-wave basis set. *Phys. Rev. B* **54**, 11169–11186 (1996).
43. Kresse, G. & Joubert, D. From ultrasoft pseudopotentials to the projector augmented-wave method. *Phys. Rev. B* **59**, 1758–1775 (1999).
44. Perdew, J. P. *et al.* Restoring the Density-Gradient Expansion for Exchange in Solids and Surfaces. *Phys. Rev. Lett.* **100**, 136406–136406 (2008).
45. Togo, A. & Tanaka, I. First principles phonon calculations in materials science. *Scr. Mater.* **108**, 1–5 (2015).
46. Togo, A. & Tanaka, I. Evolution of crystal structures in metallic elements. *Phys. Rev. B* **87**, 184104 (2013).
47. Stokes, H. T., Hatch, D. M. & Campbell, B. J. ISOTROPY Software Suite. Available at: iso.byu.edu.
48. Marks, R.B., A Multiline Method of Network Analyzer Calibration. *IEEE Trans. Microw. Theory Tech.* **39**, 1205-1215 (1991).
49. Williams, D.F., Wang, J.C.M. & Arz, U. An Optimal Vector-Network Analyzer Calibration Algorithm. *IEEE Trans. Microw. Theory Tech.* **51**, 2391-2401 (2003).
50. Williams, D.F., Marks, R.B. & Davidson, A. Comparison of On-Wafer Calibrations. *38th ARFTG Conf. Dig.* San Diego, CA. 68 – 81 (1991).
51. Orloff, N.D., *et al.* A Compact Variable-Temperature Broadband Series-Resistor Calibration. *IEEE Trans. Microw. Theory Tech.* **59**, 188-195 (2011).
52. Nelson, J. B. & Riley, D. P. An experimental investigation of extrapolation methods in the derivation of accurate unit-cell dimensions of crystals. *Proc. Phys. Soc.* **57**, 160 (1945).
53. Certain commercial equipment, instruments, or materials are identified in this paper to foster understanding. Such identification does not imply recommendation or endorsement by the National Institute of Standards and Technology, nor does it imply that the materials or equipment identified are necessarily the best available for the purpose.

Chapter 3
Off-stoichiometric defect accommodation in $(\text{SrTiO}_3)_n\text{SrO}$
Ruddlesden-Popper superlattices studied by positron
annihilation

Natalie M. Dawley¹, Werner Egger², David J. Keeble³, and Darrell G. Schlom^{1,4}

1. Department of Materials Science and Engineering, Cornell University, Ithaca, New York 14853, US

2. Peter Grünberg Institute, Forschungszentrum Jülich, 52425 Jülich, Germany

3. Carnegie Laboratory of Physics, SUPA, School of Engineering, Physics, and Mathematics, University of Dundee, Dundee DD1 4HN, United Kingdom

4. Kavli Institute at Cornell for Nanoscale Science, Ithaca, New York 14853, USA

Correspondence and requests for materials should be addressed to D.G.S. (email: schlom@cornell.edu)

Abstract

In the strained $(\text{SrTiO}_3)_n\text{SrO}$ Ruddlesden-Popper system, record breaking low dielectric loss was found in the gigahertz frequency range where charged point defects are known to dominate loss. It was posited that the unprecedented low loss was due to defect accommodation by the $(\text{SrO})_2$ Ruddlesden-Popper faults. In this paper we explore the effect of non-stoichiometric defects in the $(\text{SrTiO}_3)_n\text{SrO}$ system using positron annihilation lifetime spectroscopy on a composition series of 300 nm thick $n = 6$ $(\text{Sr}_{1+\delta}\text{TiO}_3)_n\text{SrO}$ on (001) SrTiO_3 . We find our $n = 6$ $(\text{Sr}_{1+\delta}\text{TiO}_3)_n\text{SrO}$ thin films show a dominant TiO_x vacancy with little change in defect populations across the series indicating the Ruddlesden-Popper material's ability to accommodate $\pm 5\%$ off-stoichiometry.

Defects play a key role in understanding and engineering materials. There has been recent interest in Ruddlesden-Popper superlattices for ferroelectrics¹⁻⁵, tunable dielectrics⁶, superconductivity⁷, and solid fuel cell⁸ applications without full elucidation of the defects in these materials. In the parent phase of the Ruddlesden-Popper $(\text{SrTiO}_3)_n\text{SrO}$, pure SrTiO_3 , intrinsic point defects can dramatically affect properties – oxygen reduced samples create n-type conduction⁹, off-stoichiometric point defects increase thermal conductivity^{10,11}, and ferroelectricity can emerge for ultrathin films due to intrinsic point defect nanopolarizations¹². The quantitative prediction^{13,14}, identification, and measurement of these defects in SrTiO_3 thin films has been challenging. For titanium-rich films it is known that there is a corresponding increase in strontium vacancies, titanium antisite defects, and amorphous TiO_2 -rich regions¹⁵⁻¹⁸. For strontium-rich SrTiO_3 , the defect mechanisms are less well understood. In bulk SrTiO_3 , $(\text{SrO})_2$ faults are observed with strontium excess of >0.01 at.%^{19,20}, forming disordered $(\text{SrTiO}_3)_n\text{SrO}$ Ruddlesden-Popper phases²¹⁻²³. When epitaxially strained these superlattice structures have the highest reported figure of merit for high frequency tunable dielectrics,⁶ counter to the high loss seen in their pure titanate counterparts. Loss at these gigahertz frequencies is caused by extrinsic defects²⁴⁻²⁶, notably charged point defects, indicating their absence in these superlattices.

In $(\text{SrTiO}_3)_n\text{SrO}$ Ruddlesden-Popper non-stoichiometric defects are hypothesized to be accommodated by the growth (for strontium excess) or reduction (for titanium excess) of $(\text{SrO})_2$ planar faults which have a lower formation energy cost than that of a point defect²⁷. Here using positron annihilation lifetime spectroscopy

(PALS) we test how Ruddlesden-Popper structures accommodate off-stoichiometry when $\text{Sr}_{1+\delta}\text{TiO}_3$ is inserted into an $n = 6$ $(\text{SrTiO}_3)_n\text{SrO}$ structure grown by molecular-beam epitaxy (MBE). We have used PALS in the past to examine pulsed-laser deposited 200 nm thick titanium-rich SrTiO_3 films and found a clear trend of the presence of both strontium and titanium vacancies^{16,17}. Strontium vacancies were found to dominate in titanium-rich films with a crossover to a higher proportion of titanium vacancies as the films became more stoichiometric. All films had vacancy concentrations >50 ppm.

Experiment

A range of compositions with $\delta \pm 5\%$ of 300 nm $n = 6$ $(\text{Sr}_{1+\delta}\text{TiO}_3)_n\text{SrO}$ films were grown on (001) SrTiO_3 . Films were made using a Veeco GEN10 oxide molecular-beam epitaxy chamber at a substrate temperature of 900 °C (as measured by the heating stage thermocouple) in an oxidant background pressure of 1×10^{-6} Torr O_2 + $\sim 10\%$ O_3 . Atomic layering was achieved by elemental source shuttering and calibration of individual SrO and TiO_2 monolayer shutter times using reflection high-energy electron diffraction (RHEED) intensity oscillations^{28,29}. The shutter times were then increased or decreased to achieve $\pm 5\%$ Sr/Ti ratio for an off-stoichiometric sample.

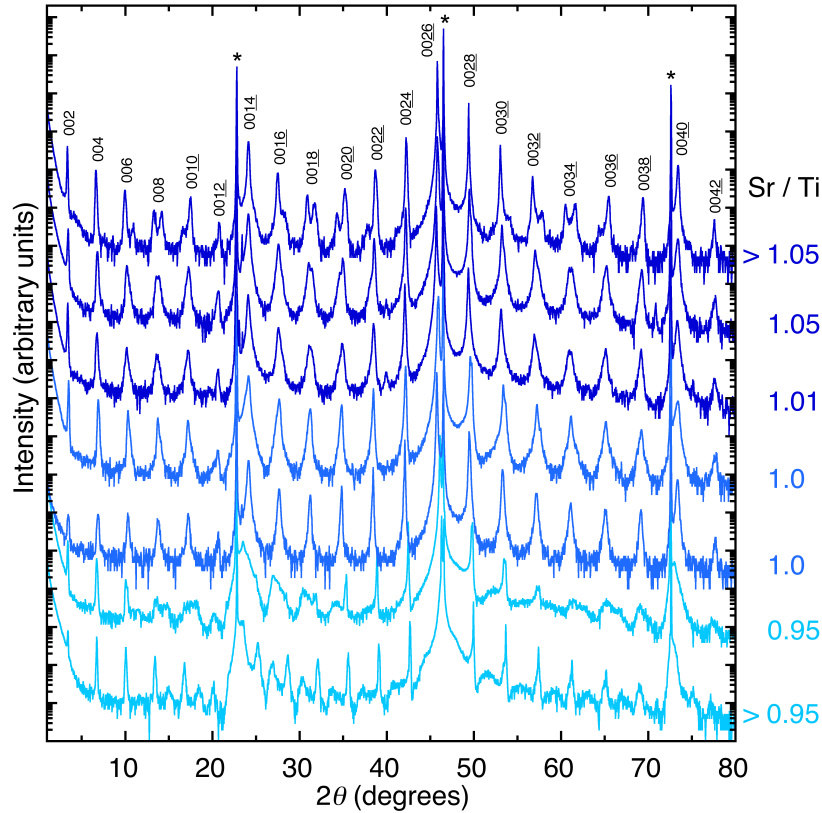


Figure 3.1 X-ray diffraction of $\delta \pm 5\%$ of 300 nm thick $n = 6$ $(\text{Sr}_{1+\delta}\text{TiO}_3)_n\text{SrO}$ films grown on (001) SrTiO_3 . The peak periodicity degrades with increasing off-composition. Substrate peaks are labeled with an asterisk (*).

Samples were characterized by x-ray diffraction seen in Figure 3.1. As the films become further off-stoichiometric the diffraction peaks begin to split, indicating a loss in superlattice periodicity. It is noted that this occurs more rapidly for titanium-rich films than those that are strontium-rich. All films have narrow ω rocking curves with full-width-at-half-maximum (FWHM) comparable to that of the underlying substrate < 34 arcsec (0.009°) (not shown). The low FWHM of these films attests to the defect accommodating nature of $(\text{SrTiO}_3)_n\text{SrO}$ despite some of the samples being off-stoichiometric by $> 5\%$. By Nelson-Riley analysis³⁰ these films have out-of-plane spacings that decrease with off-composition seen in Figure 3.2.

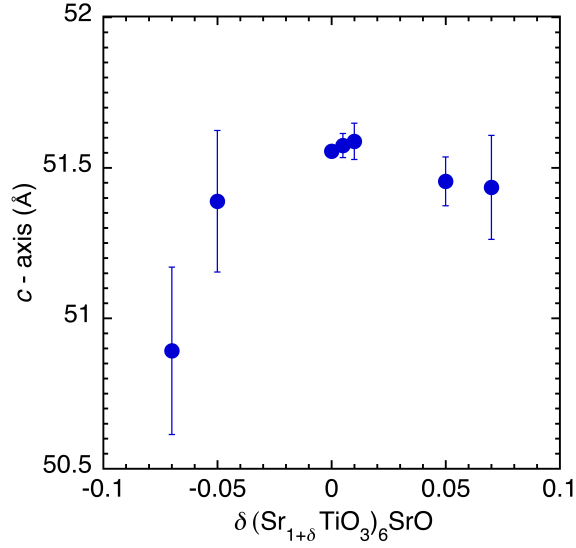


Figure 3.2 The c -axis of $n = 6$ $(\text{Sr}_{1+\delta}\text{TiO}_3)_n\text{SrO}$ films shown in **Figure 3.1** calculated by Nelson-Riley analysis. The c -axis is seen to decrease with off-composition while the error of the fit increases.

To identify vacancies in the $n = 6$ $(\text{Sr}_{1+\delta}\text{TiO}_3)_n\text{SrO}$ films we measured vacancy populations using variable-energy positron annihilation lifetime spectroscopy (VE-PALS). Positrons implanted in the films rapidly thermalize and then annihilate with a bulk lattice or defect state i , with a characteristic lifetime τ_i , and probability I_i . The positron annihilation event emits a gamma ray whose time of detection is compared to the incoming time of positrons, giving a distribution of positron lifetimes from which the population of bulk and/or defect states can be extracted. The trapping probability of a state will depend on the charge and open volume of the defect, with larger volume and more negatively charged defects trapping positrons more strongly, like strontium and titanium vacancies. VE-PALS measurements were performed on the $n = 6$ $(\text{Sr}_{1+\delta}\text{TiO}_3)_n\text{SrO}$ films at the neutron induced positron source (NEPO-MUC) at the München research reactor MLZ-FRMII^{31,32}. The positron lifetime spectra were

measured using position implantation energies of 5 or 6 keV, giving a calculated mean implantation depth of 100 - 140 nm in SrTiO₃^{16,17}. The spectrometer was set to have a 40 ns time window and each spectrum contained 4×10⁶ counts. From a three-term free fit of the resulting spectra the dominant state is shown for each film in Figure 3.3 compared to the characteristic lifetime of possible SrTiO₃ vacancy states as calculated in reference [33] and from defect structures reported in reference [34] using the MIKA/DOPPLER package³⁵.

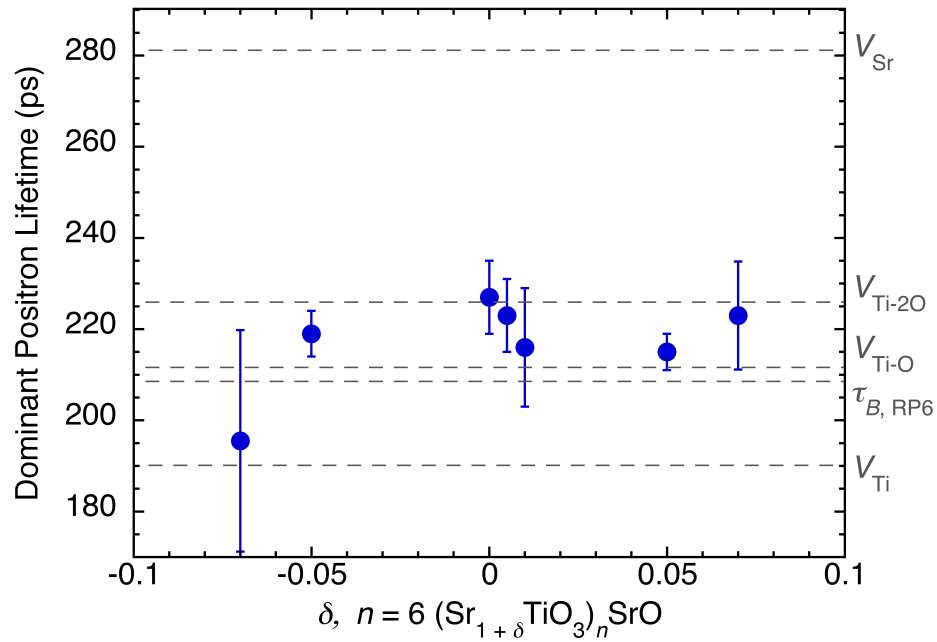


Figure 3.3 The dominant positron lifetime from a free fit of the PALS spectra of the $n = 6$ (Sr_{1+ δ} TiO₃) _{n} SrO films. Dashed lines show the characteristic lifetimes associated with possible defects in SrTiO₃ and $\tau_{B, RP6}$, the bulk lifetime for $n = 6$ (SrTiO₃) _{n} SrO.

Discussion

If the (SrO)₂ Ruddlesden-Popper faults did not accommodate off-stoichiometry

we would expect the titanium rich-films with $\delta < 0$ to have higher dominant positron lifetimes with the incorporation of the higher lifetime strontium vacancies as seen in references [16, 17]. In contrast, the dominant lifetime for the $n = 6$ $(\text{Sr}_{1+\delta}\text{TiO}_3)_n\text{SrO}$ films show little variance and are clustered between 212 – 230 ps around the TiO_x vacancy lifetimes, contributing $> 78\%$ of the total spectra intensity (see Supplementary Table 1). While non-trivial to distinguish the contribution of each V_{TiO_x} state and the bulk state of pure $(\text{SrTiO}_3)_6\text{SrO}$, $\tau_{\text{B,RP6}}$, it is clear that the V_{TiO_x} is the dominant vacancy found in $n = 6$ $(\text{Sr}_{1+\delta}\text{TiO}_3)_n\text{SrO}$. When a three-term fit of the spectra is forced to include V_{Ti} and/or V_{Sr} (see Supplementary Table 1), the free term is still found between 198 – 266 ps indicating that the dominant peak is not solely a convolution of titanium and strontium vacancies as found in our previous measurements on PLD SrTiO_3 films^{16,17}.

These results expand on the nature of the $(\text{SrTiO}_3)_n\text{SrO}$ structure's defect mitigating property and explain the exceptional performance of strained $(\text{SrTiO}_3)_n\text{SrO}$ films at high frequency where loss has been identified to be due to charged point defects²⁴⁻²⁶. In the case of TiO_2 vacancies, they are charge neutral and in essence regions of $(\text{SrO})_2$ faults, seen as $\text{SrTiO}_3 + V_{\text{TiO}_2} = \text{SrO}^{36}$. If they exist, vacancies of TiO are also likely charge neutral with the addition of two electrons from nearby oxygen vacancies³⁷.

Conclusion

The defect mitigating nature of $(\text{SrTiO}_3)_n\text{SrO}$ Ruddlesden-Popper phases was probed with PALS by introducing off-stoichiometric $\text{Sr}_{1+\delta}\text{TiO}_3$ into the superlattice, forming 300 nm thick $n = 6$ $(\text{Sr}_{1+\delta}\text{TiO}_3)_n\text{SrO}$ thin films grown by MBE on (001)

SrTiO_3 . The lack of variance with off-stoichiometry seen in the resulting PALS spectra supports the conclusion that the $(\text{SrO})_2$ faults are indeed accommodating the non-stoichiometry without introducing strontium or titanium vacancies seen in PLD $\text{Sr}_{1+\delta}\text{TiO}_3$ thin films. The TiO_x vacancies that are seen are likely charge neutral nano-regions of $(\text{SrO})_2$ faults. Further studies of the contribution of oxygen vacancies and antisite defects which cannot be fully studied with PALS are needed to provide full understanding of the defect mechanisms in $(\text{SrTiO}_3)_n\text{SrO}$.

Supplementary Information

Off-stoichiometric defect accommodation in $(\text{SrTiO}_3)_n\text{SrO}$ Ruddlesden-Popper superlattices studied with positron annihilation

Supplementary Table 1

Positron lifetime component values obtained for 5 keV spectra from $n = 6$ $(\text{Sr}_{1+\delta}\text{TiO}_3)_n\text{SrO}$ films assuming four components using PALSfit. If a fit component value is fixed this is denoted by F. Sr-poor (NMD361, NMD397), near-stoichiometric (NMD330, NMD399), Ti-poor (NMD355, NMD394, NMD392).

Sample	Date	t_1 (ps)	I_1 (%)	t_2 (ps)	I_2 (%)	t_3 (ps)	I_3 (%)	χ^2
NMD361	Sept 2016	179(9)	55(13)	249(11)	45(13)	975(151)	0.2(1)	0.849
Sr-poor		88(175)	1(3)	194(4)	78(2)	281F	21(1)	0.864
		183F	61(2)	254(3)	39(2)	1021(130)	0.21(4)	0.848
		183F	40(38)	204(25)	39(35)	281F	21(3)	0.864
NMD361	Dec 2016	83(16)	7(2)	212(3)	90(1)	400(44)	3(2)	1.044
Sr-poor		33(18)	4(1)	194(2)	75(1)	281F	21(1)	1.050
		183F	63(2)	257(5)	37(2)	747(366)	0.2(2)	1.058
		183F	63(6)	236(36)	20(3)	281F	18(9)	1.064
NMD397	Dec 2016	28(18)	7(2)	219(5)	80(6)	325(20)	14(5)	1.128
Sr-poor		22(39)	5(6)	202(2)	58(4)	281F	35(1)	1.132
		183F	44(1)	266(2)	56(1)	789(249)	0.2(1)	1.158
		183F	40(7)	237(29)	27(4)	281F	33(10)	1.144
NMD330	Sept 2016	138(28)	15(10)	227(8)	84(9)	509(171)	1(1)	0.908
Near-Stoich		117(65)	5(8)	206(9)	75(5)	281F	20(3)	0.914
		183F	50(3)	249(5)	50(3)	688(436)	0.2(3)	0.913

		183F	48(7)	235(21)	37(3)	281F	15(9)	0.916
NMD399	Dec 2016	141(30)	14(11)	223(8)	85(10)	473(89)	1(1)	0.976
Near-Stoich		91(77)	2(3)	201(5)	78(1)	281F	20(2)	0.987
		183F	50(3)	245(5)	50(3)	574(136)	0.5(4)	0.979
		183F	44(12)	222(20)	39(7)	281F	17(6)	0.988
NMD355	Sept 2016	152(24)	21(14)	230(9)	78(14)	626(129)	0.9(5)	0.862
Ti-poor		116(339)	1(12)	195(10)	73(9)	281F	25(3)	0.881
		183F	54(2)	253(3)	46(2)	913(76)	0.4(1)	0.862
		183F	22(1)	198(2)	52.7(1)	281F	26(1)	0.881
NMD355	Dec 2016	56(13)	7(1)	216(2)	91(1)	480(39)	2(1)	1.062
Ti-poor		193(2)	74(1)	281F	25(2)	905(323)	0.3(1)	1.113
		183F	54(3)	252(5)	46(2)	677(155)	642(298)	1.093
		183F	56(9)	228(38)	20(3)	281F	24(7)	1.120
NMD394	Dec 2016	101(16)	10(3)	215(4)	88(2)	453(79)	1(1)	0.964
Ti-poor		54(20)	5(1)	197(20)	79(1)	281F	17(1)	0.970
		89(49)	2(2)	183F	59(6)	252(5)	38(4)	0.993
		183F	65(4)	254(32)	30(22)	281F	4(26)	0.982
NMD392	Dec 2016	144(33)	17(19)	216(13)	82(18)	443(153)	1(2)	1.019
Ti-poor		53(47)	2(1)	194(17)	83(1)	281F	15(1)	1.022

		183F	65(3)	249(7)	34(2)	610(471)	0.2(4)	1.022
		183F	64(7)	231(25)	25(2)	281F	11(6)	1.024

References

1. Birol, T., Benedek, N. A. & Fennie, C. J. Interface Control of Emergent Ferroic Order in Ruddlesden-Popper $\text{Sr}_{n+1}\text{Ti}_n\text{O}_{3n+1}$. *Phys. Rev. Lett.* **107**, 257602 (2011).
2. Pitcher, M. J. *et al.* Tilt engineering of spontaneous polarization and magnetization above 300 K in a bulk layered perovskite. *Science* **347**, 420 (2015).
3. Oh, Y.S., Luo, X., Huang, F.-T., Wang, Y., & Cheong, S.-W. Experimental demonstration of hybrid improper ferroelectricity and the presence of abundant charged walls in $(\text{Ca,Sr})_3\text{Ti}_2\text{O}_7$ crystals. *Nat. Mater.* **14**, 407 (2015).
4. Benedek, N. A., Rondinelli, J. M., Djani, H., Ghosez, P., & Lightfoot, P. Understanding ferroelectricity in layered perovskites: new ideas and insights from theory and experiments. *Dalton Trans.* **44**, 10543 (2015).
5. Balachandran, P. V., Young, J., Lookman, T., & Rondinelli, J. M. Learning from data to design functional materials without inversion symmetry. *Nat. Commun.* **8**, 14282 (2017).
6. Lee, C.-H. *et al.* Exploiting dimensionality and defect mitigation to create tunable microwave dielectrics. *Nature* **502**, 532 (2013).
7. Meyer, T. L. *et al.* Strain control of oxygen kinetics in the Ruddlesden-Popper oxide $\text{La}_{1.85}\text{Sr}_{0.15}\text{CuO}_4$. *Nature Commun.* **9**, 92 (2018).
8. Amow, G. Davidson, I. J., & Skinner, S. J. A comparative study of the Ruddlesden-Popper series $\text{La}_{n+1}\text{Ni}_n\text{O}_{3n+1}$ ($n=1,2$ and 3), for solid-oxide fuel-cell cathode applications. *Solid State Ionics* **177**, 1205 (2006).
9. Yamada, H. & Miller, G. R. Point defects in reduced strontium titanate. *J. Solid State Chem.* **6**, 169 (1973).
10. Wiedigen, S. *et al.* Interplay of point defects, biaxial strain, and thermal conductivity in homoepitaxial SrTiO_3 thin films. *Appl. Phys. Lett.* **100**, 061904 (2012).
11. Brooks, C. M. *et al.* Tuning thermal conductivity in homoepitaxial SrTiO_3 films via defects. *Appl. Phys. Lett.* **107**, 051902 (2015).
12. Lee, D. *et al.* Emergence of room-temperature ferroelectricity at reduced dimensions. *Science* **349**, 1314 (2015).
13. Tanaka, T., Matsunaga, K., Ikuhara, Y. & Yamamoto, T. First-principles study on structures and energetics of intrinsic vacancies in SrTiO_3 . *Phys. Rev. B* **68**, 205213 (2003).

14. Freedman, D. A., Roundy, D., & Arias, T. A. Elastic effects of vacancies in strontium titanate: Short- and long-range strain fields, elastic dipole tensors, and chemical strain. *Phys. Rev. B* **80**, 064108 (2009).
15. Suzuki, T., Nishi, Y., & Fujimoto, M. Defect structure in homoepitaxial non-stoichiometric strontium titanate thin films. *Philos. Mag. A* **80**, 621 (2000).
16. Keeble, D. J., Wicklein, S., Dittmann, R., Ravelli, L., Mackie, R. A., & Egger, W. Identification of *A*- and *B*-site cation vacancy defects in perovskite oxide thin films. *Phys. Rev. Lett.* **105**, 226102 (2010).
17. Keeble, D. J., Wicklein, S., Jin, L., Jia, C. L., Egger, W., & Dittmann, R. Nonstoichiometry accommodation in SrTiO₃ thin films studied by positron annihilation and electron microscopy. *Phys. Rev. B* **87**, 195409 (2013).
18. Lee, D. *et al.* Identification of a functional point defect in SrTiO₃. *Phys. Rev. Materials* **2**, 060403 (2018).
19. Witek, S., Smyth, D.M., & Pickup, H. Variability of the Sr/Ti Ratio in SrTiO₃. *J. Am. Ceram. Soc.* **67**, 372 (1984).
20. Knott, L. J., Cockroft, N. J., & Wright, J. C. Site-selective spectroscopy of erbium-doped SrTiO₃, Sr₂TiO₄, and Sr₃Ti₂O₇. *Phys. Rev. B* **51**, 5649 (1995).
21. Balz, D. & Plieth, K. Die Struktur des Kaliumnickelfluorids, K₂NiF₄. *Z. Für Elektrochem. Berichte Bunsenges. Für Phys. Chem.* **59**, 545–551 (1955).
22. Ruddlesden, S. N. & Popper, P. New compounds of the K₂NiF₄ type. *Acta Crystallogr.* **10**, 538–539 (1957).
23. Ruddlesden, S. N. & Popper, P. The compound Sr₃Ti₂O₇ and its structure. *Acta Crystallogr.* **11**, 54–55 (1958).
24. Elissalde, C. & Ravez, J. Ferroelectric ceramics: defects and dielectric relaxations. *J. Mater. Chem.* **11**, 1957–1967 (2001).
25. Tagantsev, A. K., Sherman, V. O., Astafiev, K. F., Venkatesh, J. & Setter, N. Ferroelectric Materials for Microwave Tunable Applications. *J. Electroceramics* **11**, 5–66 (2003).
26. Vorobiev, A., Rundqvist, P., Khamchane, K., & Gevorgian, S. Microwave loss mechanisms in Ba_{0.25}Sr_{0.75}TiO₃ thin film varactors. *J. Appl. Phys.* **96**, 4642 (2004).
27. McCoy, M. A., Grimes, R. W., & Lee, W. E. Phase stability and interfacial structures in the SrO–SrTiO₃ system. *Philos. Mag. A* **75**, 833 (1997).

28. Haeni, J. H., Theis, C. D. & Schlom, D. G. RHEED Intensity Oscillations for the Stoichiometric Growth of SrTiO₃ Thin Films by Reactive Molecular Beam Epitaxy. *J. Electroceramics* **4**, 385–391 (2000).
29. Haislmaier, R.C, Stone, G., Alem, N., & Engel-Herbert, R. Creating Ruddlesden-Popper phases by hybrid molecular beam epitaxy. *Appl. Phys. Lett.* **109**, 043102 (2016).
30. Nelson, J. B. & Riley, D. P. An experimental investigation of extrapolation methods in the derivation of accurate unit-cell dimensions of crystals. *Proc. Phys. Soc.* **57**, 160 (1945).
31. Sperr, P. *et al.* Status of the pulsed low energy positron beam system (PLEPS) at the Munich Research Reactor FRM-II. *Appl. Surf. Sci.* **255**, 35 (2008).
32. Hugenschmidt, C. *et al.* Unprecedented intensity of a low-energy positron beam. *Nucl. Instrum. Methods A* **593**, 616 (2008).
33. Mackie, R. A., Singh, S., Laverock, J., Dugdale, S. B. & Keeble, D. J., Vacancy defect positron lifetimes in strontium titanate. *Phys. Rev. B* **79**, 014102 (2009).
34. Tanaka, T., Matsunaga, K., Ikuhara, Y., & Yamamoto, T. First-principles study on structures and energetics of intrinsic vacancies in SrTiO₃. *Phys. Rev. B* **68**, 205213 (2003).
35. Torsti, T. *et al.* Three real-space discretization techniques in electronic structure calculations. *Phys. Status Solidi B* **243**, 1016 (2006).
36. Balachandran, U. & Eror, N. G. On defect structure of strontium titanate with excess SrO. *J. Mater. Sci.* **17**, 2133 (1982).
37. Janotti, A., Varley, J. B., Choi, M., & Van de Walle, C. G. Vacancies and small polarons in SrTiO₃. *Phys. Rev. B* **90**, 085202 (2014).

Chapter 4

Dependence of Dielectric Constant and Leakage on Sample Quality in (Ba,Sr)TiO₃ Silicon MIM Devices

Natalie M. Dawley¹, Zhe Wang², Kiyoun Lee³, and Darrell G. Schlom^{1,4}

1. Department of Materials Science and Engineering, Cornell University, Ithaca, New York 14853, US

2. School of Applied and Engineering Physics, Cornell University, Ithaca, New York 14853, USA

3. Process Technology Group, Platform Technology Lab, Samsung Advanced Institute of Technology, Suwon-si, Gyeonggi-do, 443-803 South Korea

4. Kavli Institute at Cornell for Nanoscale Science, Ithaca, New York 14853, USA

Correspondence and requests for materials should be addressed to D.G.S. (email: schlom@cornell.edu)

Abstract

With the development of high-quality oxide integration with silicon, a wider range of dielectric materials can be revisited for superior performance in capacitor or transistor devices. Here we report the highest quality, lowest current leakage $\text{Ba}_x\text{Sr}_{1-x}\text{TiO}_3$ metal-insulator-metal (MIM) structures epitaxially integrated with silicon. $\text{Ba}_x\text{Sr}_{1-x}\text{TiO}_3$ is a common dielectric material used in capacitor circuit components whose high dielectric constant of $>15,000$ in bulk makes it an attractive replacement for on-chip MIM capacitors. Material quality and silicon integration have been the largest challenges to overcome for thin film integration. We have identified growth conditions for the highest quality films reported in literature, which focused on growth temperature and single-phase SrRuO_3 bottom electrodes. With the introduction of $(\text{SrO})_2$ layers we were able to further lower current leakage by two orders of magnitude. All films suffer from low dielectric constant and tunability, which we propose to improve with higher barium concentrations.

The epitaxial integration of perovskites with silicon-based devices like on-chip MIM capacitors has been explored for more than two decades¹. The issue of film quality has been a challenge due to interfacial reactions of oxides with silicon^{2,3} and the large thermal expansion mismatch of the two materials⁴⁻⁶ ($\alpha_{\text{Si}} = 2.49 \times 10^{-6} \text{ K}^{-1}$ versus $\alpha_{\text{SrTiO}_3, \text{SrRuO}_3} \approx 10 \times 10^{-6} \text{ K}^{-1}$) creating additional strain during cooling after film growth and introducing dislocations. With improvements in the integration of SrTiO₃ with silicon^{7,8} we have revisited this topic to understand how film quality affects dielectric constant and current leakage in full oxide Metal-Insulator-Metal (MIM) capacitors on silicon. In addition we examine how current leakage and dielectric constant are affected by the introduction of (SrO)₂ faults in the (Ba,Sr)TiO₃ layer.

Experiment

Film growth and structural characterization

To study how sample quality and strain affect dielectric properties of $x = 0.3$ Ba_xSr_{1-x}TiO₃ thin films, three 20 nm thick Ba_{0.3}Sr_{0.7}TiO₃ films with 50 nm thick SrRuO₃ bottom electrodes grown on 15 nm thick SrTiO₃ were grown with various quality on (001) Si using Molecular-Beam Epitaxy (MBE). In reference [9] we have shown previous successful integration of this Ba:Sr ratio with silicon. All layers were grown *in situ* with no exposure to air. MBE growth of SrTiO₃ on (001) silicon has been described elsewhere^{3-8,10}. The SrRuO₃ was grown at 660 – 700 °C under an oxidant of a mixture of O₂ + ~10% O₃, and the Ba_{0.3}Sr_{0.7}TiO₃ layer was grown at 650 °C and 750 °C in 7×10^{-7} Torr O₂ + ~10% O₃. Samples with three or five (SrO)₂ layers inserted into the Ba_{0.3}Sr_{0.7}TiO₃, forming $n = 10$ and 18 (Ba_{0.3}Sr_{0.7}TiO₃)_{n-1}(SrTiO₃)₁SrO Ruddlesden-Popper phases were also grown to lower current leakage and defect

density associated with Ruddlesden-popper $(\text{SrTiO}_3)_n\text{SrO}^{11}$. The x-ray diffraction of all films is shown in Figure 4.1 with rocking curve full-width-at-half-maximum (FWHM) denoted for each film (rocking curve plots are shown in Supplementary Figure 4.5).

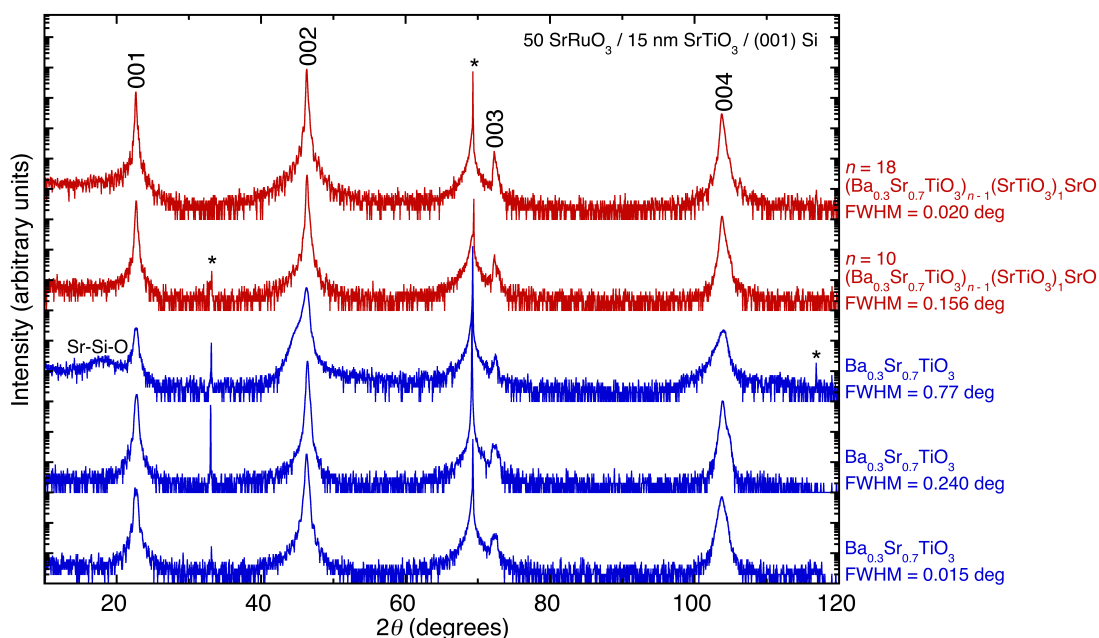


Figure 4.1 X-ray diffraction, 2θ , of a series of $x = 0.3 \text{ Ba}_x\text{Sr}_{1-x}\text{TiO}_3$ films in blue and $x = 0.3 (\text{Ba}_x\text{Sr}_{1-x}\text{TiO}_3)_{n-1}(\text{SrTiO}_3)\text{SrO}$ films in red, grown on $50 \text{ nm SrRuO}_3 / 20 \text{ nm SrTiO}_3 / (001) \text{ Si}$ with the listed FWHM of the ω rocking curve scan of the 002 film peak. The 001 silicon substrate peaks are denoted with a (*).

Scanning transmission electron microscopy (STEM) is shown in Figure 4.2, revealing the origin of the spread in film quality measured by the ω rocking curves. All films show SiO_2 at the interface of the SrTiO_3 and Si due to prolonged sample exposure at high temperatures and oxygen pressures required to grow multiple layers. The quality of the conductive SrRuO_3 was linked with higher quality samples. SrRuO_3 can form secondary phases of RuO_2 or Sr_2RuO_4 when the growth conditions are not

within a narrow range of temperature and Sr:Ru ratio¹². Shown in Figure 4.2a-d, the highest quality sample (Figure 4.2a) shows minimal impurity phases while the lowest quality sample (Figure 4.2c and d) has significant formation of Sr₂RuO₄. The sample with a rocking curve FWHM of 0.24° (Figure 4.2b) shows a portion of RuO₂ secondary phase. The $n = 10$ and 18 (Ba_{0.3}Sr_{0.7}TiO₃) _{$n-1$} (SrTiO₃)₁SrO STEM is shown in Figure 4.2e-h, where the (SrO)₂ layers can clearly be identified.

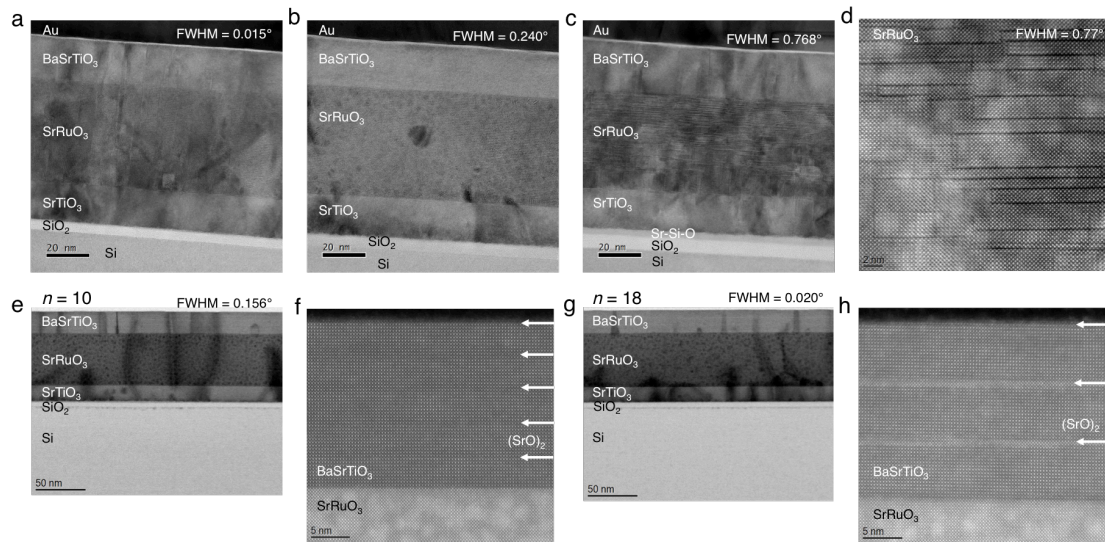


Figure 4.2 Annular dark field STEM (**a-d**, **g**, and **h**) of $x = 0.3$ Ba _{x} Sr_{1- x} TiO₃ samples shown in **Figure 4.1**. **a**, The highest quality sample shows phase-pure layers. **b**, A relatively phase-pure SrRuO₃ with possible RuO₂ formation seen as a spherical secondary phase leading to lower film quality. **c**, The lowest quality sample due to the large incorporation of secondary phase Sr _{$n+1$} Ru _{n} O_{3 $n+1$} seen in panel **d**. **e-h**, The $x = 0.3$ (Ba _{x} Sr_{1- x} TiO₃) _{$n-1$} (SrTiO₃)₁SrO MIM devices with bright field STEM, **e** and **g**, of the $n = 10$ and 18 stack respectively. **f**, The five (SrO)₂ layers inserted into the $x = 0.3$ Ba _{x} Sr_{1- x} TiO₃ and panel **h** showing the three (SrO)₂ layers inserted can clearly be identified.

Dependence of dielectric constant and leakage on sample quality

The dielectric constant and leakage properties were measured to examine their

dependence on film quality. To measure on-chip MIM devices, gold electrodes were patterned on the sample with 100 μm diameter for current leakage measurements and 20 μm diameter electrodes for dielectric measurements. The out-of-plane dielectric constant, K_{33} , was measured with an LCR meter and cryoprobe setup and the resulting data is shown in Figure 4.3a-c. The dielectric constant slightly increases for lower quality samples (higher rocking curve FWHM of the 002 $\text{Ba}_x\text{Sr}_{1-x}\text{TiO}_3$ film peak) due to disorder-induced polarization associated with dislocations and mosaicity. The dielectric constant is far lower than bulk $\text{Ba}_x\text{Sr}_{1-x}\text{TiO}_3$, which is known to be a pervasive issue in $\text{Ba}_x\text{Sr}_{1-x}\text{TiO}_3$ thin films^{13,14}. To identify if the samples show a strong ferroelectric transition, the out-of-plane dielectric constant was measured (Figure 4.3b and c) as a function of temperature, where an increase in dielectric constant is expected at the ferroelectric phase transition. All samples show low dielectric constant across all temperatures measured indicating the samples are have little to no ferroelectric polarization and thus dielectric tunability with an applied voltage. No tunability is desired for an on-chip MIM capacitor but for other devices like tunable capacitors the samples in their current form are not candidates.

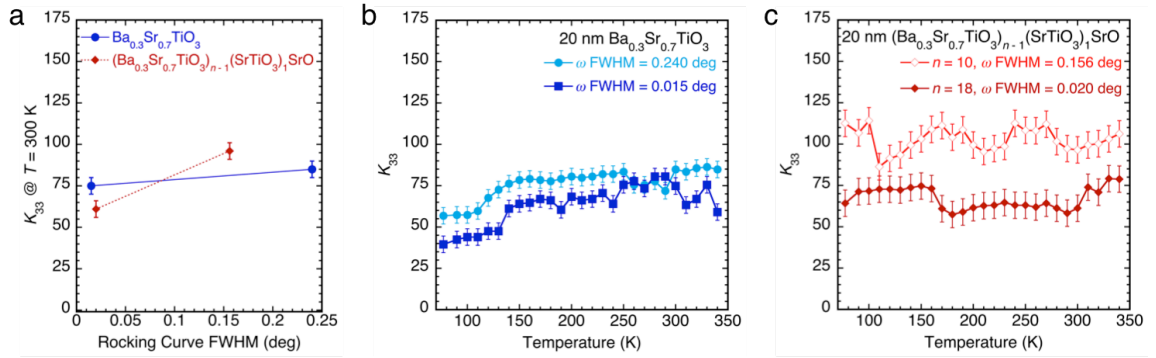


Figure 4.3 **a**, The out-of-plane dielectric constant K_{33} is seen to increase with lower sample quality (higher FWHM). The lowest quality film with a FWHM of 0.77° had high leakage that prevented the measurement of a reliable K_{33} . Out-of-plane dielectric constant K_{33} measured as a function of temperature for, **b**, $\text{Ba}_x\text{Sr}_{1-x}\text{TiO}_3$ MIM devices and **c**, $(\text{Ba}_x\text{Sr}_{1-x}\text{TiO}_3)_{n-1}(\text{SrTiO}_3)_1\text{SrO}$ structures. Both films show little change with temperature indicating the samples are likely not ferroelectric and have low dielectric tunability with an applied voltage.

Current leakage through the MIM device was measured (Figure 4.4 and Supplementary Figure 4.6) and found to strongly correlate with sample quality as dislocations threading through the stack provide conduction pathways¹³. The addition of $(\text{SrO})_2$ layers in $(\text{Ba}_x\text{Sr}_{1-x}\text{TiO}_3)_{n-1}(\text{SrTiO}_3)_1\text{SrO}$ decreased the leakage by two orders of magnitude due to the known defect-accommodating nature of the material¹¹. The highest quality films (lowest ω rocking curve FWHM) have the lowest leakage of all epitaxial $\text{Ba}_x\text{Sr}_{1-x}\text{TiO}_3$ on silicon devices reported in literature, the previous record being 10^{-8} A/cm^2 at 2 V (148 kV/cm)¹⁵.

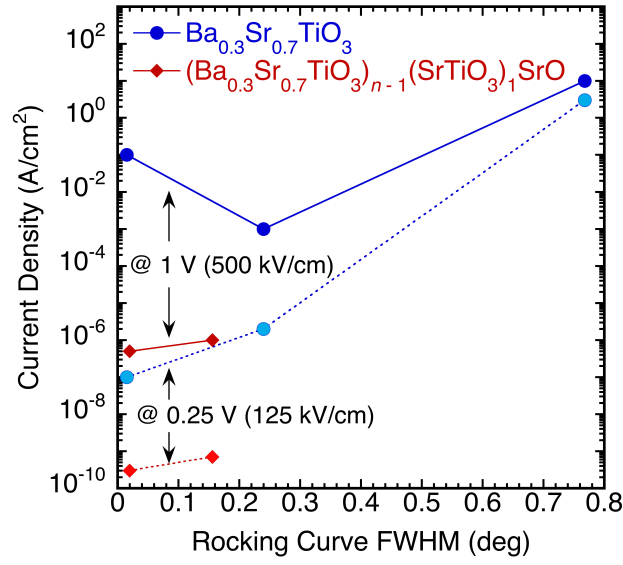


Figure 4.4 Current leakage in MIM devices for two different electric fields. Samples with (SrO)₂ layers inserted into the Ba_xSr_{1-x}TiO₃ shown in red diamonds have dramatically lower leakage.

Discussion

While our films show excellent quality and the lowest reported leakage in literature the dielectric constant is well below what is seen in bulk and the films are not ferroelectric. The degradation of film quality from the introduction of secondary phases at interfaces or dislocations from the large thermal expansion coefficient mismatch is expected to have strong effects on the MIM device properties. Dislocations create strain fields and vacancies which modify the local dielectric constant and increase loss by providing conduction channels for charges¹³. The charged defects introduced by dislocations and strain fields can suppress the local dielectric permittivity¹⁶. Film thickness also greatly reduces the dielectric constant by intrinsic depolarization effects¹⁴. To achieve higher dielectric constant, tunable on-chip MIM devices we propose future work to increase the amount of ferroelectric

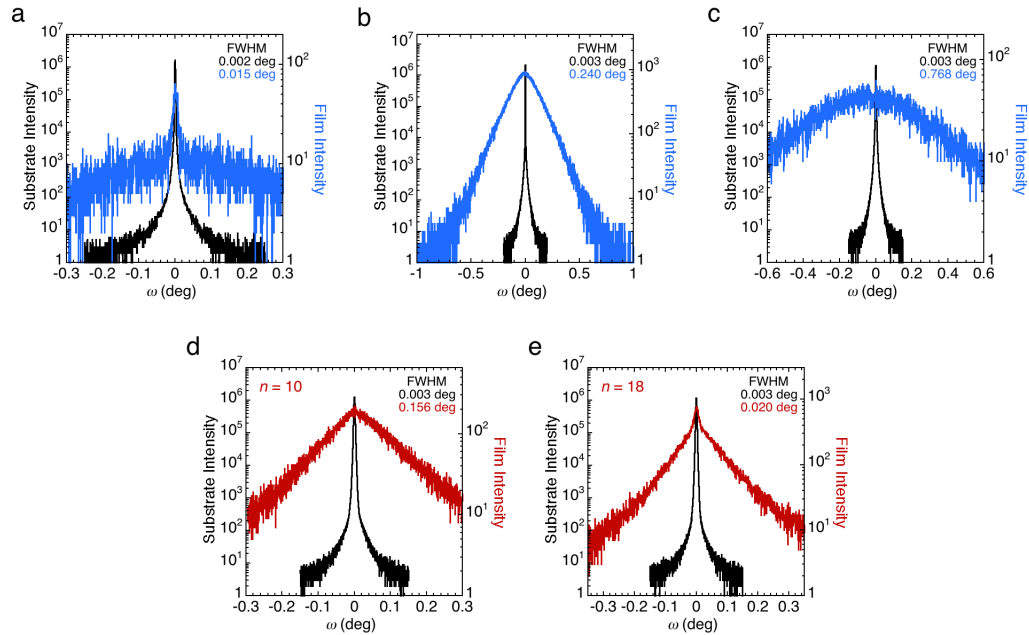
BaTiO₃ in the (Ba,Sr)TiO₃ dielectric film to induce a larger polarization at these low dimensions. BaTiO₃ is known to be ferroelectric down to film thicknesses of 5 nm with out-of-plane dielectric constants of ~500 when grown on SrRuO₃ / (001) SrTiO₃¹⁷.

Conclusion

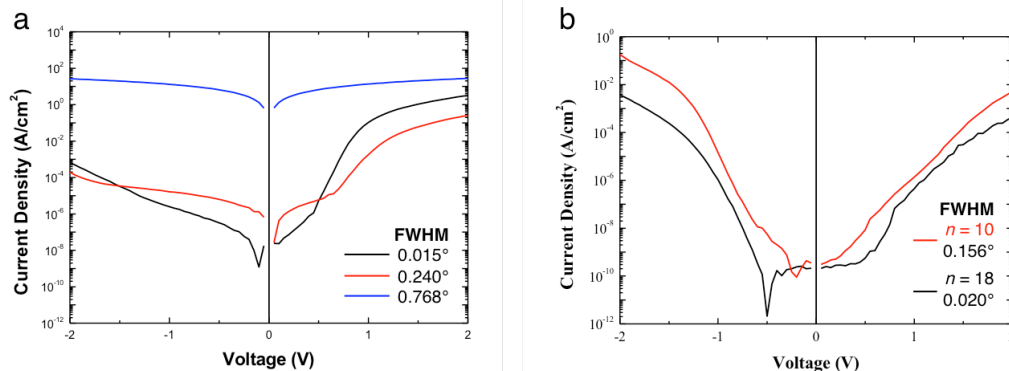
In conclusion, the dielectric constant and current leakage was measured for a range of 20 nm $x=0.3$ Ba_xSr_{1-x}TiO₃ and (Ba_xSr_{1-x}TiO₃)_{n-1}(SrTiO₃)SrO / 50 nm SrRuO₃ / 20 nm SrTiO₃ / (001) Si MIM devices. All films showed low dielectric constant, K_{33} , characteristic of thin films. With the highest quality film, as measured by the rocking curve FWHM, we achieved the lowest current leakage in epitaxial MIM silicon devices reported in literature. With the introduction of defect-mitigating (SrO)₂ layers, current leakage was further decreased by two orders of magnitude. In future work we propose to increase the ferroelectric BaTiO₃ composition of the Ba_xSr_{1-x}TiO₃ film to achieve higher dielectric constants.

Supplementary Information

Dependence of Dielectric Constant and Leakage on Sample Quality in (Ba,Sr)TiO₃, Silicon MIM Devices



Supplementary Figure 4.5 ω rocking curves of the 002 silicon and 002 film peak for: **a – c** films of 20 nm $x = 0.3$ Ba_xSr_{1-x}TiO₃ / 50 nm SrRuO₃ / 15 nm SrTiO₃ / (001) Si, and **d & e** films of 20 nm $x = 0.3$ (Ba_xSr_{1-x}TiO₃)_{n-1}(SrTiO₃)₁SrO / 50 nm SrRuO₃ / 15 nm SrTiO₃ / (001) Si.



Supplementary Figure 4.6 Current Leakage in MIM devices with applied voltage. **a**, $x = 0.3$ Ba_xSr_{1-x}TiO₃ / 50 nm SrRuO₃ / 15 nm SrTiO₃ / (001) Si structures with varying quality measured by ω rocking curve FWHM. **b**, Samples with (SrO)₂ layers inserted into the Ba_xSr_{1-x}TiO₃ show dramatically lower leakage.

References

1. Hou, S. Y., Kwo, J., Watts, R. K., Cheng, J.-Y. & Fork, D. K. Structure and properties of epitaxial $\text{Ba}_{0.5}\text{Sr}_{0.5}\text{TiO}_3/\text{SrRuO}_3/\text{ZrO}_2$ heterostructure on Si grown by off-axis sputtering. *Appl. Phys. Lett.* **67**, 1387 (1995).
2. Hubbard K. J. & Schlom, D. G. Thermodynamic Stability of Binary Oxides in Contact with Silicon. *J. Mater. Res.* **11** (1996) 2757-2776.
3. Lettieri, J., Haeni, J. H. & Schlom, D. G. Critical issues in the heteroepitaxial growth of alkaline-earth oxides on silicon. *J. Vac. Sci. Technol.* **A20**, 1332 (2002).
4. Touloukian, Y. S., Kirby, R., Taylor, E., & Lee, T. *Thermophysical Properties of Matter-the TPRC Data Series*. Volume 13. Thermal Expansion-Nonmetallic Solids. (1977)
5. de Ligny, D., & Richet, P. High-temperature heat capacity and thermal expansion of SrTiO_3 and SrZrO_3 . *Phys. Rev. B* **53**, 3013 (1996).
6. Yamanaka, S., Maekawa, T., Muta, H., Matsuda, Kobayashi, S., & Kurosaki, K. Thermophysical properties of SrHfO_3 and SrRuO_3 . *J. Solid State Chem.* **177**, 3484 (2004).
7. Li, H. *et al.* Two-dimensional growth of high-quality strontium titanate thin films on Si. *J. Appl. Phys.* **93**, 4521 (2003).
8. Warusawithana, M. P. *et al.* A Ferroelectric Oxide Made Directly on Silicon. *Science* **324**, 367–370 (2009).
9. Vaithyanathan, V. *et al.* *c*-Axis Oriented Epitaxial BaTiO_3 Films on (001) Si. *J. Appl. Phys.* **100** 024108 (2006).
10. Wang, Z. *et al.*, Enhancement of crystalline quality of SrTiO_3 on silicon. *APL Mater.* (submitted).
11. Lee, C. H. *et al.* Exploiting Dimensionality and Defect Mitigation to Create Tunable Microwave Dielectrics. *Nature* **502** 532–536 (2013).
12. Nair, H. P. *et al.* Synthesis Science of SrRuO_3 and CaRuO_3 Epitaxial Films with High Residual Resistivity Ratios. *APL Mater.* **6**, 046101 (2018).
13. Streiffer, S. K., Basceri, C., Parker, C. B., Lash, S. E., & Kingon, A. I. Ferroelectricity in thin Films: The Dielectric Response of Fiber-Textured $(\text{Ba}_x\text{Sr}_{1-x})\text{Ti}_{1+y}\text{O}_{3+z}$ Thin Films Grown by Chemical Vapor Deposition. *J. Appl. Phys.* **86**, 4565–4575 (1999).

14. Stengel, M. & Spaldin, N. A. Origin of the dielectric dead layer in nanoscale capacitors. *Nature*, **443**, 679-682 (2006).
15. Lee, M.-B., Kawasaki, M., Yoshimoto, M., Moon, B.-K., Ishiwara, H., & Koinuma, H. Epitaxial Growth of $\text{Ba}_{1-x}\text{SrTiO}_3$ Films on Si by Pulsed Laser Deposition and Their Dielectric Properties. *Mat. Res. Soc. Symp. Proc.* **361**, 521-526 (1995).
16. Tagantsev, A. K., Sherman, V. O., Astafiev, K. F., Venkatesh, J. & Setter, N. Ferroelectric Materials for Microwave Tunable Applications. *J. Electroceramics* **11**, 5–66 (2003).
17. Zubko, P., Lu, H., Bark, C.-W., Marti, X., Santiso, J., Eom, C.-B., Catalan, G., & Gruverman, A. On the persistence of polar domains in ultrathin ferroelectric capacitors. *J. Phys.: Condens. Matter* **29**, 284001 (2017).

Chapter 5

Thermal conductivity of the $n = 1 - 5$ and 10 members of the $(\text{SrTiO}_3)_n\text{SrO}$ Ruddlesden-Popper superlattices

Natalie M. Dawley¹, Ella K. Pek⁵, Che-Hui Lee,^{1,2} Ye Zhu,³ Qingyun Mao,³ Julia A. Mundy,³ David A. Muller,³ Xiaoxing Xi,⁴ David G. Cahill,⁵ and Darrell G. Schlom^{1,6}

1. Department of Materials Science and Engineering, Cornell University, Ithaca, New York 14853, USA
 2. Department of Materials Science and Engineering, Pennsylvania State University, University Park, Pennsylvania 16802, USA
 3. School of Applied and Engineering Physics, Cornell University, Ithaca, New York 14853, USA
 4. Department of Physics, Temple University, Philadelphia, Pennsylvania 19122, USA
 5. Kavli Institute at Cornell for Nanoscale Science, Ithaca, New York 14853, USA
- Electronic mail: Schlom@cornell.edu

Abstract

Unlike many superlattice structures, the Ruddlesden-Popper phases have atomically abrupt interfaces providing a clear interpretation of thermal transport results. Here we report the thermal transport in thin films of $n = 1 - 5$ and 10 $(\text{SrTiO}_3)_n\text{SrO}$ Ruddlesden-Popper superlattices grown by molecular-beam epitaxy. The longitudinal thermal conductivity (k_{33}) is measured by time-domain thermoreflectance at room temperature and compared to atomic-level simulations. The longitudinal thermal conductivity of this homologous series exhibits saturation below $n = 3$ ($\sim 2.0 \text{ W m}^{-1} \text{ K}^{-1}$). Characterization by x-ray diffraction and cross-sectional transmission electron microscopy confirm that these samples have a layered Ruddlesden-Popper superlattice structure.

Materials with low thermal conductivity are of interest for a variety of potential applications including thermal barrier coatings^{1,2} and thermoelectric devices³⁻⁵. Reducing the dimensionality of the material has been considered a promising approach to increase the effectiveness of a thermoelectric material. As the dimensionality of a material is decreased, the length scale becomes a new variable to control material properties through quantum-confinement effects. Recently, a greatly improved figure-of-merit for thermoelectric cooling and power conversion have been demonstrated in quantum well systems^{6,7}. Superlattices – materials with a high density of epitaxial internal interfaces – should have significantly degraded thermal transport behavior, which improves their performance as thermal barriers and as materials used in thermoelectric devices^{8,9}.

Several factors reduce thermal conductivity in superlattice structures. In general, internal interfaces inhibit the flow of heat. Differences in elastic properties impede the transfer of vibrational energy across interfaces between dissimilar materials¹⁰. Theoretical calculations reveal that the average phonon velocity decreases with increasing superlattice period due to the increase amount of phonon band folding¹¹. Additionally, in a superlattice the energy required for Umklapp process, an anharmonic scattering process, is reduced relative to the bulk because of a smaller reciprocal-lattice vector¹². Experimentally, the thermal properties of synthetic semiconductor superlattices GaAs–AlAs have been studied for their unique thermal conductivity^{13,14} and phonon transport¹⁵. In particular, the transverse thermal conductivity (k_{13}) decreases with reducing superlattice period¹³ and an even stronger reduction is found in the thermal conductivity of the superlattice along the direction in

which it is layered, i.e., perpendicular to the (001)-oriented substrate surface (k_{33})¹⁴. We refer to k_{33} as the longitudinal thermal conductivity¹⁶. As an analog system to the semiconductor superlattices, oxide superlattices also show potential for thermoelectric applications¹⁷.

It has been almost 40 years since the first calculation predicted that superlattices should have a significantly reduced thermal conductivity compared to their bulk counterpart¹⁸. With advances in thin film deposition and characterization technologies, it is now possible not only to synthesize but also to examine customized hetero-structures with sub-nanometer precision. In this work, we report an experimental study on the thermal properties of a broad spectrum ($n = 1 - 5$ and 10) of $(\text{SrTiO}_3)_n\text{SrO}$ epitaxial films measured by the time-domain thermoreflectance (TDTR) technique³. The longitudinal thermal conductivity of this homologous series, as a function of n , shows saturation below $n = 3$ and is compared to a previous computational study¹⁹.

$(\text{SrTiO}_3)_n\text{SrO}$ Ruddlesden-Popper phases have drawn extensive attention due to their potential applications as tunable dielectrics²⁰ and thermoelectric materials²¹. Recently, an ultralow longitudinal thermal conductivity ($\sim 0.4 \text{ W m}^{-1} \text{ K}^{-1}$) has been observed in $\text{CsBiNb}_2\text{O}_7$,²² the $n = 2$ member of the structurally-related Dion-Jacobson homologous series, $A[A'_{n-1}B_nO_{3n+1}]$. This layered structure has NbO_6 octahedra interleaved between alternating BiO and Cs layers. $(\text{SrTiO}_3)_n\text{SrO}$ RP phases have similar structural features; these natural superlattices are composed of an alternate stacking of double layers of rock-salt SrO and n layers of perovskite SrTiO_3 along the c -axis. With decreasing n , the repeat distance between inserted additional SrO layers

decreases and the structure undergoes a transition from a two-dimensional interfacial system to a three-dimensional monolithic single crystal. The investigation of this homologous series provides an opportunity to tailor the thermal properties through changing dimensionality.

The synthesis of single-crystal Ruddlesden-Popper phases is a challenging task. Conventional solid-state reactions can only yield polycrystalline $n = 1 - 3$ members due to the thermodynamic degeneracy of the higher- n phases^{23,24}. Severe intergrowth of mixed- n phases is generally found in attempts to make higher n members. Here we use the precise layering ability of oxide molecular-beam epitaxy (MBE) to grow not only the first five but also $n = 10$ $(\text{SrTiO}_3)_n\text{SrO}$ single-phase epitaxial 300 nm thick films. Oxide MBE can supply incident species in any desired sequence with submonolayer composition control, and essentially arbitrary n values can be synthesized even though nearby phases have similar formation energies²³⁻²⁸.

Experiment

We used a Veeco GEN10 oxide MBE system to grow the $(\text{SrTiO}_3)_n\text{SrO}$ ($n = 1 - 5, 10$) films. Molecular beams of strontium and titanium were generated using a low-temperature effusion cell and a Ti-BallTM,²⁹ respectively. The fluxes of both elements were pre-calibrated using a quartz crystal microbalance. A more accurate flux calibration was done by following the reflection high-energy electron diffraction (RHEED) intensity oscillations³⁰. Judging from the change of maximum/minimum intensity and the shape of oscillations, the shutter time needed for an absolute monolayer dose of each element is precisely determined. To grow $(\text{SrTiO}_3)_n\text{SrO}$ phases, both the stoichiometry and each monolayer absolute dose cannot be off by

more than 1%. Each of the members in this series has different sequences of SrO and TiO₂ layers. We controlled the shutter ordering of strontium and titanium ions to match the layering sequence of the desired (001)-oriented Sr_{n+1}Ti_nO_{3n+1} phases.

The majority of films were deposited ~300 nm thick onto (001) SrTiO₃ ($a = 3.905 \text{ \AA}$) substrates in an oxidant background pressure (O₂ + ~10% O₃) of 7×10^{-7} Torr at 850 °C. The lattice mismatch of the (SrTiO₃)_nSrO ($n=1-5, 10$) series to (001) SrTiO₃ decreases monotonically with increasing n , about 0.56% for $n = 1$ and about 0.03% for $n = 10$. Two $n = 1$ samples ($a = 3.883 \text{ \AA}$) were grown 200 nm thick on (001) (LaAlO₃)_{0.29}(SrAl_{0.5}Ta_{0.5}O₃)_{0.71} (LSAT) ($a = 3.869 \text{ \AA}$) for better lattice match (-0.36% vs. 0.57% on (001) SrTiO₃)³¹, as well as a 300 nm $n = 1$ sample on (001) SrTiO₃ which is above the film's critical thickness and partially relaxed.

The structural perfection of the entire (SrTiO₃)_nSrO homologous series was examined by x-ray diffraction (XRD). Figure 5.1 shows θ - 2θ scans of 300 nm thick $n = 1 - 5, 10$ films on (001) SrTiO₃ and the 200 nm $n = 1$ film on (001) LSAT. Each sample shows all peaks corresponding to phase-pure (SrTiO₃)_nSrO ($n = 1 - 5, 10$). X-ray rocking curves confirmed the high structural perfection of the films; the full width at half maximum (FWHM) of the $n = 1 - 5, 10$ films is less than 52 arc sec ($<0.014^\circ$), comparable to the rocking curve FWHM of the 004 peak of the SrTiO₃ substrates (not shown). The c -axis lattice constants of each member of the series, determined by Nelson-Riley analysis³², is $12.63 \pm 0.03 \text{ \AA}$, $12.40 \pm 0.03 \text{ \AA}$, $20.29 \pm 0.01 \text{ \AA}$, $28.16 \pm 0.02 \text{ \AA}$, $35.84 \pm 0.03 \text{ \AA}$, $43.68 \pm 0.02 \text{ \AA}$, and $82.90 \pm 0.02 \text{ \AA}$ for the $n=1$ (LSAT), 1 (SrTiO₃) 2, 3, 4, 5, and 10 phases, respectively, similar to prior RP films grown on (001) SrTiO₃.²⁵

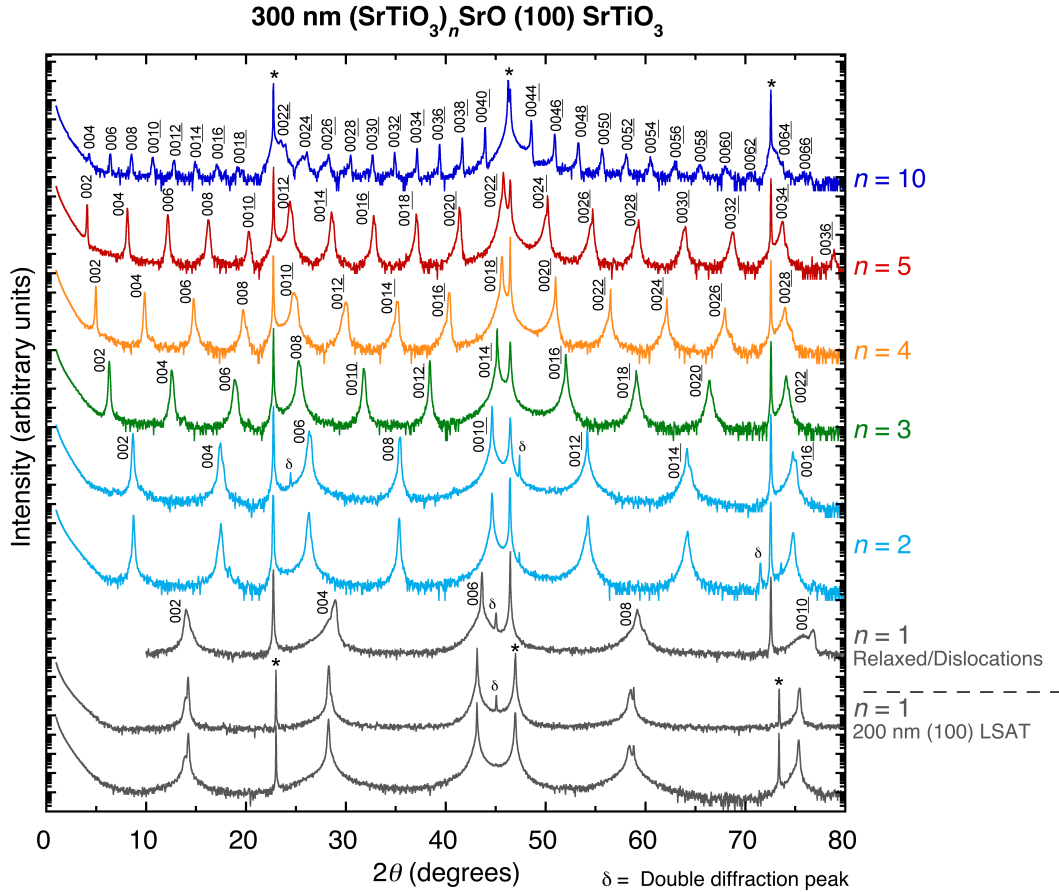


Figure 5.1 θ - 2θ x-ray diffraction scans of the epitaxial 300 nm thick $\text{Sr}_{n+1}\text{Ti}_n\text{O}_{3n+1}$ ($n=1-5, 10$) films grown on (001) SrTiO_3 (001) LSAT. Substrates peaks are labeled with a (*), and the plots are offset for clarity.

In addition to XRD, the microstructure of $(\text{SrTiO}_3)_n\text{SrO}$ films was investigated by scanning transmission electron microscopy (STEM) in a 200 kV FEI Tecnai F20 SuperTWIN STEM. TEM characterization is necessary to confirm the periodicity of superlattices with large unit cells such as the $(\text{SrTiO}_3)_n\text{SrO}$ phases³³. It is difficult to discern by XRD alone intergrowths of multiple shorter-period members from large-period superlattices. Figure 5.2 shows annular-dark-field STEM images of $n = 2, 5,$ and 10 samples taken along the [100] zone axis of the LSAT substrate. Although the

growth-direction (up in the images) ordering is clearly visible in the images, we note the existence of a few stacking faults and intergrowth regions, especially in the $n = 10$ sample. The small fraction of intergrowths in these samples is not resolved in the θ - 2θ scans and most likely stems from slight monolayer-to-monolayer dosage variations during growth.

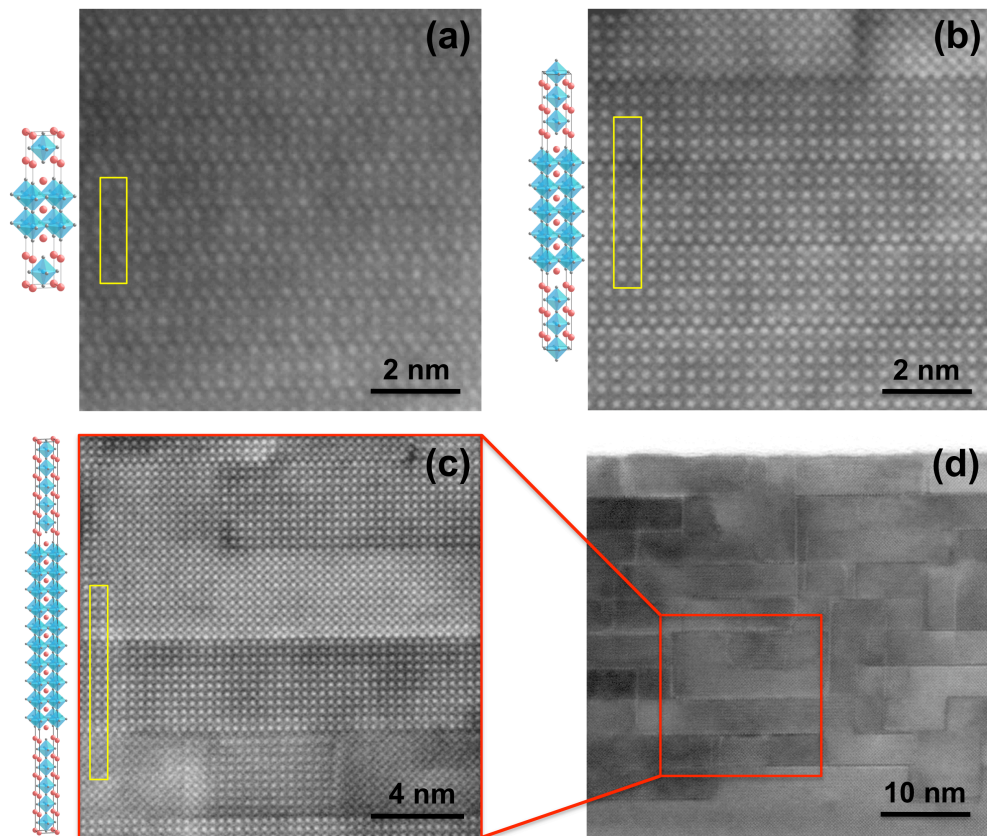


Figure 5.2 Annular-dark-field STEM images of the epitaxial Ruddlesden-Popper: (a) $n=2$ ($\text{Sr}_3\text{Ti}_2\text{O}_7$), (b) $n=5$ ($\text{Sr}_6\text{Ti}_5\text{O}_{16}$), (c) $n=10$ ($\text{Sr}_{11}\text{Ti}_{10}\text{O}_{31}$) films taken along the $[100]$ zone axis of the (001) LSAT substrate. In these images, strontium columns show higher intensity than titanium. Crystal structure models of each Ruddlesden-Popper phase are adjacent to the corresponding images. The yellow rectangles highlight the unit cell region in the images. (d) Bright-field STEM image showing a large field of view of the $n = 10$ ($\text{Sr}_{11}\text{Ti}_{10}\text{O}_{31}$) film.

The longitudinal thermal conductivity of the entire series of $(\text{SrTiO}_3)_n\text{SrO}$ ($n = 1 - 5$ and 10) films was measured by TDTR^{34,35}. It is a non-contact, pump-probe optical technique that can be used for measuring thermal properties of materials on nanometer length scales. In our implementation of TDTR, a thin aluminum layer is deposited on the surface of the thin film and pumped with short pulse of a 9.8 MHz laser beam. A small fraction of energy from each pulse in the pump beam produces a sudden temperature jump ~ 3 K near the surface of a sample. Decay of this near-surface temperature is then examined by reflected energy of the pulses in the probe beam, i.e. the temperature change of a sample is measured by its temperature-dependent reflectance. The results of these time-resolved measurements are analyzed to return longitudinal thermal conductivities. Analysis of data requires the heat capacities per unit volume of the film layers and the substrate. In cases where no published data for the heat capacity of layers was available, we used the heat capacity of chemically and structurally similar phases to analyze the data. The longitudinal thermal conductivity of the substrate was either taken from the literature, or was measured on blank single crystal substrates of the same type. The sensitivity of the TDTR data to the heat capacity of many superlattice layers is much smaller than the sensitivity to the longitudinal thermal conductivity and any systematic errors.

TDTR Results

Figure 5.3 compares the thermal conductivities of the $(\text{SrTiO}_3)_n\text{SrO}$ phases acquired from TDTR measurements at room temperature to the conductivities obtained from a previous computational study¹⁹. The experimental and computational data reveal significant agreement in trends, and magnitude of the longitudinal thermal

conductivity across the series. All samples show an expected trend as the conductivity decreases with the increasing density of thermal-resistant interfaces. Phonons experience scattering at the interfaces between rock-salt SrO and perovskite SrTiO₃ layers. A saturation in scattering occurs for $n < 3$. This saturation can be attributed to all heat carrying phonons being scattered by interfaces with an interface density < 0.7 interfaces per nm (spaced < 1.4 nm apart). This is consistent with reported phonon mean free path in bulk SrTiO₃ measured experimentally to be ~ 2 - 1.3 nm depending if the sample was a single crystal or polycrystalline³⁶. In strontium rich SrTiO₃ thin films where (SrO)₂ layers become randomly incorporated into the SrTiO₃ film the longitudinal thermal conductivity was also suppressed down to $2 \text{ W m}^{-1} \text{ K}^{-1}$ with no saturation observed³⁷.

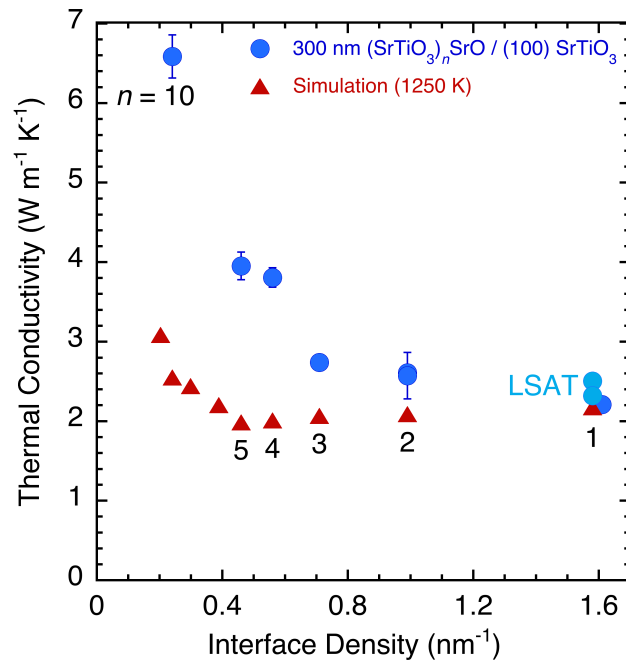


Figure 5.3 Summary of experimental and simulated longitudinal thermal conductivities of the Ruddlesden-Popper (SrTiO₃)_nSrO phases as a function of

interface density. The error bars of the experimental data taken at room temperature are the result of multiple measurements from various regions of the samples. The simulation data¹⁹ are adopted from a previous theoretical calculation at $T = 1250$ K.

A similar trend with interface density was also observed in SrTiO₃-BaTiO₃ superlattice materials with longitudinal thermal conductivity lowering to $2 \text{ Wm}^{-1}\text{K}^{-1}$ for an interface density of 0.6 nm^{-1} .³⁸ Compared to the perovskite-on-perovskite system, the Ruddlesden-Popper superlattices have not only an atomic-mass variation, but also a structural variation between superlattice layers from the layers of perovskite slabs interleaved with rocksalt-type SrO layers. Structural changes from layer-to-layer are believed to provide additional contributions to phonon scattering at the internal interfaces.

Conclusion

In this letter we summarized the experimental and theoretical longitudinal thermal conductivity of (SrTiO₃)_nSrO phases, as a function of interface density. A saturation in conductivity is seen as the distance between interfaces becomes smaller than the phonon mean free path. Intergrowth and planar faults in RP phases might serve as additional scattering centers and lower the effective phonon mean free path. The investigation of this RP series provides an opportunity to tailor the thermal properties through changing dimensionality.

Acknowledgements

The work at Cornell was supported by the U.S. Department of Energy, Office of Basic Sciences, Division of Materials Sciences and Engineering, under Award No. DE-SC0002334. Sample preparation was in part facilitated by the Cornell NanoScale

Science & Technology Facility (CNF), a member of the National Nanotechnology Coordinated Infrastructure (NNCI), which is supported by the National Science Foundation (Grant NNCI-1542081).

References

1. Padture, N. P., Gell, M., and Jordan, E. H. Thermal Barrier Coatings for Gas-Turbine Engine Applications. *Science* **296**, 280 (2002).
2. Miller, R. A. Current status of thermal barrier coatings – An overview. *Surf. Coat. Technol.* **30**, 1 (1987).
3. Koh, Y. K. *et al.* Comparison of the 3ω method and time-domain thermoreflectance for measurements of the cross-plane thermal conductivity of epitaxial semiconductors. *J. Appl. Phys.* **105**, 054303 (2009).
4. Dresselhaus, M.-S. *et al.* New Directions for Low-Dimensional Thermoelectric Materials. *Adv. Mater.* **19**, 1043 (2007).
5. Snyder, G. J. & Toberer, E. S. Complex Thermoelectric Materials. *Nat. Mater.* **7**, 105 (2008).
6. Harman, T. C., Taylor, P. J., Walsh, M. P., & LaForge, B. E. Quantum Dot Superlattice Thermoelectric Materials and Devices. *Science* **297**, 2229 (2002).
7. Harman, T. C., Walsh, M. P., LaForge, B. E., & Turner, G. W. Nanostructured thermoelectric materials. *J. Electron. Mater.* **34**, L19 (2005).
8. Venkatasubramanian, R. Lattice thermal conductivity reduction and phonon localizationlike behavior in superlattice structures. *Phys. Rev. B* **61**, 3091 (2000).
9. Venkatasubramanian, R., Siivola, E., Colpitts, T., & O'Quinn, B. Thin-Film Thermoelectric Devices with High Room-Temperature Figures of Merit. *Nature* **413**, 597 (2001).
10. Chen, G. Thermal conductivity and ballistic-phonon transport in the cross-plane direction of superlattices. *Phys. Rev. B* **57**, 14958 (1998).
11. Simkin, M. V. & Mahan, G. D. Minimum Thermal Conductivity of Superlattices. *Phys. Rev. Lett.* **84**, 927 (2000).
12. Capinski, W. S., Maris, H. J., Ruf, T., Cardona, M., Ploog, K., & Katzer, D. S. Thermal-conductivity measurements of GaAs/AlAs superlattices using a picosecond optical pump-and-probe technique. *Phys. Rev. B* **59**, 8105 (1999).
13. Yao, T., Thermal Properties of AlAs/GaAs Superlattices. *Appl. Phys. Lett.* **51**, 1798 (1987).

14. Capinski, W. S. & Maris, H. J. Thermal conductivity of GaAs/AlAs superlattices *Physica B* **219**, 699 (1996).
15. Colvard, C. *et al.* Folded acoustic and quantized optic phonons in (GaAl)As superlattices. *Phys. Rev. B* **31**, 2080 (1985).
16. Note that the specific coefficient of the thermal conductivity tensor being measured is k_{33} , corresponding to the coefficient describing the heat flow parallel to the direction of the applied temperature gradient (both are along the direction perpendicular to the substrate surface). This nomenclature is analogous to the definition of “longitudinal stress,” “longitudinal strain,” “longitudinal piezoelectric effect,” and analogous tensor quantities. See for example, J.F. Nye, *Physical Properties of Crystals: Their Representation by Tensors and Matrices* (Oxford University Press, 1957, 1985) pp. 127, 144.
17. Ohta, H. *et al.* Giant thermoelectric Seebeck coefficient of a two-dimensional electron gas in SrTiO₃. *Nat. Mater.* **6**, 129 (2007).
18. Ren, Y. & Dow, J. D. Thermal conductivity of superlattices. *Phys. Rev. B* **25**, 3750 (1982).
19. Chernatynskiy, A., Grimes, R. W., Zurbuchen, M. A., Clarke, D. R., & Phillpot, S. R. Crossover in thermal transport properties of natural, perovskite-structured superlattices. *Appl. Phys. Lett.* **95**, 161906 (2009).
20. Lee, C.-H. *et al.* Exploiting dimensionality and defect mitigation to create tunable microwave dielectrics. *Nature* **502**, 532 (2013).
21. Wang, Y., Lee, K. H., Ohta, H. & Koumoto, K. Thermoelectric properties of electron doped SrO(SrTiO₃)_n ($n = 1, 2$) ceramics. *J. Appl. Phys.* **105**, 103701 (2009).
22. Cahill, D. G., Melville, A., Schlom, D. G., & Zurbuchen, M. A. Low thermal conductivity of CsBiNb₂O₇. *Appl. Phys. Lett.* **96**, 121903 (2010).
23. Udayakumar, K. R. & Cormack, A. N. Structural Aspects of Phase Equilibria in the Strontium-Titanium-Oxygen System. *J. Amer. Ceram. Soc.* **71**, C469 (1988).
24. *The Chemistry of Extended Defects in Non-metallic Solids: Proceedings of the Institute for Advanced Study on the Chemistry of Extended Defects in Non-metallic Solids*, edited by L. Eyring and M. O’Keefe (North-Holland, Amsterdam, 1970), pp. 1-20.
25. Haeni, J. H. *et al.* Epitaxial growth of the first five members of the Sr_{n+1}Ti_nO_{3n+1} Ruddlesden-Popper homologous series. *Appl. Phys. Lett.* **78**, 3292 (2001).

26. Tian, W., Pan, X. Q., Haeni, J. H., & Schlom, D. G. Transmission-electron microscopy of the $n = 1-5$ $\text{Sr}_{n+1}\text{Ti}_n\text{O}_{3n+1}$ epitaxial thin films. *J. Mater. Res.* **16**, 2013 (2001).
27. Orloff, N. D. *et al.* Broadband dielectric spectroscopy of Ruddlesden-Popper $\text{Sr}_{n+1}\text{Ti}_n\text{O}_{3n+1}$ ($n=1, 2, 3$) thin films. *Appl. Phys. Lett.* **94**, 042908 (2009).
28. Tian, W. *et al.* Epitaxial growth and magnetic properties of the first five members of the layered $\text{Sr}_{n+1}\text{Ru}_n\text{O}_{3n+1}$ oxide series. *Appl. Phys. Lett.* **90**, 022507 (2007).
29. Theis, C. D. & Schlom, D. G. Cheap and stable titanium source for use in oxide molecular beam epitaxy systems. *J. Vac. Sci. Technol. A* **14**, 2677 (1996).
30. Haeni, J. H., Theis, C. D., & Schlom, D. G. RHEED Intensity Oscillations for the Stoichiometric Growth of SrTiO_3 Thin Films by Reactive Molecular Beam Epitaxy. *J. Electroceram.* **4**, 385-391 (2000).
31. Chakoumakos, B. C., Schlom, D. G., Urbanik, M., & Luine, J. Thermal expansion of LaAlO_3 and $(\text{La,Sr})(\text{Al,Ta})\text{O}_3$, substrate materials for superconducting thin-film device applications. *J. Appl. Phys.* **83**, 1979 (1998).
32. Nelson, J. B. & Riley, D. P. An experimental investigation of extrapolation methods in the derivation of accurate unit-cell dimensions of crystals. *Proc. Phys. Soc. London* **57**, 160 (1945).
33. Zurbuchen, M. A. *et al.* Morphology, structure, and nucleation of out-of-phase boundaries (OPBs) in epitaxial films of layered oxides. *J. Mater. Res.* **22**, 1439 (2007).
34. Cahill, D. G. *et al.* Nanoscale Thermal Transport. *J. Appl. Phys.* **93**, 793 (2003).
35. Cahill, D. G. Analysis of heat flow in layered structures for time-domain thermoreflectance. *Rev. Sci. Instrum.* **76**, 5119 (2004).
36. Wang, Y. *et al.* Interfacial thermal resistance and thermal conductivity in nanograined SrTiO_3 . *Appl. Phys. Express* **3**, 031103 (2010).
37. Brooks, C. M. *et al.* Tuning thermal conductivity in homoepitaxial SrTiO_3 films via defects. *Appl. Phys. Lett.* **107**, 051902 (2015).
38. Ravichandran, J. *et al.* Crossover from incoherent to coherent phonon scattering in epitaxial oxide superlattices. *Nat. Mater.* **13**, 168 (2014).

Chapter 6 Outlook and Conclusion

Out-of-plane ferroelectric barium-containing $(\text{SrTiO}_3)_n\text{SrO}$ Ruddlesden-Popper superlattices

In the application of $(\text{SrTiO}_3)_{n-1}(\text{BaTiO}_3)_1\text{SrO}$ Ruddlesden-Popper phases to tunable dielectrics, an open question is the incorporation of higher concentrations of barium into the $(\text{SrTiO}_3)_n\text{SrO}$ superlattice. BaTiO_3 is metastable in the Ruddlesden-Popper structure, with the non-perovskite barium orthotitanate (Ba_2TiO_4) being the lowest energy phase¹²⁻⁶. Seen in this thesis work, these structures can be stabilized by molecular-beam epitaxy without the formation of secondary phases.

Density-functional theory calculations were done to predict the properties of these higher barium compounds. Seen in Figure 6.1 are calculations using the VASP software package^{7,8} with the PBEsol exchange-correlation functional.⁹ Gamma-point phonons were calculated for the strained structures in the aristotype space group $I4/mmm$, using the finite displacement method as implemented in Phonopy¹⁰. A schematic of the structure is shown in Figure 6.1a where the BaTiO_3 layers are increased inside the $(\text{SrTiO}_3)_n\text{SrO}$ superlattice. In Figure 6.1a & b calculations on the phonon component associated with in-plane (IP) and out-of-plane (OOP) polarization are calculated with epitaxial strain, (001)-oriented SrTiO_3 having the highest compressive strain.

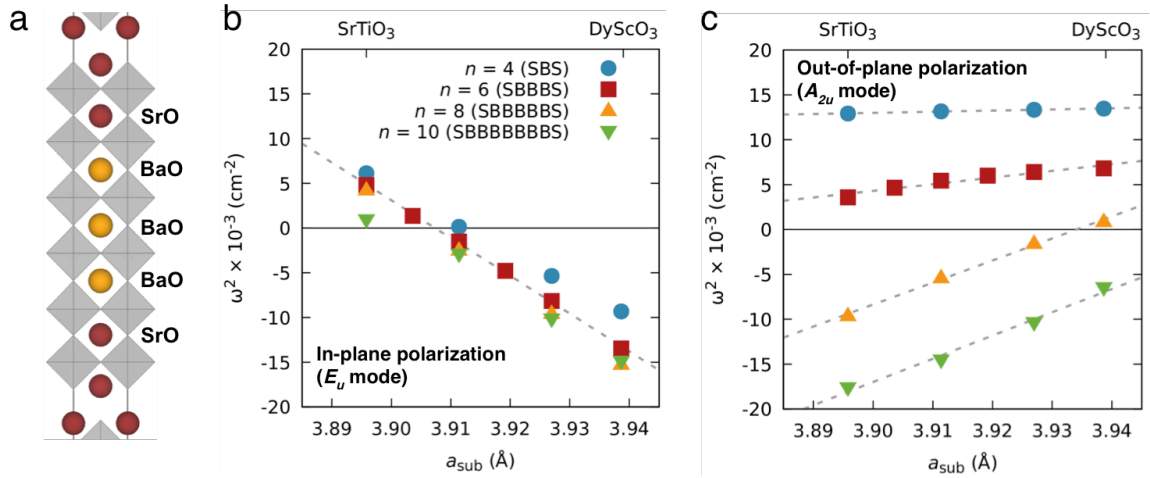


Figure 6.1 a, Schematic of the $(\text{BaTiO}_3)_n\text{SrO}$ unit cell. b, First-principles calculation of the phonon component associated with in-plane polarization for $(\text{BaTiO}_3)_n\text{SrO}$ at various compressive epitaxial strain states from (001) SrTiO_3 to (110) DyScO_3 . The material is considered to likely be ferroelectric if the square of this phonon, ω^2 , becomes negative. c, Calculations of the phonon component associated with out-of-plane polarization.

Surprisingly in this structure both in-plane and out-of-plane polarization can be induced. This was thought unlikely due to the $(\text{SrO})_2$ layers breaking up the chain of O-Ti-O bonds along the c -axis, which mediate ferroelectricity. A critical amount of > 5 unit cells of BaTiO_3 was calculated to be needed to induce OOP polarization on (110)-oriented DyScO_3 .

Barium containing $(\text{SrTiO}_3)_n\text{SrO}$ Ruddlesden-Popper films could open new types of properties and devices if the direction of polarization/tunability could be reliably manipulated with the barium concentration. Films with an out-of-plane ferroelectric component could be used for vertical device geometries where the electric field can be fully concentrated in the active material, maximizing device tunability. Up till now only planar geometries can be used in $m = 0$ or 1 $(\text{SrTiO}_3)_n$.

$m(\text{BaTiO}_3)_m\text{SrO}$ films which have in-plane ferroelectricity. In the planar geometry most of the field is concentrated in the substrate and not the active film, lowering overall device tunability. With a vertical device, higher device tunability can be reached due to the applied electric field only sampling the tunable dielectric as well as a smaller device footprint, advantageous to industry applications. It will also allow the superlattice to be integrated with a wider array of materials for more complex devices.

When I first attempted to grow these higher barium-containing Ruddlesden-Popper superlattices in the form of $(\text{BaTiO}_3)_{n-1}(\text{SrTiO}_3)_1\text{SrO}$ films on (110) DyScO_3 , secondary-phase formation was seen in all growths in the spotty reflection high-energy electron diffraction image (RHEED) shown in Figure 6.2b and the low quality x-ray diffraction in Figure 6.2c.

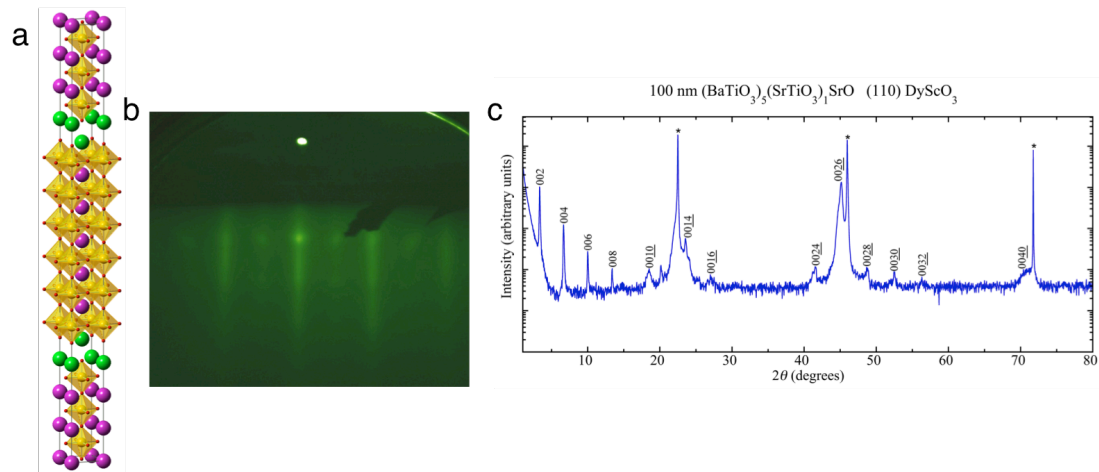


Figure 6.2 **a**, A schematic of the $(\text{BaTiO}_3)_5(\text{SrTiO}_3)_1\text{SrO}$ unit cell with barium atoms shown in pink and strontium atoms in green. **b**, A RHEED image in the [110] azimuthal direction of the growing $(\text{BaTiO}_3)_5(\text{SrTiO}_3)_1\text{SrO}$ film on (110) DyScO_3 . Spots are seen in the diffraction pattern indicating a rough surface and likely secondary phase formation. **c**, The x-ray diffraction spectra from a 100 nm thick $(\text{BaTiO}_3)_5(\text{SrTiO}_3)_1\text{SrO}$ film on (110) DyScO_3 . Poor superlattice ordering is seen in the lack of sharp and missing peaks at higher 2θ angles.

I hypothesized that the secondary phase formation was due to barium-containing phases, like barium orthotitanate, forming at the floating SrO layer known to occur in $(\text{SrTiO}_3)_n\text{SrO}^{11,12}$. When the floating layer reaches a threshold of BaO concentration, a secondary phase begins to form. I observed that once a double SrO layer was deposited, the RHEED image returned to the streaky pattern of high-quality terrace growth.

To avoid this secondary-phase formation I believe is associated with the BaO at the floating layer, I grew various concentrations of $(\text{Ba}_x\text{Sr}_{1-x}\text{TiO}_3)_{n-1}(\text{SrTiO}_3)_1\text{SrO}$ on (110) DyScO₃ to find the highest x compound that can be grown without the additional RHEED spots seen during growth. I found that concentration to be $x = 0.6$. At this lower concentration of BaTiO₃ a higher n is needed in the $(\text{Ba}_x\text{Sr}_{1-x}\text{TiO}_3)_{n-1}(\text{SrTiO}_3)_1\text{SrO}$ superlattice to reach the critical > 5 BaTiO₃ unit cells predicted by theory to induce an out-of-plane ferroelectric component. A series of 150 nm thick films with $n = 10, 15,$ and 20 (total BaTiO₃ unit cells equals 6, 9, and 12 per formula unit respectively) were grown with $x = 0.6$ $(\text{Ba}_x\text{Sr}_{1-x}\text{TiO}_3)_{n-1}(\text{SrTiO}_3)_1\text{SrO}$ with 15 nm thick SrRuO₃ bottom electrodes on (110) DyScO₃ to test out-of-plane ferroelectric properties. These films were grown at $T = 850$ °C at 7×10^{-7} Torr O₂ + ~10% O₃ in the Veeco GEN10 molecular-beam epitaxy chamber. The resulting XRD and ω rocking curves are shown in Figure 6.3. All films show the desired periodicity with no second phases. The ω rocking curves show some film relaxation is occurring due either to the quality of the underlying SrRuO₃ film or small volume of secondary phases distorting the crystal that are not observed in XRD.

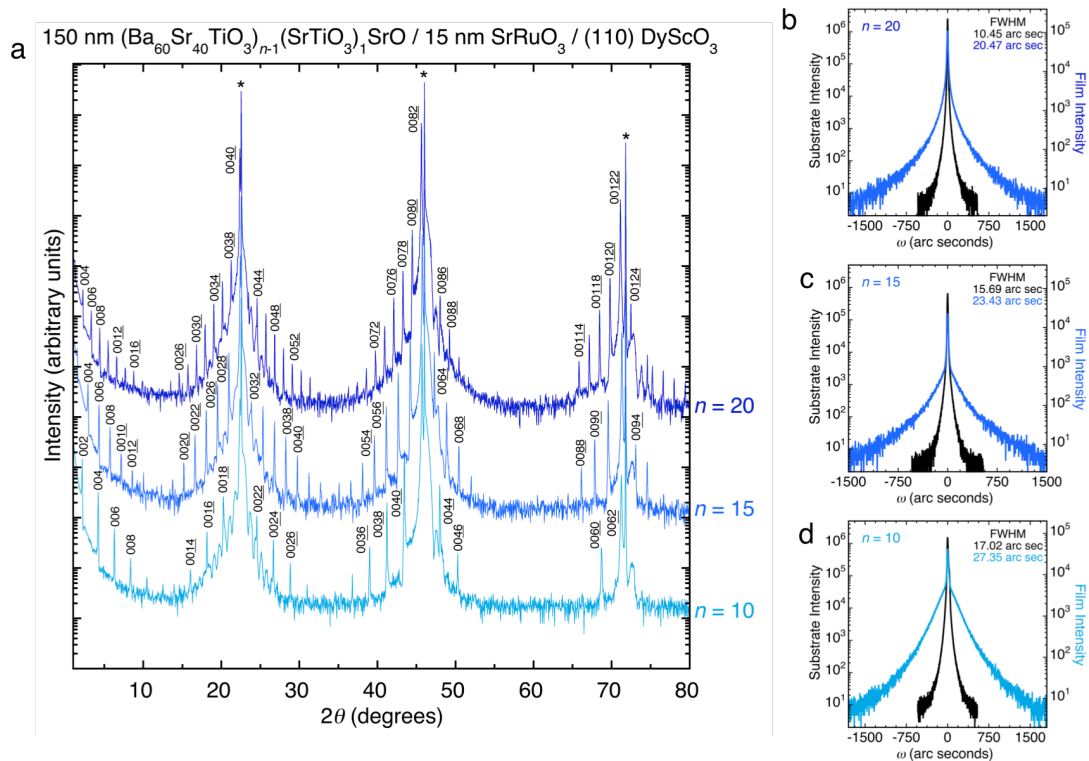


Figure 6.3 **a**, X-ray Diffraction of 150 nm thick $(\text{Ba}_{60}\text{Sr}_{40}\text{TiO}_3)_{n-1}(\text{SrTiO}_3)_1\text{SrO}$ films grown on 15 nm thick SrRuO_3 bottom electrodes on (110) DyScO_3 . **b**, ω rocking curves about the 220 DyScO_3 substrate peak and the $n = 20$ 0082 film peak, **c**, the $n = 15$ 0062 film peak, and **d**, the $n = 10$ 0042 film peak.

Circular electrodes of 100 nm gold with a 10 nm chrome adhesion layer were photolithographically patterned on to the samples with a diameter of 20 μm . The OOP dielectric constant, K_{33} , was measured seen in Figure 6.4 using a LCR meter and a cryoprobe down to liquid nitrogen temperatures to identify the samples' ferroelectric transition temperature. Ferroelectric hysteresis loops were also attempted with a TF Analyzer 2000 with no success due to large leakage in the samples.

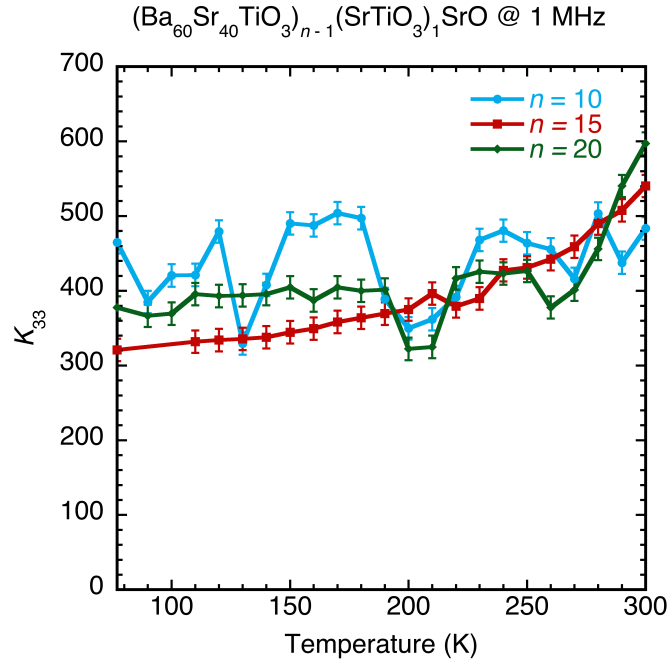


Figure 6.4 The out-of-plane dielectric temperature, K_{33} , with temperature of the $n = 20, 15,$ and 10 (Ba₆₀Sr₄₀TiO₃)_{n-1}(SrTiO₃)₁SrO films. Samples $n = 15$ and 20 have a phase transition above 300 K but it is unclear if this is associated with ferroelectricity.

Sample $n = 10$ does not show a transition at any measured temperature but samples with $n = 15$ and 20 do show a transition above 300 K. It is unclear if this is a ferroelectric transition or some other structural change. Piezoforce microscopy measurements will be carried out to confirm if these samples are polar and can be switched in the out-of-plane direction.

By refining the growth methodology to mitigate secondary-phase formation and more precise ferroelectric characterization, I am optimistic that the first out-of-plane ferroelectric Ruddlesden-Popper superlattice can be achieved.

Conclusions

With technologies increasingly relying on the radio wave spectrum to transmit information, the mmWave gigahertz frequencies are especially attractive for gigabyte per second data transfer rates for applications like 5G cellphones. At these frequencies charged point defects, entropically inevitable in ceramic components, have a resonance, dissipating the electric field as heat phonons. Epitaxially strained $(\text{SrTiO}_3)_n\text{SrO}$ Ruddlesden-Popper superlattices were found to have extremely low loss and tunability up to 125 GHz, having the highest figure of merit reported in literature. I have shown through positron annihilation lifetime spectroscopy of a series of non-stoichiometric 300 nm thick $(\text{Sr}_{1+\delta}\text{TiO}_3)_6\text{SrO}$ films on (001) SrTiO_3 that the $(\text{SrO})_2$ faults are indeed accommodating the non-stoichiometric point defects. Little variance is seen in the series of the type of vacancy observed, and the dominant vacancy, $V_{\text{Ti-O}_x}$ is likely associated with the $(\text{SrO})_2$ layers themselves. Another way of considering the $(\text{SrO})_2$ layers is that they provide an outlet for the entropy of the system, with the low-loss non-tunable $(\text{SrO})_2$ faults meandering about the tunable SrTiO_3 which can now be free of charged point defects allowing for high frequency applications.

I examined the thermal transport in the $(\text{SrTiO}_3)_n\text{SrO}$ system for a series of 300 nm thick $(\text{SrTiO}_3)_n\text{SrO}$ films on (001) SrTiO_3 . The Ruddlesden-Popper system is ideal for the study of thermal transport as the superlattices naturally have atomically precise interfaces, which has confounded previous studies. I found that the $(\text{SrO})_2$ layers effectively scatter phonons, lowering the longitudinal thermal conductivity, and a scattering saturation is reached beyond the $n = 3$ phase associated with the mean free path of phonons in SrTiO_3 .

The work on $(\text{SrTiO}_3)_n\text{SrO}$ for high frequency tunable dielectrics suffered from 50 nm film thickness before relaxation occurred due to the $\sim 1.1\%$ epitaxial strain imposed by the (110) DyScO_3 substrate. Epitaxial strain is required for $(\text{SrTiO}_3)_n\text{SrO}$ to induce ferroelectricity and tunability in the paraelectric phase. This low film thickness reduces overall device tunability. To improve tunability and provide flexibility in substrate choice I integrated ferroelectric BaTiO_3 into the $(\text{SrTiO}_3)_n\text{SrO}$ forming the first reported $(\text{SrTiO}_3)_{n-1}(\text{BaTiO}_3)_1\text{SrO}$ series in the literature. A single unit cell of BaTiO_3 was layered in the middle of the SrTiO_3 component and was found through DFT to produce the largest increase in ferroelectric polarization and thus tunability in the paraelectric phase while lowering the overall epitaxial strain. The single BaTiO_3 layer creates the largest distortion in the surrounding SrTiO_3 through a targeted chemical pressure effect of the structure. The 100 nm thick $n = 6$ $(\text{SrTiO}_3)_{n-1}(\text{BaTiO}_3)_1\text{SrO}$ film on (110) DyScO_3 now has the highest figure of merit in the literature from the increase of tunability in the low loss structure at frequencies up to 140 GHz. Higher barium concentrations are being examined for out-of-plane ferroelectricity allowing for more efficient vertical device geometries.

Finally I showed that these barium-containing superlattices in the form of $(\text{Ba}_x\text{Sr}_{1-x}\text{TiO}_3)_{n-1}(\text{SrTiO}_3)_1\text{SrO}$ can be integrated with silicon and can significantly lower current leakage in MIM device structures as compared to their $\text{Ba}_x\text{Sr}_{1-x}\text{TiO}_3$ counterparts.

References

1. Bland, J. A. The crystal structure of barium orthotitanate, Ba_2TiO_4 . *Acta Crystallogr.* **14**, 875–881 (1961).
2. Kwestroo, W. & Paping, H. A. M. The Systems BaO-SrO-TiO_2 , BaO-CaO-TiO_2 , and SrO-CaO-TiO_2 . *J. Am. Ceram. Soc.* **42**, 292–299 (1959).
3. Suzuki, T., Nishi, Y. & Fujimoto, M. Ruddlesden–Popper Planar Faults and Nanotwins in Heteroepitaxial Nonstoichiometric Barium Titanate Thin Films. *J. Am. Ceram. Soc.* **83**, 3185–3195 (2000).
4. Fujimoto, M. & Suzuki, T. High-Resolution Transmission Electron Microscopy and Computer Simulation of Defect Structures in Electronic Perovskite Ceramics. *J. Ceram. Soc. Jpn.* **109**, 722–732 (2001).
5. Lee, S., Randall, C. A. & Liu, Z.-K. Modified Phase Diagram for the Barium Oxide–Titanium Dioxide System for the Ferroelectric Barium Titanate. *J. Am. Ceram. Soc.* **90**, 2589–2594 (2007).
6. Twigg, M. E., Alldredge, L. M. B., Chang, A., Podpirka, A., Kirchoefer, S. W., & Pond, J. M. Structure and composition of $\text{Ba}_{0.5}\text{Sr}_{0.5}\text{TiO}_3$ films deposited on (001) MgO substrates and the influence of sputtering pressure. *Thin Solid Films* **548**, 178–185 (2013).
7. Kresse, G. & Furthmüller, J. Efficient iterative schemes for ab initio total-energy calculations using a plane-wave basis set. *Phys. Rev. B* **54**, 11169–11186 (1996).
8. Kresse, G. & Joubert, D. From ultrasoft pseudopotentials to the projector augmented-wave method. *Phys. Rev. B* **59**, 1758–1775 (1999).
9. Perdew, J. P. *et al.* Restoring the Density-Gradient Expansion for Exchange in Solids and Surfaces. *Phys. Rev. Lett.* **100**, 136406–136406 (2008).
10. Togo, A. & Tanaka, I. First principles phonon calculations in materials science. *Scr. Mater.* **108**, 1–5 (2015).
11. Lee, J. H. *et al.* Dynamic Layer Rearrangement During Growth of Layered Oxide Films by Molecular Beam Epitaxy. *Nat. Mater.* **13**, 879–883 (2014).
12. Nie, Y. F. *et al.* Atomically precise interfaces from non-stoichiometric deposition. *Nat. Comm.* **5**, 4530 (2014).

Appendix A

Basic Photolithography Recipe

Good for patterns with feature ≥ 5 μm

Positive resist

Required CNF training:

General photolithography

Heidelberg Mask Writer - DWL2000

Glen 1000 Resist Strip

ABM Contact Aligner

SC4500 Odd-Hour Evaporator

Run process multiple time on dummy samples (bare substrates) finding optimal exposure (0.5 sec steps) and development time (30 sec steps) for your specific pattern.

1. Sonicate samples 1 min each - Acetone, IPA, DI water - blow/spin dry
2. Glen 1000 Resist Strip (process 3 - 100 W 100 W 45 sec, RIE mode, shelf b, put samples on Si wafer on 2 glass slides to prevent heating from shelves)
3. On spinner (Level 1 resist station) put 1 drop on AZ nLOF2020 at each corner of square sample - use smallest chuck
4. Spin at 4000 rpm , Ramp 100 rpm/s , 45 sec
 - a. Should give $\sim 2\text{-}3$ μm thick
 - b. If blotchy, streaky, or a particulate need to start over
5. Spray acetone on beta wipe (far away from sample), place newly spun sample on acetone part to remove resist on back
6. Bake 60 sec at 115 C
7. Expose 6 - 7.5 sec ABM contact Aligner
 - a. Use hard contact - clean with Acetone and IPA spray in between each use to clear away resist that will stick to mask - check no streaks
8. Bake 75 sec at 115 C
9. Develop AZ-MIF 726 for 1 min - 6 min
 - a. Gently shake with tweezers while developing to promote resist removal
 - b. If doing large batch can rotate through samples gently shaking 10 sec ea
10. In larger beaker spray each sample directly with water gun to clean out hard to remove spots
11. Blow dry
12. Check with optical microscope if pattern appears as should or if need to redo

13. Glen 100 Resist Strip (process 3 - 100 W 100 W 45 sec, RIE mode, shelf b, put samples on Si wafer on 2 glass slides to prevent heating from shelves)
 - a. Do right before depositing
14. Using Odd-hour evaporator deposit
 - a. 1st 100 A chrome (Cr) @ 0.5 A/s (use Cr rod thermal evap - adhesion layer)
 - b. 2nd 1000 A gold (Au) @ 1.5 A/s (ebeam)
15. Lift-off - put in Acetone for ~ 2 hrs, gently shake, put in fresh Acetone and sonicate for < 15 sec
 - a. Check resist fully removed
16. Sonicate IPA 5 sec, DI rinse, blow dry

Optimizing recipe tips:

Start with changing exposure time in 0.5 sec increments for a given developer time, will change results most

With best looking exposure time change developer time in 30 sec increments

Also check if mask dirty and causing rough edges

Mask Notes - check CNF wiki for deleving process

In making mask pattern - use L-Edit, can start from pattern already on file here

For positive resist (this recipe): When load/convert for DWL2000 XOR layers (frame layer 1st, pattern 2nd). Then when get to plate exposure options check XOR

In making mask if chrome etch not remove all the way after standard process and looks 'foggy' manually etch mask in 'chrome etch' for 15 sec

Removing Patterned Electrodes and not oxide film

Use Gold Etch TFA (iodide based)

40 A/s etch rate

Chrome Etch (does have some nitric acid that can etch oxide so do not mess up this part)

13 A/s